Advances in *ab initio* approaches

to nuclear structure, reaction and nucleonic dynamics

by

Weijie Du

A dissertation submitted to the graduate faculty

in partial fulfillment of the requirements for the degree of

DOCTOR OF PHILOSOPHY

Major: Nuclear Physics

Program of Study Committee:
James P. Vary, Major Professor
Pieter Maris
Kirill Tuchin
Glenn R. Luecke
Amanda Weinstein

The student author, whose presentation of the scholarship herein was approved by the program of study committee, is solely responsible for the content of this dissertation. The Graduate College will ensure this dissertation is globally accessible and will not permit alterations after a degree is conferred.

Iowa State University

Ames, Iowa

2019

DEDICATION

This thesis is dedicated to my beloved parents and grandparents.

TABLE OF CONTENTS

Page

LIST OF TABLES

LIST OF FIGURES

ACKNOWLEDGEMENTS

I am deeply indebted to my advisor, Prof. Dr. James P. Vary, for his fundamental role in my doctoral study. Dr. Vary is visionary, insightful, patient, supportive, experienced and inspiring. He provided me the freedom in research, while continuing to contribute valuable feedback, advice and encouragement. I could not imagine a better adviser.

I am grateful to Prof. Dr. Pieter Maris (committee member). I benefit a lot from his insightful critiques and high standard. I wish I could have learned more from such a first-class scientist.

I could not forget to thank Prof. Dr. Kirill Tuchin (committee member). As a beginning graduate student who knew barely college physics in 2013, I was really fortunate to have attended his courses, Quantum Mechanics I & II. It was from him that I learned the fundamental elements in studying theoretical physics.

I want to express my sincere appreciation to Prof. Dr. Glenn R. Luecke (committee member) and Prof. Dr. Amanda Weinstein (committee member). I am grateful to their insightful and hard questions, which inspired me to broaden my knowledge spectrum from various perspectives.

I am very thankful to Prof. Dr. Xingbo Zhao. He provided me consistent, valuable help in my research. I am also grateful to my colleagues Peng Yin (Ph.D.), Guangyao Chen (Ph.D.), Yang Li (Ph.D.) and Hugh D. Potter (Ph.D.). I benefit a lot from our discussions. I wish them great success in their careers.

I am grateful to Paula Herrera Siklódy (Ph.D.), Helen M. Fretwell (Ph.D.), Debra Schmidt, Lori Hockett, Linda K. Shuck and Gloria Oberender. I appreciate their great help in my work and study in the Physics department.

I want also to express my appreciation to my friends, including but not limited to: Boqun Song, Boyu Chen, Boping Chen, Liang Luo (Ph.D.), Xu Yang (Ph.D.), Tai Kong (Ph.D.), Tianqi Li (Ph.D.), Evan Stewart, William Meier (Ph.D.) and his families, Seth Loyd and his families.

I gratefully acknowledge the staff of the Parks library. They host a great place where I did a significant part of my course and research work.

Finally, I would like to thank my beloved parents and grandparents: I simply miss them every day.

ABSTRACT

We calculate effective Hamiltonians and effective electroweak operators with the Okubo-Lee-Suzuki formalism for two-nucleon systems. Working within a harmonic oscillator basis, first without and then with a confining harmonic oscillator trap, we demonstrate the effects of renormalization on observables calculated for truncated basis spaces. We illustrate the renormalization effects for the root-mean-square point-proton radius, electric quadrupole moment, magnetic dipole moment, Gamow-Teller transition and neutrinoless double-beta decay operator using nucleon-nucleon interactions from chiral effective field theory. Renormalization effects tend to be larger in the weaker traps and smaller basis spaces suggesting applications to heavier nuclei with transitions dominated by weakly-bound nucleons would be subject to more significant renormalization effects within achievable basis spaces.

We also develop an *ab initio*, non-perturbative, time-dependent basis function method to solve the nuclear structure and scattering problems in a unified manner. We apply this method to a test problem: the Coulomb excitation of a trapped deuteron by an impinging heavy ion. The states of the deuteron system are obtained by the *ab initio* nuclear structure calculation implementing a realistic inter-nucleon interaction with a weak external trap to localize the center of mass and to discretize the continuum. The evolution of the internal state of the deuteron system is directly solved using the equation of motion for the scattering. We analyze the excitation mechanism of the deuteron system by investigating its internal transition probabilities and observables as functions of the exposure time and the incident speed. In this investigation, the dynamics of the Coulomb excitation are revealed by the time evolution of the system's internal charge distribution.

Finally, we present the first application of the Basis Light-Front Quantization method to a simple chiral model of the nucleon-pion system as a relativistic bound state for the physical proton. The light-front mass-squared matrix of the nucleon-pion system is obtained within a truncated basis.

The mass and the corresponding light-front wave function (LFWF) of the proton are computed by numerical diagonalization of the resulting mass-squared matrix. With the boost invariant LFWF, we evaluate the proton's parton distribution function and Dirac form factor. An improved model, adopting phenomenological corrections for quark contributions, is implemented to calculate the proton's Dirac form factor. The resulting Dirac form factor agrees well with the experimental data below the squared transverse momentum transfer of 0.20 GeV^2.

CHAPTER 1. OVERVIEW

An important topic in nuclear physics is to develop a basic understanding of nuclear structure, reactions and nucleonic dynamics from the fundamental theory, Quantum Chromodynamics (QCD). Progress in this direction would, on the one hand, help answer fundamental questions such as [1]

- How do protons and neutrons make stable nuclei and rare isotopes? Where are the limits?
- What are the heaviest nuclei that can exist?
- What is the origin of simple patterns observed in complex nuclei?
- How do we describe fission, fusion, and other nuclear reactions?
- How did the elements from iron to uranium originate?
- What is the equation of state of nucleonic matter?

On the other hand, efforts in seeking such a bottom-up understanding in nuclear physics will illuminate, and in turn be fertilized by, other pursuits such as the quest for nature's fundamental symmetries and other disciplines such as the life sciences, material sciences, energy, security, etc [1].

Ab initio (i.e., from first principle) approaches provide pathways to address the challenges and opportunities listed above. In this thesis, we present our efforts in developing *ab initio*, non-perturbative methods to study nuclear structure, reaction, and nucleonic dynamics. As shown in Fig. 1.1, our works focus on achieving benchmark tests of *ab initio* methods (which are positioned between "development" and "next step" in Fig. 1.1) within two main perspectives: 1) non-relativistic structure and reaction theories/techniques that are based on the nuclear interaction; and 2) relativistic structure theory/method that is based on the chiral Lagrangian.

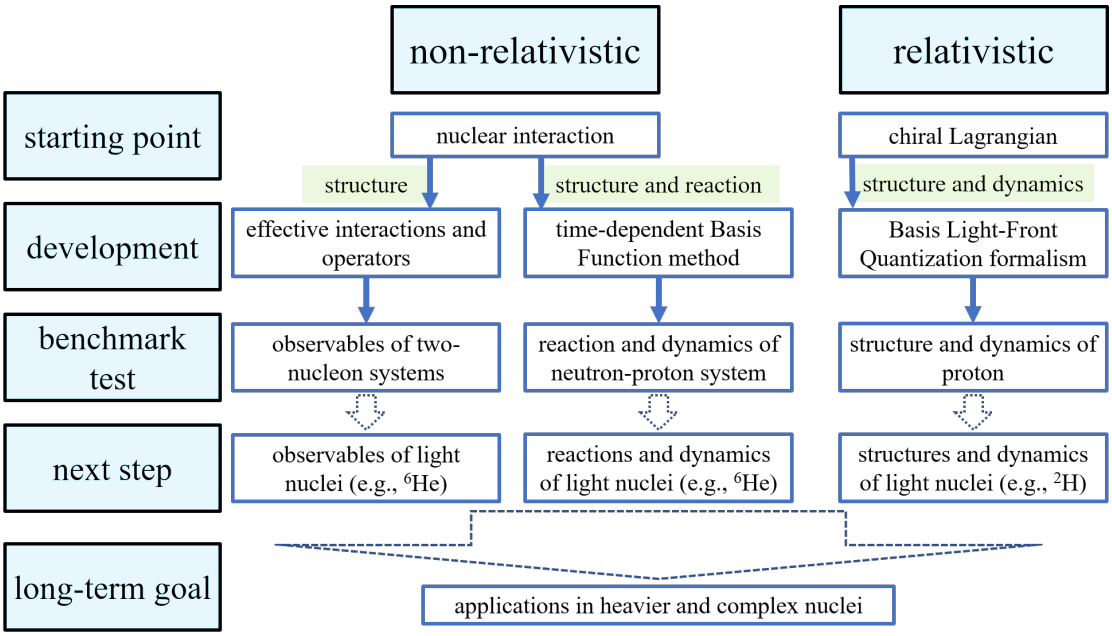

Figure 1.1: The scope of the thesis (see details in the text).

In applying the fully microscopic approaches to study heavier nuclei with the multi-nucleon interactions and coupling to the continuum included, the computing power is still too demanding even for the Exascale supercomputers (defined as having capabilities for 10^{18} floating-point operations per second (flops)). As one of our efforts in the non-relativistic perspective, we work on developing the renormalization scheme in the nuclear structure theories in order to reduce the computational burden for large-scale *ab initio* calculations (see the extensive introduction in Sec. 2.1). In particular, we develop the effective interaction and, consistently, the effective operators for additional observables and test the renormalization effects by studying numerically solvable two-nucleon systems. In the next step, this theory/technique will be adopted to study the observables of light nuclei such as ^{6}He as a major step towards applications in heavier nuclei.

We also develop an *ab initio* method that treats non-relativistic nuclear structure and reactions in a unified manner (see the extensive introduction in Sec. 3.1). We introduce the time-dependent Basis Function (tBF) method that retains the full, non-perturbative quantum coherence of the scattering over all potentially relevant intermediate states necessary for accurate descriptions of

dynamical multi-step scattering processes. We demonstrate the utility of the tBF method via a model problem, i.e., the Coulomb excitation of a trapped deuteron by an impinging heavy ion, where we analyze, in detail, the dynamics of the deuteron system during scattering. In the next step, we plan to further develop this method to treat general reaction problems for light and, eventually, heavier nuclei.

Within the relativistic perspective, we introduce a framework to study the nuclear structure and dynamics via an *ab initio*, non-perturbative approach (see the extensive introduction in Sec. 4.1). In particular, we develop a method to treat a chiral model (Lagrangian) of the nucleon-pion system via the Basis Light-Front Quantization (BLFQ) approach. As a test problem, we apply this method to investigate the properties (structure and dynamics) of the physical proton, which is treated as the relativistic bound state of the nucleon-pion system described by the chiral Lagrangian. In the future, we will further develop this method to study the structure and dynamics of more complex nuclei.

The arrangement of this thesis is the following. In Chapter 2.1, we present the development and tests of the effective interactions and operators based on our recently published works [2, 3]. In Chapter 3, we show our work in developing and testing the framework of the time-dependent basis function method based on our works [4, 5]. In Chapter 4, we show the development and applications of the Basis Light-Front Quantization approach for the dynamical nucleon-pion system based on our works [6, 7]. We offer conclusions and outlooks in Chapter 5. The necessary mathematical details are in the Appendices for completeness.

CHAPTER 2. EFFECTIVE INTERACTIONS AND OPERATORS

2.1 Introduction

The *ab initio* nuclear theory establishes the link between the properties of atomic nuclei and the inter-nucleon interactions [8, 9]. Investigations along this line offer promising vistas into a wide range of complex nuclear phenomena as well as into the fundamental symmetries of nature [9].

Groundbreaking progress of the *ab initio* nuclear theory has been made after Yukawa first proposed the microscopic theory of the nuclear interaction based on the idea of boson exchange. Theoretically, various theories of the nuclear potentials/interactions have been proposed, such as the standard, accurate meson-exchange nuclear potentials (e.g., the Argonne V18 [10], INOY [11] and CD-Bonn 2000 [12]) and the realistic/phenomenological nuclear potentials (e.g., JISP16 [13] and Daejeon16 [14]). These potentials enable the construction of the nuclear many-body Hamiltonians. Several many-body techniques have also been developed, including: 1) the exact methods, such as Greens Function Monte Carlo approach [15, 16, 17, 18], no-core shell model (NCSM) approach [19, 20, 9], the coupled cluster approach [21], the lattice-simulation approach with nucleons, using effective field theory (EFT) [22]; and 2) the approximate methods, such as the interacting shell model [23, 24]. These techniques enable solving the resulting nuclear many-body Hamiltonians (equivalently, the many-body Schrödinger equation). In addition, there are also advances that facilitate (or promise to facilitate) the computation/storage/extrapolation of large tensors that encode the quantum many-body problem, such as the supercomputing techniques (see, e.g., [9, 3] and references therein), the deep learning techniques (see, e.g., [25]) and, most recently, the quantum computing techniques [26].

There are several key problems, among others, in the *ab initio* nuclear theory.

1. The link between the nuclear interactions and the fundamental theory (QCD) is not firmly established. Building this link will provide insight into the role QCD plays in nuclear structure and reactions.

2. The *ab initio* calculations based on many of these potentials do not utilize consistent operators for all observables and, hence, do not establish the predictive power. While many known experimental data can be well reproduced, extrapolations to unknown region of the Segrè chart will likely be unreliable.

3. The "hard core" problem plagues many nuclear potentials. Physically, this problem results from strong repulsion at small separations between physical nucleons. Mathematically, this problem results in strong correlations between high- and low-momentum components in the nuclear wave function, which requires a high-resolution description of the nuclear system up to very high-momentum scale.[1] In practical terms, sophisticated many-body methods such as the Hamiltonian eigenvalue methods in very large basis spaces are required.

4. The required computing power typically scales exponentially or factorially with the number of nucleons for high-precision results with current exact many-body methods. Even for the approximate many-body methods, such scaling is polynomial. As a result, the *ab initio* calculations are still limited to light- and/or medium-mass nuclei [27].

In order to treat these problems, two conceptual revolutions were introduced. First, the EFT is proposed to model the nuclear interactions. This work was pioneered by Weinberg and collaborators [28, 29, 30, 31] and the theory is known today as the chiral EFT. The chiral EFT provides a direct link between the nuclear interaction and the underlying theory, QCD. Due to the systematic expansion and power counting scheme in the chiral EFT, the error of the truncation in the chiral expansion can be quantified. In particular, the neglected higher-order terms in the chiral Lagrangian are expected to contribute at a level that can be estimated, which facilitates the error estimation and guarantees the predictive power of the resulting *ab initio* calculations. In addition, the chiral

[1] Since many nuclear structure observables are of low-momentum scale, the high-momentum physics in the nuclear interactions with the high-resolution description can be avoided.

EFT offers flexibility in modeling the short-range part of the nuclear interaction due to its implicit and systematic treatment of the high-momentum degrees of freedom: the high-momentum physics is captured at each scale by the renormalization procedures.[2]

The second revolution is the further processing of nuclear interactions to derive effective inter-nucleon interactions with lower resolution and momentum scale that enable faster convergence of the *ab initio* calculation with respect to increasing basis size. Such methods include the renormalization group methods [32] and the similarity transformation methods [33, 34, 35, 36], among others. The underlying ideas of these methods are similar: since any unitary transformation of the nuclear Hamiltonian leaves its spectrum unchanged, it is thus desirable to design a unitary transformation to drive the Hamiltonian towards a certain form (e.g., diagonal or block-diagonalized form), wherein the coupling between the high- and low-momentum physics can be weakened/removed. As a result, the convergence in *ab initio* many-body calculation is further improved so that a desired accuracy is achieved within a practical basis dimension[3].

In this chapter, we present our work in deriving effective interactions (or, equivalently, effective Hamiltonians) from the chiral interactions [37, 38, 39, 40, 41, 42, 43] by the Okubo-Lee-Suzuki (OLS) similarity transformation method [33, 34, 35, 36]. The application of such effective interactions would reduce the computational burden while preserving the fidelity of the underlying theory of the nuclear interaction. Our focus is also on deriving the consistent effective electroweak operators. Thus, we aim to advance precision studies of electroweak properties (e.g., neutrinoless double-beta ($0\nu2\beta$) decay) of nuclei. We note that electroweak properties have become of great interest as a complement to major advances underway in experimental nuclear physics. By consistent, we mean that the effective electroweak operators are evaluated in the same formalism as the chiral interactions employed in the Hamiltonians.

[2]The chiral nuclear potential is obtained from the chiral Lagrangian by solving a non-perturbative Lippmann-Schwinger equation, in which process a regulating function with a (momentum) cutoff is usually introduced in order to regulate the loop divergences. This cutoff determines the corresponding scale of the nuclear potential and hence the limit of its applicability.

[3]Note there is, however, a price to pay for such transformation. Since the unitary transformation is to be performed in the many-body Hilbert space, many-body operators (e.g., for the nuclear interaction and observables) are induced. These induced terms are only retained up to some convenient level, leading to an approximation that requires further testing.

We provide demonstration cases using two-nucleon systems for the present purposes. Such systems are numerically solvable in a large three dimensional harmonic oscillator (3DHO) basis space, while providing high precision results for comparison with approximate results. This enables us to map out 1) the effects arising from the correlations governed by different interactions; 2) the effects due to basis-space truncation and the effects linked with the length scale of the environment (c.f., the mean field in the nuclei), the trap.

We study the renormalization effects (conversely, the truncation effects) on each electroweak operator for each chiral interaction, each basis space and each confining HO trap. This is achieved by comparing matrix elements of these effective interactions and operators with those from a truncated treatment of the original interactions and operators. Our work offers guidance to more realistic *ab initio* calculations of the nuclear properties in larger nuclei as in the case of the NCSM [44, 45, 46, 9, 19, 20], and to the *ab initio* valence space effective interactions as well [47].

This chapter is mainly based on the published papers [2, 3]. Except for part of the above introduction material and Sec. 2.2.3, this chapter is essentially the published paper [2]. It is organized in the following way. We begin with the theory in Sec. 2.2, where we discuss the Hamiltonian formalism of the many-body system, the truncation technique and the construction of the effective Hamiltonian and operators. We present the results and the corresponding discussion in Sec. 2.3.

2.2 Theory

2.2.1 Many-body systems

We seek to solve a Hermitian Hamiltonian H eigenvalue problem expressed in a suitable basis and, once the eigenvectors are obtained, to evaluate matrix elements of additional observables O. For nuclear physics applications, such as the NCSM, the resulting matrix for H is infinite dimensional. With truncation, the matrix of H becomes numerically tractable, allowing the study of results as a function of the finite basis parameters in order to estimate the converged results and their uncertainties. For the NCSM, we express H in terms of the relative kinetic energy operator

$T_{\rm rel}$ acting between all pairs of nucleons in the A-nucleon system and an interaction term V that may include multinucleon interactions as

$$H = T_{\rm rel} + V \ . \tag{2.1}$$

By adopting a complete basis of Slater determinants, $|\Phi_j\rangle$ for A nucleons, developed from a chosen single-particle basis, we express the complete space problem as a matrix eigenvalue problem. That is, the eigenvalues E_k and eigenstates $|\Psi_k\rangle$, expanded in our complete basis of Slater determinants, obey the equations

$$H|\Psi_k\rangle = E_k|\Psi_k\rangle \ , \tag{2.2}$$

$$|\Psi_k\rangle = \sum_j A_{kj}|\Phi_j\rangle \ , \tag{2.3}$$

where A_{kj} denotes the expansion coefficient.

The selection of the complete single-particle basis is flexible but we will follow a popular choice and adopt the 3DHO due to its well-studied analytical properties that facilitate numerical applications and the retention of the underlying symmetries of H [9]. We present some useful/relevant properties of the 3DHO basis, along with the formalism of the one-body operators, in Appendix A. We take the neutron and proton mass $\widetilde{M}_N$ to be the same (938.92 MeV, their average measured mass), so that the only length scale in the HO single-particle basis can be expressed in terms of the HO energy (or basis parameter) $\hbar\Omega$ as

$$\tilde{b} = \sqrt{\frac{\hbar}{\widetilde{M}_N \Omega}} \ . \tag{2.4}$$

2.2.2 Finite matrix truncation approach

In practical applications, it is advantageous to define the many-body truncation with $N_{\rm max}$, the maximum of the total HO quanta in the retained Slater determinants above the minimum total HO quanta for the A nucleons [45]. A quantum of the HO single-particle state is twice the radial quantum number n plus the orbital quantum number l. That minimum total HO quanta for the A nucleons also depends on the number of neutrons N and protons Z that comprise the system. Zero is the minimum total HO quanta for the two-nucleon systems addressed in this work.

We define the P-space (or "model space") as the basis space retained by this $N_{\max}$ truncation. The infinite dimensional space beyond this $N_{\max}$ truncation is called the Q-space. For a sufficiently large $N_{\max}$, some observables are seen to converge in very light nuclei for interactions which do not couple strongly to high-momentum states and when computational resources are sufficient. For example, using a chiral N^{2}LO NN interaction [37, 38], the ground-state energy of ^{6}Li has been calculated [39, 40, 41] in a sequence of HO basis spaces. With extrapolation to the complete basis, the result is $-31.0(2)$ MeV [41]. Here, the parenthesis specifies the uncertainty as 200 keV in the extrapolation. The basis space truncation for the largest finite basis employed in the extrapolation is $N_{\max} = 18$. At $N_{\max} = 18$ and $\hbar\Omega = 28$ MeV the ground-state energy, which is also a variational upper bound of the exact result, is already -29.928 MeV, i.e., about 1.1 MeV above the extrapolated result. For comparison, the experimental ground-state energy is -31.995 MeV [48].

However, other observables, such as the root-mean-square (r.m.s.) point-proton radius and electric quadrupole transitions, converge poorly up through $N_{\max} = 18$ [49]. For long-range observables such as the r.m.s. point-proton radius, the theoretical results are insufficiently converged to provide directly a meaningful comparison with experiment. For example, with extrapolations, the r.m.s. point-proton radius for ^{6}Li has significant uncertainties [49].

For all these reasons, it may be advantageous to soften the interactions and to promote improved convergence of the eigenvalue problem. As we explain in the next section, this softening, or renormalization of the interaction also necessitates renormalizing the operators corresponding to these other observables. That is, we need to consistently derive the effective operators for all observables in the chosen model space.

2.2.3 Effective Hamiltonian and operators

Once the complete basis space and the P-space are defined, we can address the development of an effective Hamiltonian H_{eff} for the P-space that formally retains a subset of the eigenvalues of the complete space. We adopt the OLS formalism in this work, which we briefly outline here.[4]

[4] In order to gain additional insights we present an alternative approach to the OLS formalism in Appendix B. More details can be found in Ref. [9] and the references therein.

The formal structure of the OLS approach is visualized by first considering H in the complete basis space and defining the unitary transformation U that diagonalizes H to produce the Hamiltonians spectrum. In the matrix representation, the diagonalization is

$$H_{\rm diag} \;=\; UHU^{\dagger} \;=\; \begin{pmatrix} E_1 & 0 & \cdots & 0 \\ 0 & E_2 & \cdots & 0 \\ \cdots & \cdots & \cdots & \cdots \\ 0 & 0 & \cdots & E_{\rm max} \end{pmatrix} , \tag{2.5}$$

where the subscript "max" denotes the dimension of the full model space. The unitary matrix U can be constructed by the eigenfunctions of H as

$$U \;=\; \begin{pmatrix} a_{1,1} & a_{1,2} & \cdots & a_{1,\rm max} \\ a_{2,1} & a_{2,2} & \cdots & a_{2,\rm max} \\ \cdots & \cdots & \cdots & \cdots \\ a_{\rm max,1} & a_{\rm max,2} & \cdots & a_{\rm max,max} \end{pmatrix} , \tag{2.6}$$

where, for example, $a_{1,2}$ means the amplitude of the $2^{\rm nd}$ component of the $1^{\rm st}$ energy eigenfunction.

The full model space can be divided into the P-space of the dimension d_P and the complementary Q-space of the dimension d_Q. We define our P-space to accommodate the lowest set of eigenvalues of the original Hamiltonian though other choices are feasible, such as retaining states whose eigenvectors have the largest probabilities of P-space configurations. The projection operator for each subspace can be constructed from the eigenvectors of the H such that

$$H^{P}_{\rm diag} \;=\; PH_{\rm diag}P \;=\; \begin{pmatrix} E_1 & 0 & \cdots & 0 \\ 0 & E_2 & \cdots & 0 \\ \cdots & \cdots & \cdots & \cdots \\ 0 & 0 & 0 & E_{d_P} \end{pmatrix} \tag{2.7}$$

and

$$H^Q_{\rm diag} \;=\; QH_{\rm diag}Q \;=\; \begin{pmatrix} E_{d_P+1} & 0 & \cdots & 0 \\ 0 & E_{d_P+2} & \cdots & 0 \\ \cdots & \cdots & \cdots & \cdots \\ 0 & 0 & 0 & E_{\rm max} \end{pmatrix} . \tag{2.8}$$

Making use of the projection operators, U can be partitioned as

$$U \;=\; \begin{pmatrix} PUP & PUQ \\ QUP & QUQ \end{pmatrix} , \tag{2.9}$$

where, for clarity, U^P is defined as [5]

$$U^P \;\equiv\; PUP \;=\; \begin{pmatrix} a_{1,1} & a_{1,2} & \cdots & a_{1,d_P} \\ a_{2,1} & a_{2,2} & \cdots & a_{2,d_P} \\ \cdots & \cdots & \cdots & \cdots \\ a_{d_P,1} & a_{d_P,2} & \cdots & a_{d_P,d_P} \end{pmatrix} . \tag{2.10}$$

With the metric of U^P, a unitary transformation can be obtained as

$$\widetilde{U}^P \;\equiv\; P\widetilde{U}^P P \;=\; \frac{U^P}{\sqrt{U^{P\dagger}U^P}} , \tag{2.11}$$

with $\widetilde{U}^P\widetilde{U}^{P\dagger} = \mathbb{1}$. Note that the so-constructed transformation is identical to the unitary OLS transformation in Refs. [33, 34, 35], via which the effective Hamiltonian $H_{\rm eff} = \widetilde{U}^{P\dagger}H_{\rm diag}\widetilde{U}^P$ satisfies the decoupling condition $QH_{\rm eff}P = PH_{\rm eff}Q = 0$. The effective Hamiltonian in the P-space is then

$$H_{\rm eff} \;=\; \widetilde{U}^{P\dagger}H^P_{\rm diag}\widetilde{U}^P \;=\; \widetilde{U}^{P\dagger}(P\;UHU^\dagger\;P)\widetilde{U}^P , \tag{2.12}$$

Since we start with Hermitian H, it can be easily seen that $H_{\rm eff}$ is Hermitian as well. By construction, $H_{\rm eff}$ reproduces the spectrum in the P-space. For brevity, we define the OLS transformation as

$$U^P_{\rm OLS} \;\equiv\; \widetilde{U}^{P\dagger}PU , \tag{2.13}$$

[5] Specific caution needs to be taken that the determinant of U^P should be nonvanishing.

such that

$$H_{\rm eff} = U^P_{\rm OLS}\ H\ U^{P\dagger}_{\rm OLS}\ . \tag{2.14}$$

We remark that $H_{\rm eff}$ is not unique since there is the freedom of a residual P-space unitary transformation that preserves the sprectrum of $H_{\rm diag}$. Additional mathematical issues have been addressed in Ref. [50] such as the breakdown when linearly dependent projected eigenvectors are encountered. We did not encounter this breakdown in the calculations reported in this work.

A central issue for the current work is to investigate the effects of the corresponding transformation on the observables O needed to generate consistent renormalizations. That is, we define consistent effective operators [6]

$$O_{\rm eff} \ = \ U^P_{\rm OLS,f}\ O\ U^{P\dagger}_{\rm OLS,i}\ , \tag{2.15}$$

where $U^P_{\rm OLS,i}$ denotes the OLS transformation constructed from the bare Hamiltonian of the initial system, $H_{\rm i}$, while $U^P_{\rm OLS,f}$ is the OLS transformation constructed from the bare Hamiltonian of the final system, $H_{\rm f}$. The effective operator $O_{\rm eff}$ reproduces the corresponding full space calculation with the bare operator

$$\langle\phi_{\rm f}|O|\phi_{\rm i}\rangle \ = \ \langle\phi^P_{\rm eff,f}|O_{\rm eff}|\phi^P_{\rm eff,i}\rangle\ , \tag{2.16}$$

where $|\phi_{\rm i}\rangle$ and $|\phi_{\rm f}\rangle$ are eigenvectors of $H_{\rm i}$ and $H_{\rm f}$, which transform as

$$|\phi^P_{\rm eff,i}\rangle = U^P_{\rm OLS,i}\ |\phi_{\rm i}\rangle\ , \tag{2.17}$$

$$|\phi^P_{\rm eff,f}\rangle = U^P_{\rm OLS,f}\ |\phi_{\rm f}\rangle\ . \tag{2.18}$$

While these steps provide the formal framework, the essential question of a practical implementation requires further discussion. In the NCSM, one introduces an auxiliary confining potential, which is later removed, and solves for the OLS transformations on a subset of the nucleons in the nucleus (typically two or three nucleons) in what is dubbed a "cluster approximation" [9, 19, 20].

[6] Note that we are addressing a P-space which generally includes eigenstates with different conserved quantum numbers. The $U^P_{\rm OLS}$ transformation will properly manage scalar operators that conserve the symmetries of H as well as nonscalar operators that may induce transitions between eigenstates.

The derived few-nucleon effective interaction is designed to renormalize the strong few-nucleon correlations in the presence of other nucleons approximated by the auxiliary potential. This effective interaction is subsequently employed to define an A-nucleon effective Hamiltonian. The cluster approximation is guaranteed to produce the exact results as either the cluster size is increased to reach the full A-nucleon system or as the P-space truncation is removed. The two-nucleon cluster approximation of the NCSM serves as a paradigm for introducing and solving the NN systems of this work. Our aim is to investigate the ramifications of this approach for effective electroweak operators derived in a manner consistent with the softened interaction.

2.3 Results and discussions

To this stage, we have described the formal structure of the OLS method and we have discussed its applications within the NCSM. For the two-nucleon systems we address below, either without or with a HO trap, we apply the OLS approach in the relative coordinate system. Since the NN Hamiltonian is defined with the conserved symmetries of each NN partial wave (channel), we apply the OLS method to each NN channel independently. That is, we solve for individual OLS transformations in a relative HO basis of fixed total angular momentum, coupled spin, parity, and charge — the conserved quantum numbers for each NN channel. Then, we calculate the effective nonscalar operators with OLS transformations from the NN channels required for that operator.

2.3.1 Deuteron ground state

We define an initial system to consist of two nucleons described by the H [Eq. (2.1)]. We will discuss the ground-state energy of this system in this subsection. Motivated by the NCSM cluster approximation framework, we will define a second two-nucleon system in the next subsection that adds a confining HO interaction (trap). Both systems are numerically solvable. We refer to the numerical solutions of these two systems as their "exact" results. Using graphical representations, we compare these exact results with solutions from a truncation approach and with solutions from

an OLS effective Hamiltonian approach. We refer to the results from the truncation approach and the results from the OLS approach each as "model" results.

We adopt NN interactions from chiral EFT and we include the Coulomb interaction between proton pairs in the Hamiltonian. Specifically, we employ the NN interactions of the Low Energy Nuclear Physics International Collaboration (LENPIC) [37, 38, 39, 40, 41], which have been developed for each chiral order up through N^{4}LO. These LENPIC interactions employ a semilocal coordinate-space regulator and we select the interactions with the regulator range $R = 1.0$ fm [40, 41]. We refer to these interactions as "LENPIC-X", where "X" defines the specific chiral order (LO, NLO, N^{2}LO, N^{3}LO, or N^{4}LO). We also employ the chiral EFT interaction of Ref. [42] with momentum-space regulator 500 MeV, which we refer to as "Idaho-N^{3}LO". All of these chiral EFT interactions are charge dependent.

We consider the neutron-proton (np) system since the deuteron ground-state provides the only bound NN state. In particular, we solve for the deuteron ground-state energy for each interaction using three approaches. First, we obtain a high-precision result by diagonalizing the Hamiltonian in the coupled $[np; (^3S_1,\ ^3D_1)]$ channel in a very large HO basis ($N_{\max} = 400$) for three different values of the basis strength $\hbar\Omega$. We have verified that these ground-state energies produce the same result as the numerical solution of the Schrödinger equation to at least five significant figures [37, 38] in all cases. We refer to these results from diagonalization at $N_{\max} = 400$ as the "exact" results. One may view these exact results as creating a discretized approximation to the continuum and we note that the largest eigenvalues exceed 1 GeV in all cases investigated here. Second, we solve for the ground-state energy in the HO bases truncated at lower $N_{\max}$ values to produce model results for the simple truncation approach. Third, we solve for the OLS effective Hamiltonian at each value of $N_{\max}$ and $\hbar\Omega$, following the methods described above, to produce the model results for the OLS approach. We follow this same approach for the neutron-neutron (nn) and proton-proton (pp) channels needed for some of the transitions addressed in this work.

The model results of the truncation and OLS approaches are used to calculate their fractional difference with respect to our exact results for each observable (i.e., observables calculated with the

$N_{\max} = 400$ wave functions) where the fractional difference, Fract. Diff., is defined as the scaled difference $(model - exact)/|exact|$. The Fract. Diff. results for the deuteron ground state energy are presented as curves in Fig. 2.1 for a representative selection of our NN interactions. We do not show the results for LENPIC-LO since they are similar to the LENPIC-NLO results. Also, we do not show the LENPIC-N^{4}LO results, which are similar to those of LENPIC-N^{3}LO.

From the results in Fig. 2.1, we observe that the convergence rates for the truncation approach can depend significantly on the chiral order with the LENPIC NN interaction. In particular, there is a dramatic slowing of the convergence rates at N^{3}LO as seen in Fig. 2.1(c) compared to Figs. 2.1(a) and 2.1(b). The dependence of the convergence rates on the LENPIC chiral orders is also revealed in many-body observables where slower convergence leads to larger extrapolation uncertainties [39, 40, 41].

Table 2.1: (Adopted from Ref. [2]) Ground-state eigenvalues (in MeV) for the specified potentials used as the "exact" values in Fig. 2.1 as a function of the basis parameter $\hbar\Omega$ (in MeV).

Potential	$\hbar\Omega = 5$	$\hbar\Omega = 10$	$\hbar\Omega = 20$
LENPIC	-2.20607	-2.20609	-2.20609
LENPIC-N^{2}LO	-2.23508	-2.23516	-2.23516
LENPIC-N^{3}LO	-2.22324	-2.22326	-2.22326
LENPIC-N^{4}LO	-2.22458	-2.22459	-2.22458

Comparing the LENPIC NN interaction results in Fig. 2.1 also reveals changing shapes of the convergence patterns with increasing chiral order for the bases using basis parameter $\hbar\Omega = 5$ and 10 MeV. In particular, the case with $\hbar\Omega = 5$ MeV develops a region showing significantly reduced slope, nearly a plateau, with increasing $N_{\max}$ at N^{3}LO [Fig. 2.1(c)]. The results for the Idaho-N^{3}LO interaction shown in Fig. 2.1(d) indicate convergence patterns intermediate to LENPIC-N^{2}LO [Fig. 2.1(b)] and LENPIC-N^{3}LO [Fig. 2.1(c)]. These regions of reduced slope correspond to Fract. Diff ≈ 1.0, which defines a region of P-spaces where the lowest solution is transitioning between an

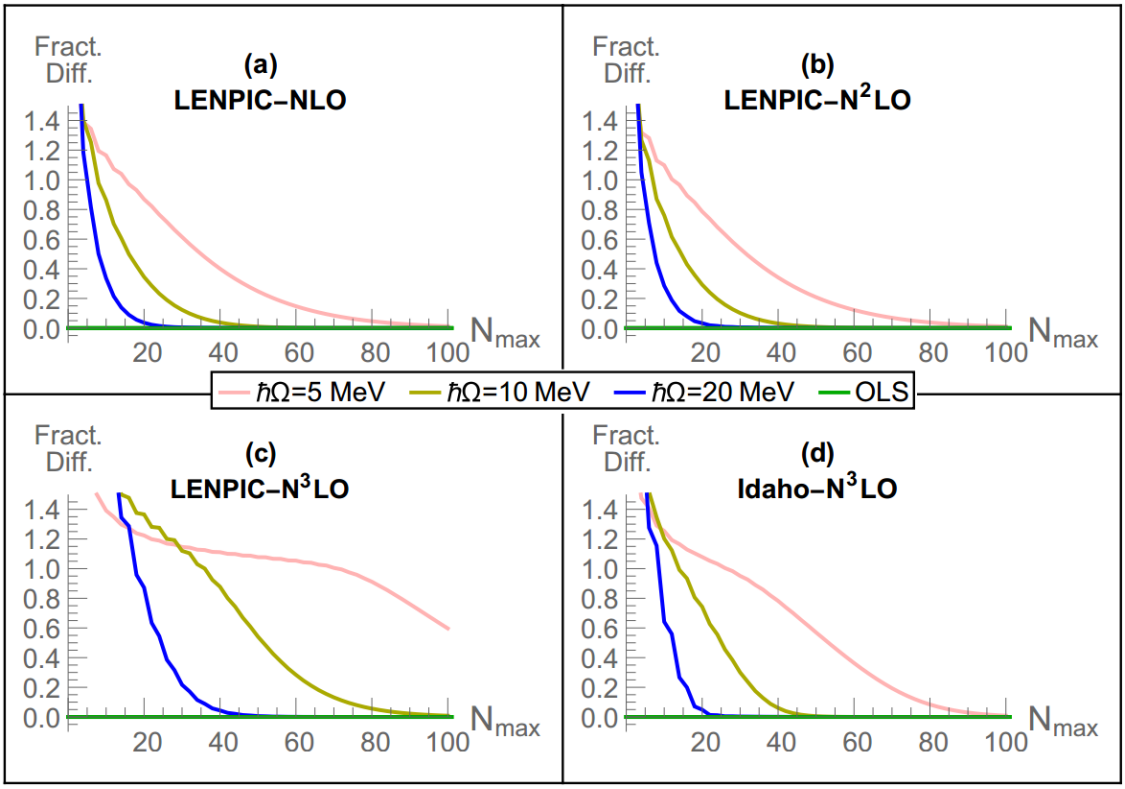

Figure 2.1: (Adopted from Ref. [2]) The fractional differences, where Fract. Diff. of an observable is defined as $(model - exact)/|exact|$, for the deuteron ground-state energy at three values of the basis parameter $\hbar\Omega$ as a function of the P-space limit $N_{\max}$. The model results from diagonalizing the P-space truncated Hamiltonian matrix produce Fract. Diff. curves that decrease towards zero with increasing $N_{\max}$ in accordance with the variational principle. The model results from diagonalizing the OLS-renormalized Hamiltonian matrix reproduce the exact results at each $N_{\max}$ to high precision, yielding flat and overlapping green lines for their Fract. Diff. plots in all cases. Panels (a), (b) and (c) correspond to the Hamiltonians constructed with the LENPIC chiral EFT interactions [37, 38, 39, 40, 41] at NLO, N^{2}LO, and N^{3}LO, respectively. We employ the LENPIC interactions with coordinate-space regulator $R = 1.0$ fm. Panel (d) corresponds to the Hamiltonian constructed with the Idaho-N^{3}LO potential [42] with momentum-space regulator 500 MeV. The exact ground-state energies are given in Table 2.1.

unbound state and a bound state with increasing $N_{\max}$. Thus, for some interactions at lower values of $\hbar\Omega$, we observe a plateau-like behavior as seen in Figs. 2.1(c) and 2.1(d). In these same cases, after crossing over to a bound-state solution, the convergence rate accelerates. We have investigated this plateau and have found a correlation with a changing feature of the wave function: while the solution is moving across the plateau with increasing $N_{\max}$, it is building up its d-state component from near zero to near its final value. When it nearly acquires its final value, the energy decreases to a bound state (Fract. Diff. falls below 1.0) and accelerates its convergence rate. We examined other interactions exhibiting this plateau in Fract. Diff. and found a similar correlation with buildup of the d-state probability. We anticipate that, at sufficiently low values of the basis $\hbar\Omega$, we would find a similar plateau with all realistic interactions for the deuteron.

The dependence of the convergence rate on the basis $\hbar\Omega$ for the truncation approach in Fig. 2.1 is systematic — from most rapid convergence at $\hbar\Omega = 20$ MeV to slowest at $\hbar\Omega = 5$ MeV. We have not sought to optimize the choice of $\hbar\Omega$, although that is often a point of interest in many-body applications. Our interest here is rather to feature results for a range of choices of $\hbar\Omega$ that will be useful for our investigation of electroweak observables in the system of the following subsection.

The Fract. Diff. for the results of the OLS approach in Fig. 2.1 always remains at zero, to within our numerical precision, which is what one anticipates. That is, since the OLS approach should provide the exact ground-state energy in any basis space, these results serve as a verification of our numerical procedures. The OLS procedure reproduces that subset of eigenvalues of the complete problem compatible with the dimensionality fixed by $N_{\max}$, including eigenvalues lying high in the continuum. We verify the accuracy of the eigenvalues from the OLS approach by direct comparison with the corresponding subset of results from the complete problem for each set of P-space basis parameters. We have confirmed that our OLS eigenvalues agree with the respective subset of the exact eigenvalues to at least six significant figures.

We now present additional observables for the deuteron that represent baseline results for later comparison. In Fig. 2.2 we show the ground-state energy [Fig. 2.2(a)], r.m.s. point-proton radius [2.2(b)], electric quadrupole moment [2.2(c)], and magnetic moment [2.2(d)] for the same set of

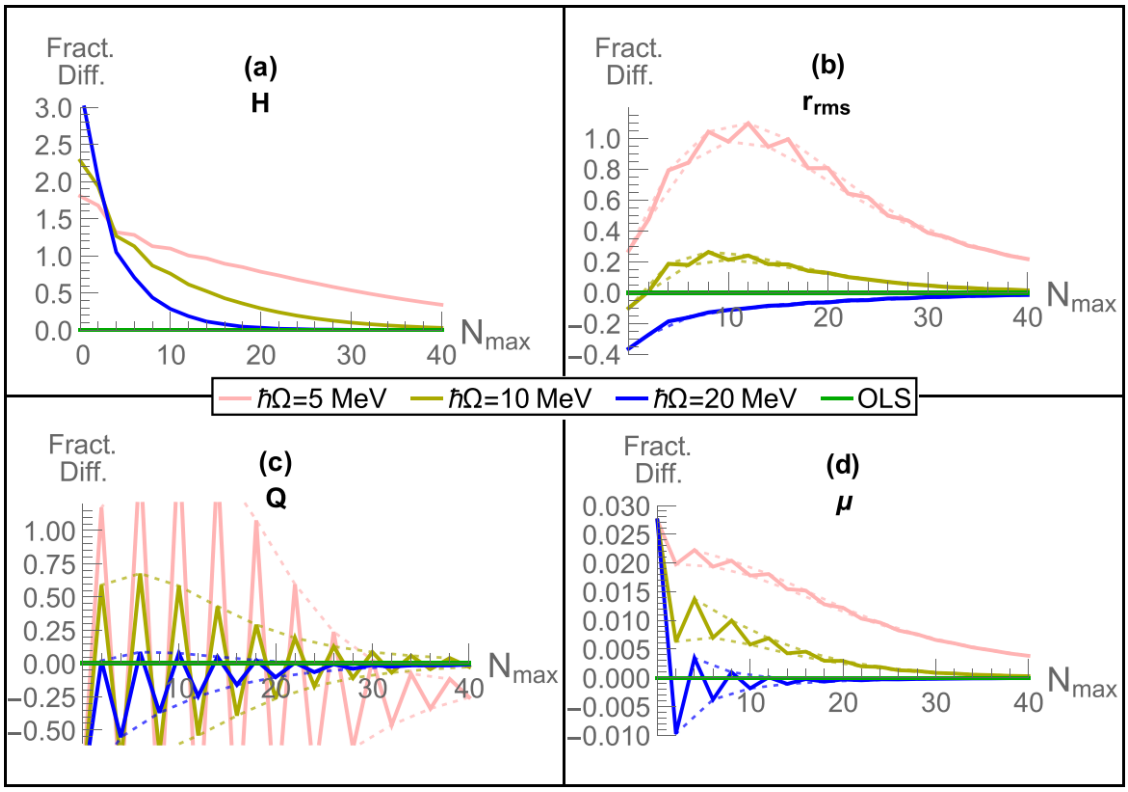

Figure 2.2: (Adopted from Ref. [2]) The fractional differences for a selection of deuteron properties at three values of the basis parameter $\hbar\Omega$ as a function of the P-space limit $N_{\max}$. Following the scheme of Fig. 2.1, we present the Fract. Diff. for the truncated basis calculations (three colored curves approaching zero at high $N_{\max}$) and for the OLS renormalized calculations (green curves all coincident with zero). All results are obtained with the LENPIC-N^{2}LO interaction with regulator $R = 1.0$ fm. The ground-state energy in panel (a) is an expanded version of the ground-state energy in panel (b) of Fig. 2.1. The r.m.s. point-proton radius $r_{\rm rms}$ appears in panel (b), the electric quadrupole moment Q in panel (c) and the magnetic moment μ in panel (d). The model results using the OLS transformation method reproduce the exact results at each $N_{\max}$ to high precision, yielding flat and overlapping green lines for their Fract. Diff. plots in all cases. The short dashed lines provide envelopes for results with "sawtooth" patterns. The exact values used for the observables here are given in Table 2.2.

3DHO basis parameters as in Fig. 2.1 using the LENPIC-N^{2}LO interaction. Here, we expand the scale to see details of the results from $N_{\max} = 0 - 40$. Clearly, the results in the truncated basis exhibit strong deviations from their exact values and those deviations exhibit nonsmooth behavior, such as sawtooth patterns, with increasing $N_{\max}$. The excursions in the electric quadrupole moment in Fig. 2.2(c) are especially prominent. These features represent the role of an s-state plus d-state combination that are added with each increase in $N_{\max}$ by 2 units. With the addition of two such combinations (increase $N_{\max}$ by four units) we include states with canceling asymptotic tails. This observation helps one to understand why results differing by 4 units in $N_{\max}$ follow a simpler trend in Fig. 2.2 — a trend visualized by the dotted line connecting the successive maxima and another dotted line connecting the successive minima of the "sawtooth" patterns. Such a visualization is also applied to the maxima and the minima of the sawtooth patterns of the other observables in Fig. 2.2, the r.m.s. radius [Fig. 2.2(b)] and magnetic moment [Fig. 2.2(c)]. Note that the scale for the magnetic moment is greatly enlarged relative to the other scales in Fig. 2.2 indicating it is rather insensitive to basis truncation effects.

Table 2.2: (Adopted from Ref. [2]) Ground-state eigenvalues and selected observables used as the "exact" values in Fig. 2.2 as a function of the basis parameter $\hbar\Omega$ (in MeV). The results are obtained with the LENPIC-N^{2}LO interaction with regulator $R = 1.0$ fm. No confining potential is included.

Ground-state observable	$\hbar\Omega = 5$	$\hbar\Omega = 10$	$\hbar\Omega = 20$
H (MeV)	-2.23508	-2.23516	-2.23516
$r_{\rm rms}$ (fm)	1.96440	1.96436	1.96436
Q $(e \cdot fm^2)$	0.269862	0.269874	0.269873
μ (μ_N)	0.856323	0.856323	0.856323

Here again, the calculations of the effective operators with the OLS method, when employed with the OLS wave functions in the same P-space, provide the exact results to within six digits for

each observable at each value of the trap. The OLS results are seen as the flat green lines at Fract. Diff. ≈ 0 in Fig. 2.2.

2.3.2 Two nucleons in HO trap ground-state energy

In this section, we investigate the effective electroweak operators of the two-nucleon systems. In view of the future applications to finite nuclei, we add a confining interaction (or trap) to the initial two-nucleon system in the previous section. In particular, we adopt a HO confining potential, where the effects of the confining potential are separated into the center-of-mass (COM) and the relative motions. Note that the COM and the relative motions exactly factorize. We hence consider only the relative motion of the two-nucleon system in the confining trap. The resulting Hamiltonian reads:

$$H = T_{\rm rel} + V + \frac{1}{2} M_{\rm red} \Omega^2 r^2 \ , \tag{2.19}$$

where $T_{\rm rel}$ and V denote the relative kinetic energy and the interaction of the two-nucleon system, respectively. $\frac{1}{2} M_{\rm red} \Omega^2 r^2$ denotes the confining HO trap, where r is the separation between the two nucleons, while $M_{\rm red} = \frac{1}{2}\widetilde{M}_N = 469.46$ MeV is the reduced mass of the two-nucleon system. In this work, we take the oscillator frequencies of the confining trap (Ω) to be the same as those of the basis values $\hbar\Omega = 5$, 10, and 20 MeV introduced in the discussion above.

The HO confining trap applied in this second system plays the role of simulating the effect of the nuclear medium in finite nuclei, in which the two-nucleon system is embedded. We tune the confining strength of the trap (also referred to as the trap strength in the following discussion) according to the properties of the nuclei: for example, we adopt weak (strong) trap strength for weakly (deeply) bound nuclei. In this work, we test the electroweak properties of the two-nucleon systems with the trap strengths of 5, 10 and 20 MeV. In addition, we remark that the application of the HO trap emulates the mathematical framework of the two-body cluster approximation in the NCSM, in which the HO trap is introduced in constructing the effective Hamiltonian and later removed in defining the effective interaction [9]. This auxiliary HO trap serves as a pseudo-potential to improve the convergence in NCSM applications with the OLS approach via the cluster

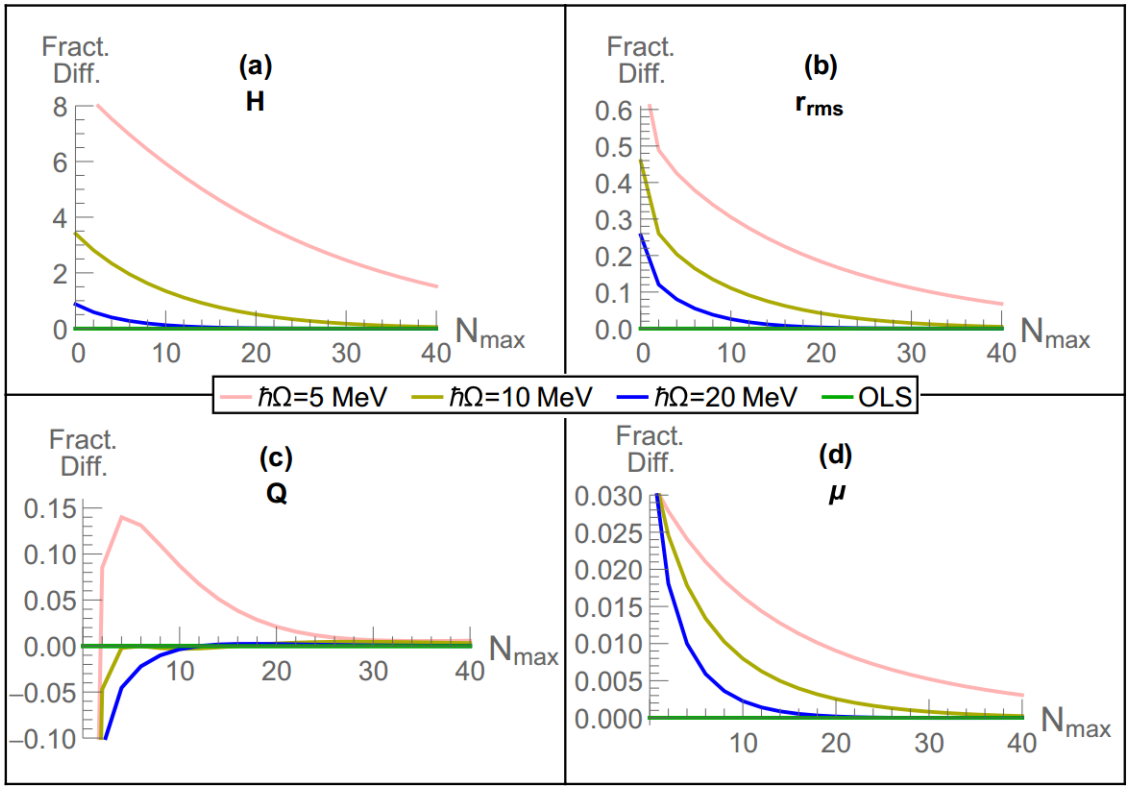

Figure 2.3: (Adopted from Ref. [2]) Fractional differences between model and exact results as a function of the P-space for selected ground-state observables of the two-nucleon system in the ${}^3S_1 - {}^3D_1$ channel for three different HO traps. The NN interaction is the LENPIC-N^{2}LO NN interaction with regulator $R = 1.0$ fm. The $\hbar\Omega$ for the bases correspond to the HO energies of the traps. The observables correspond to the eigenenergy (a), the r.m.s. point-proton radius (b), the electric quadrupole moment (c), and the magnetic dipole moment (d). The exact values used for the observables here are given in Table 2.3.

approximation. Overall, we anticipate that our study of the properties of a range of two-nucleon systems embedded in different HO traps will provide useful insights into the renormalization effects of various observables in future applications of the NCSM to the finite nuclei.

In testing this second two-nucleon system, we elect to retain only a subset of the LENPIC NN interactions for the simple purpose of demonstration. We show in Fig. 2.3(a) the ground-state energy of the two-nucleon system in the ${}^3S_1 - {}^3D_1$ channel (namely, neutron-proton system). The exact results are listed in Table 2.3. Due to the external trap, the corresponding exact results depend explicitly on the basis parameter $\hbar\Omega$ (also the trap strength) for the second system. The

convergence rate for the results via the truncation approach is systematic and increases with $\hbar\Omega$. Note that the scale for the Fract. Diff. in Fig. 2.3(a) is much larger than those in Fig. 2.1. Nevertheless, we again find good agreement between the results via the OLS approach and the exact ground-state energy results over all choices of P-space, which can be seen from the coincident flat green lines at Fract. Diff. $= 0$.

Table 2.3: (Adopted from Ref. [2]) Ground-state eigenvalues and selected observables used as the "exact" values in Fig. 2.3. The results were obtained with the LENPIC-N^{2}LO interaction with regulator $R = 1.0$ fm. The parameter of the confining HO potential is the same as the basis parameter $\hbar\Omega$ (in MeV) that labels each column of results.

Ground-state observable	$\hbar\Omega = 5$	$\hbar\Omega = 10$	$\hbar\Omega = 20$
H (MeV)	-0.703487	2.35148	10.7332
$r_{\rm rms}$ (fm)	1.44078	1.20869	0.992923
Q $(e \cdot fm^2)$	0.204165	0.164676	0.122359
μ (μ_N)	0.852184	0.849597	0.84814

2.3.3 Two nucleons in HO trap — Electromagnetic observables

We now investigate additional observables in the second system. Our focus is, again, to compare the truncation approach with the OLS approach. As reported in Refs. [44, 45, 46], the results of various long-range observables computed via the truncation approach is within the range from a few percent to about 10% compared to those computed via the OLS approach. We intend to demonstrate the truncation effect, as well as the renormalization effect, of various electroweak observables with the second two-nucleon system. Comparing the truncation and OLS approaches, we find large renormalization effects for the matrix elements of some observables in cases where the trap strength is small, and/or where the basis space is small (limited $N_{\rm max}$). This suggests that, for the observables involving weakly bound states and the transitions involving resonance states, the truncation effects are severe, so that the renormalization becomes important and necessary.

We again examine the ground-state variables such as the energy, the r.m.s. point-proton radius $r_{\rm rms}$, quadrupole moment Q, and magnetic dipole moment μ as initial tests. Due to the extra harmonic confining trap, the wave functions of the second two-nucleon system possess the gaussian type of asymptotic properties. The long-range contributions to the matrix element of long-range observables are hence moderated. Note that in the real nuclear environment of bound state nuclei, however, such asymptotic properties of the wave functions are exponential and will therefore generate more significant contributions to the matrix element of the long-range observables.

We calculate the ground-state expectation values of these operators via both the truncation approach and the OLS approach. The results are shown in Fig. 2.3 as the fractional difference from the exact results (Table 2.3) obtained in $N_{\rm max} = 400$ calculations. We note the major differences in the scales of the Fract. Diff. results in Fig. 2.3; the truncation effects are largest for the ground-state energy and decrease in size in the sequence of $r_{\rm rms}$, Q, and μ. We also find that the truncation effects increase with decreasing trap strength. This can be interpreted as arising from the competing roles of the external HO trap and the NN interaction in the Hamiltonian. As the trap strength increases, the role of the NN interaction in the Hamiltonian becomes less dominant; the second two-nucleon system simply resembles the HO Hamiltonian with a sufficiently large trap strength ($\hbar\Omega$ =20 MeV in this case). In addition, we find that the "sawtooth" behavior of the results from the truncation approach seen in Fig. 2.2 (without the HO confining potential) is absent from Fig. 2.3 — the generally smooth trend is present for the results computed via the truncation approach. While the truncation results of the ground-state energy, $r_{\rm rms}$ [Fig. 2.3(b)] and μ [Fig. 2.3(d)] present a monotonic convergence pattern, the convergence pattern of Q is more complicated: the Fract. Diff. of Q in the truncation approach still shows a sign change for all the choices of trap strength. This sign change becomes less visible with increasing trap strength.

Meanwhile, we again find good agreement between the ground-state observables in Fig. 2.3 via the OLS approach and respective exact results over all choices of P-spaces and traps. This is evident from the coincident green lines remaining zero in all panels. Indeed, we checked and found that the Fract. Diff. for all the OLS results are zero to at least six significant digits.

2.3.4 Two nucleons in HO trap — Weak observables

Table 2.4: (Adopted from Ref. [2]) Ground-state transition matrix elements used as the "exact" values in Figs. 2.4 and 2.5. The strength of the confining HO potential is the same as the basis parameter $\hbar\Omega$ (in MeV) that labels each column of results. The GT transition matrix element values correspond to the $N_{\max} = 400$ case, where they have converged to six or more significant digits. The $0\nu2\beta$ transition matrix element values correspond to the $N_{\max} = 200$ case, where they have converged to four or more significant digits.

Decay	Potential	$\hbar\Omega = 5$	$\hbar\Omega = 10$	$\hbar\Omega = 20$
GT	NLO	−1.40355	−1.42839	−1.43974
	N^{2}LO	−1.40338	−1.42902	−1.44106
$0\nu2\beta$	NLO	1.59067	0.505287	0.827882
	N^{2}LO	1.48274	0.476412	0.792684

We now investigate the truncation effect and the renormalization effect of the weak operators of the two-nucleon system confined in the HO trap. For a demonstration, we first consider the Gamow-Teller (GT) β-decay matrix element for the transition between the ground states of the $^1S_0$ nn channel and the $^3S_1 - ^3D_1$ np channel. We take the GT operator to be of the simple spin-isospin form [51].[7] Two NN interactions of lower chiral orders, namely, the LENPIC-NLO NN interaction and the LENPIC-N^{2}LO NN interaction, are adopted for the purpose of illustration. The corresponding results are shown in Fig. 2.4(a) and Fig. 2.4(b), respectively.

As seen from the Fract. Diff. for the GT matrix elements (Figs. 2.4(a) and 2.4(b)), the convergence pattern of the results via the truncation approach is similar to that of the operators in Figs. 2.3(a), 2.3(b) and 2.3(d), but with the opposite sign. The exact results are shown in Table 2.4 for completeness. Note that there is an overall negative sign for all the GT matrix elements. We

[7] In the future, we will employ operators, including the GT operators, that are derived consistently from the chiral EFT.

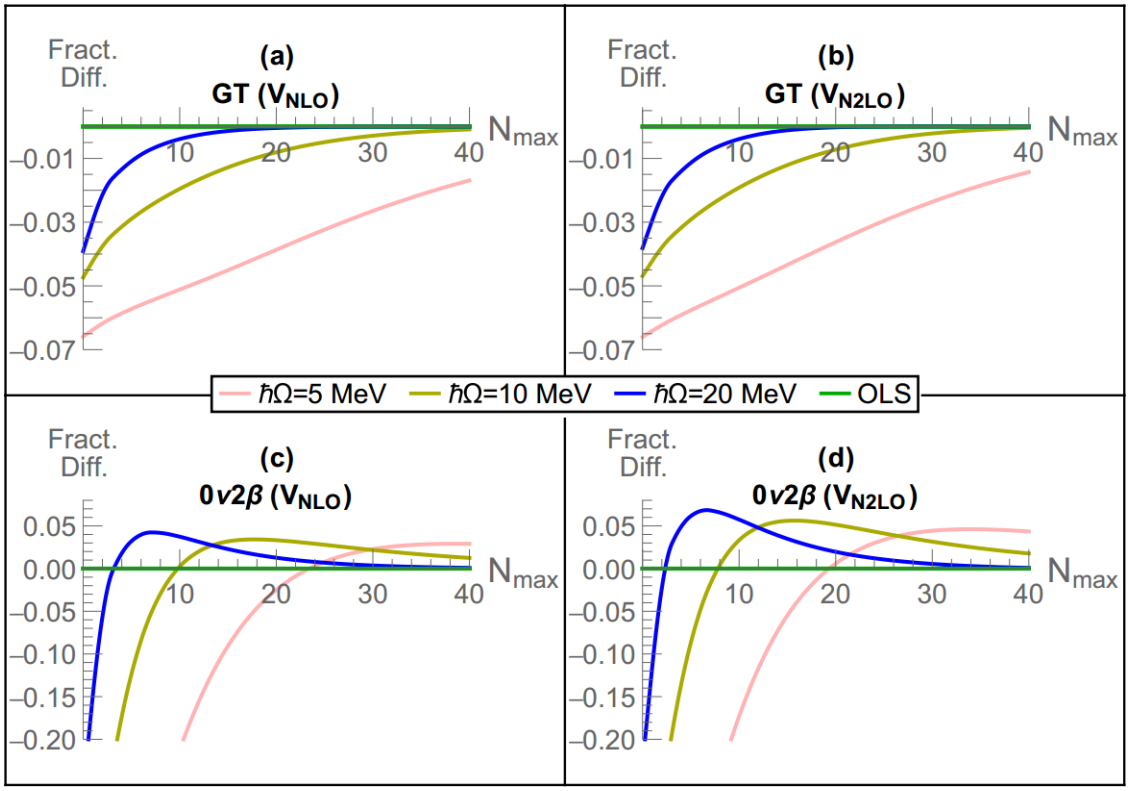

Figure 2.4: (Adopted from Ref. [2]) Fractional differences between model and exact results as a function of the P-space for selected ground-state transitions from the lowest state of the $^1S_0$ nn system in three different HO traps. Panels (a) and (b) are for the allowed GT transition to the ground state of the $^3S_1 - ^3D_1$ channel. Panels (c) and (d) are for the $0\nu2\beta$-decay to the ground state of the $^1S_0$ pp system. The NN interaction for cases (a) and (c) are taken to be the LENPIC-NLO potential, while we adopt the LENPIC-N^{2}LO potential for cases (b) and (d). All results shown employ LENPIC NN interactions with coordinate space regulator $R = 1.0$ fm. The exact values used for the observables here are given in Table 2.4.

remark that the negative sign is arbitrary and results in no physical consequence. As the P-space dimension increases, the results via the truncation approach converge to the exact results from below, producing the trends in Figs. 2.4(a) and 2.4(b). Therefore, the results via the truncation approach with restricted basis space would necessitate the application of a scaling factor, or a quenching factor (less than unity), in order to match the exact results. For clarification, we present the plots of this quenching factor (defined as the *exact*/*model*) in Figs. 2.5(a) and Fig. 2.5(b) based on the results in Figs. 2.4(a) and 2.4(b). We find the quenching factors of the GT matrix elements deviate from unity by about 6% at most. Smaller quenching factors are obtained for the cases with smaller trap strengths, where the confinement of the nn and np systems is weaker. In other words, the GT quenching factor is smaller (relative to unity) with increasing spatial distribution of the two-nucleon system (i.e. decreasing $\hbar\Omega$), which resembles the phenomenological decrease in the quenching factor (i.e. trending lower than unity), of the valence-space GT-transition matrix elements with increasing atomic number [52]. As for the OLS approach, we again find that the exact GT results are reproduced for all our choices of P-space and trap strength. This is evident from the overlapping green lines at zero in Figs. 2.4(a) and 2.4(b), or, equivalently, at unity in Figs. 2.5(a) and 2.5(b).

Via the same approach used in studying the GT transitions, we study the $0\nu2\beta$-decay matrix element for the transition between the ground states of the $^1S_0$ nn channel and the $^1S_0$ pp channel. As before, three HO traps (of trap strength 5, 10, 20 MeV) and two low-order chiral interactions are adopted for the second two-nucleon system. The $0\nu2\beta$-decay operator is derived from chiral EFT in Ref. [53], which is consistent with the chiral NLO (the expression of the $0\nu2\beta$ operator in the 3DHO representation is shown in Appendix A.9). The corresponding results are shown in Figs. 2.4(c) and 2.5(c) (with LENPIC-NLO) and Figs. 2.4(d) and 2.5(d) (with LENPIC-N^{2}LO). In calculating the exact results (shown in Table 2.4), we employ a basis space with $N_{\max} = 200$ for good convergence. Note that we elect not to apply the LENPIC semi-local coordinate-space regulator to this $0\nu2\beta$ operator, since this regulator is not gauge invariant.

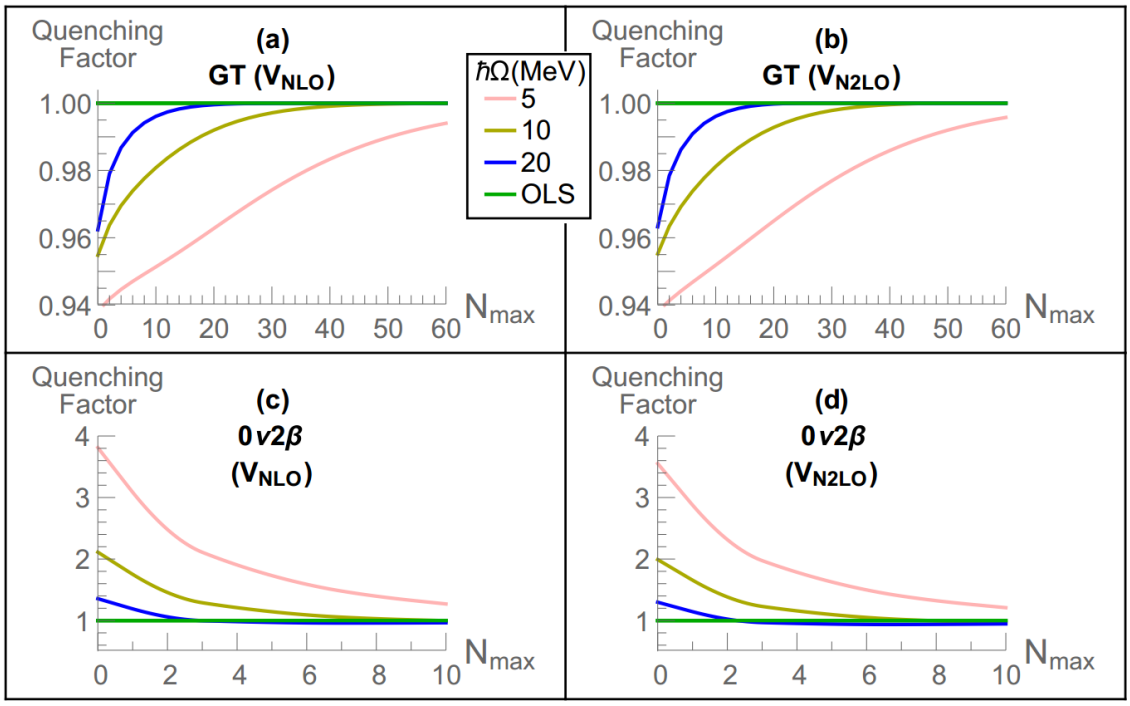

Figure 2.5: (Adopted from Ref. [2]) Quenching factor defined as *exact*/*model* for GT-decay and $0\nu2\beta$-decay matrix elements as a function of the P-space for ground-state transitions from the lowest state of the $^1S_0$ nn system in three different HO traps. Panels (a) and (b) are for the allowed GT-transition to the ground state of the $^3S_1 - ^3D_1$ channel. Panels (c) and (d) are for the $0\nu2\beta$-decay to the ground state of the $^1S_0$ pp system. The NN interaction for cases (a) and (c) are taken to be the LENPIC-NLO potential, while we adopt the LENPIC-N^{2}LO potential for cases (b) and (d). All results shown employ LENPIC NN interactions with coordinate space regulator $R = 1.0$ fm. A quenching factor greater than unity signals an enhancement of the model results is required to arrive at the exact results. The exact values used for the observables here are given in Table 2.4.

We find that the convergence patterns of the $0\nu2\beta$-decay results via the truncation approach are sensitive to the trap strength. The Fract. Diff. results in Fig. 2.4 do not appear to approach zero (which indicates the convergence of the model-space calculations) until $N_{\max}$ reaches 10, 20, 40 for $\hbar\Omega = (20, 10, 5)$ MeV, respectively. As $N_{\max}$ increases, these convergence patterns are similar but not monotonic. We find the magnitude of the results via the truncation approach are much smaller than the exact results when $N_{\max}$ is small, which means that the $0\nu2\beta$-decay results via the truncation approach would be largely suppressed in truncated and limited model spaces.

The results of the corresponding quenching factors via the truncation approach are shown in Figs. 2.5(c) and 2.5(d). Contrary to the quenching factors of the GT matrix elements, we find that the quenching factors rise significantly above unity for small basis space (small $N_{\max}$). For weaker HO trap strength, this rise is larger. This indicates that, when evaluated via the truncation approach, significant contributions from the intermediate-range components of our $0\nu2\beta$ operator are missing for the cases with restricted basis space. Also, larger quenching factors (acting as enhancements here) would be necessary for the $0\nu2\beta$-decay in weakly bound nuclei.

As for the OLS approach, we again find that the exact $0\nu2\beta$ results are reproduced for all the choices of P-space and trap strength. This can be seen from the Fract. Diff. results (coincident green lines) at zero in Figs. 2.4(c) and 2.4(d), or from the quenching factor results (coincident green lines) at unity in Figs. 2.5(c) and 2.5(d). It is worth noting that the OLS transformation is defined separately for the initial and final states of transitions (GT- and $0\nu2\beta$-decays in this work). Indeed, to reproduce the exact results of the transition matrix elements for all model spaces via the OLS approach is a nontrivial benchmark test of our numerical procedures.

CHAPTER 3. TIME-DEPENDENT BASIS FUNCTION METHOD

3.1 Introduction

A unified treatment of nuclear structure and reactions is a central, but challenging, issue of *ab initio* nuclear theory. Specifically, the challenge is to incorporate the discrete bound states with the scattering states in the continuum [54, 55]. For few-body systems with mass number $A \leq 4$, highly precise methods such as Faddeev [56], Faddeev-Yakubovsky [57, 58], Alt-Grassberger and Sandhas [59, 60], and hyperspherical harmonics [61, 62] have been developed using internal coordinates. As for light and medium nuclei with $A > 4$, there are also a wealth of cutting edge approaches. A survey of the methods includes the no-core shell model with resonating group method [63, 64, 65, 66], the no-core shell model with continuum method [67, 68, 69], the coupled cluster method with the Gamow basis [70, 71, 72], the no-core shell model with the Gamow basis [73, 74, 75], the HORSE (J-matrix) method [76, 77, 78], the configuration interaction with resonating group method [79], the Green's function Monte Carlo method [80, 81], and the nuclear lattice effective field theory [82, 83]. However, these successful methods may be challenged to retain the full, non-perturbative quantum coherence of the scattering over all potentially relevant intermediate and final states which could be important for complex scattering processes involving exotic nuclei. For short-lived rare isotopes, where the low-lying states are either weakly bound or unbound, one will be challenged to include the relevant degrees of freedom for a complete description of the inelastic processes. In particular, a large number of intermediate states may be needed to provide accurate descriptions of the dynamical multi-step processes contributing to the final states.

In order to address these complex processes and retain predictive power, we propose an *ab initio*, time-dependent non-perturbative approach, which we call the time-dependent Basis Function (tBF) approach. The idea, which is based on a successful time-dependent approach in quantum field theory [84, 85, 86, 87, 5], is to solve the equation of motion (EOM) for the scattering of the system in the

representation constructed from the energy eigenbases of the system before scattering. The state vector for the system hence reduces to a set of amplitudes with respect to the chosen eigenbases, in which the full coherence is retained, and the EOM becomes a set of first order differential equations in time.

We demonstrate the tBF approach with a very simple problem, the internal excitation of a trapped deuteron in the time-varying external Coulomb field of a heavy ion, or deuteron Coulomb excitation [88, 89]. Note in this initial application, the motion of the COM of the deuteron is constrained to the trap and the excitation in the COM degree of freedom is neglected. Future work will remove the trap and evolve the motion of the COM. Within the tBF formalism, the evolution of the deuteron system is examined through its consequent transition probabilities and through expectation values of different observables during the scattering. The dynamics of the scattering process will also be revealed by the time evolution of the deuteron system's internal charge density distribution.

This chapter is essentially the published paper [4]. It is organized in the following way. We first introduce the theory of the tBF approach in Sec. 3.2. Then, we discuss the details of our model problem in Sec. 3.3 and present the simulation conditions of the problem in Sec. 3.4. Later, we provide illustrative numerical results in Sec. 3.5.

3.2 Theory

We begin with an introduction of the framework for time-dependent scattering within a basis space determined from an *ab initio* structure calculation. In particular, we outline the problem where the external field, which induces the transitions, is treated as a classical, possibly strong, time-dependent electromagnetic (EM) source. The generalization to more complex sources will be considered in subsequent works. To be concrete and simple, we outline the approach for the specific case of a trapped deuteron as the system undergoing excitation, which, however, can be straightforwardly generalized.

3.2.1 Hamiltonian

Our full Hamiltonian for the target scattered by the time-varying EM field produced by the impinging heavy ion (HI) is

$$H_{\rm full}(t) \;=\; H_0 + V_{\rm int}(t)\ , \tag{3.1}$$

where the Hamiltonian for the intrinsic motion of the target is

$$H_0 \;=\; T_{\rm rel} + V_{\rm NN} + U_{\rm trap}\ , \tag{3.2}$$

with $T_{\rm rel}$ the relative kinetic energy and $V_{\rm NN}$ the nucleon-nucleon (NN) interaction. $U_{\rm trap}$ denotes an external HO trap introduced to localize the COM of the target and to discretize the continuum of the target's scattering states. We neglect the excitation of the COM motion. Removing the regularization provided by the trap will be the subject of future investigations.

For physical motivation to retain a weak trap, one may cite the utility of a quasi-deuteron approach to reactions as an example. In that case, the presence of our trap simulates a nuclear environment in which the deuteron degree of freedom is selected to respond to an external probe [90].

The time-dependent interaction between the target and the external EM field is $V_{\rm int}(t)$, which is formulated by the coupling between the four current $J^\mu = (\rho,\ \vec{j})$ of the target and the four potential $A^\mu = (\varphi,\ \vec{A})$ of the external EM field

$$V_{\rm int}(t) \;=\; \int A_\mu J^\mu\ d\vec{r} \;=\; \int \rho(\vec{r},t)\varphi(\vec{r},t)\ d\vec{r} \;-\; \int \vec{j}(\vec{r},t)\cdot\vec{A}(\vec{r},t)\ d\vec{r}\ \ . \tag{3.3}$$

Note we adopt the natural units and set $\hbar = c = 1$ throughout this chapter.

3.2.2 EOM for the scattering

The EOM for the target during the scattering, in the interaction picture, is

$$i\frac{\partial}{\partial t}|\psi;t\rangle_I \;=\; e^{iH_0t}\ V_{\rm int}(t)\ e^{-iH_0t}\ |\psi;t\rangle_I \;\equiv\; V_I(t)\ |\psi;t\rangle_I\ , \tag{3.4}$$

where $V_I(t)$ denotes the interaction part in the full Hamiltonian. The subscript "I" specifies the interaction picture. The state vector of the target at time $t \geq t_0$ (t_0 is the time when the target is defined in its initial state and begins to experience the time-dependent interaction) can be solved as

$$|\psi;\ t\rangle_I \quad = \quad U_I(t;t_0)|\psi;\ t_0\rangle_I \quad , \tag{3.5}$$

where $U_I(t;t_0)$ is the unitary operator for the time-evolution

$$U_I(t;t_0) \quad = \quad \hat{T}\left\{ \exp\left[-i \int_{t_0}^{t} V_I(t')\ dt' \right] \right\} , \tag{3.6}$$

with $\hat{T}$ the time-ordering operator towards the future.

The time-evolution operator $U_I(t;t_0)$ can be evaluated numerically by first dividing the interval $[t_0, t]$ into segments with step length $\delta t = (t - t_0)/n$ (n being sufficiently large to attain numerically stable results) and then replacing the integration in the exponent with additive increments. Keeping only terms up to the order of δt in the following Taylor expansion, we get

$$U_I(t;t_0) \xrightarrow{\sum \delta t} \left[1 - i\ V_I(t)\delta t\right] \left[1 - i\ V_I(t_{n-1})\delta t\right] \ \cdots \ \left[1 - i\ V_I(t_1)\delta t\right] . \tag{3.7}$$

The direct evaluation according to Eq. (3.7) is called the Euler scheme. It is numerically unstable since this scheme is not symmetric in time; the norm of the state vector of the target may not be conserved [91] during the evolution. We therefore adopt the MSD2 scheme [92] in our tBF method. Via the MSD2 scheme, the state vector for the target at the time $t_1 = t_0 + \delta t$ is still evolved via the Euler scheme. However, for $t' = t_2, t_3, \cdots, t_{n-1}$, the state vector under time evolution is

$$|\psi; t' + \delta t\rangle_I \quad \approx \quad |\psi; t' - \delta t\rangle_I - 2i\ V_I(t')\ \delta t\ |\psi; t'\rangle_I \ . \tag{3.8}$$

For the current model problem, we also calculate the state vector of the target via first-order perturbation theory for comparison

$$|\psi;\ t\rangle_I \quad \rightarrow \quad \left[1 - i\ \Big(V_I(t) + \cdots V_I(t_2) + V_I(t_1)\Big)\delta t\right] |\psi;\ t_0\rangle_I \ , \tag{3.9}$$

where only the terms up to the order of δt are retained.

3.2.3 Basis representation

We solve the energy eigenbases of the target from its intrinsic Hamiltonian (Eq. (3.2)). The eigenequation is

$$H_0|\beta_j\rangle \quad = \quad E_j \ |\beta_j\rangle, \tag{3.10}$$

where E_j is the eigenvalue corresponding to the eigenvector $|\beta_j\rangle$ and the subscript j is an index running over the individual states. In the basis representation defined by the set of bases $\{|\beta_j\rangle\}$, the state vector of the target becomes a vector of time-dependent amplitudes, while the operators become matrices and the EOM (Eq. (3.4)) becomes sequential matrix-vector multiplications.

3.2.4 Transition amplitude

In the basis representation, the state vector of the target at any moment t during the scattering is

$$|\psi;t\rangle_I \quad = \quad \sum_j A_j^I(t)|\beta_j\rangle \ , \tag{3.11}$$

where the $A_j^I(t)$ is the amplitude corresponding to the basis $|\beta_j\rangle$. Given the initial state vector of the target at the beginning of the scattering ($t = t_0$) to be $|\psi;t_0\rangle = |\beta_i\rangle$, $A_j^I(t)$ describes the transition amplitude from $|\beta_i\rangle$ to $|\beta_j\rangle$ and can be computed as

$$A_j^I(t) \quad = \quad \langle\beta_j|U_I(t;t_0)|\beta_i\rangle \ , \tag{3.12}$$

with $A_j^I(t_0) = \delta_{ij}$. The corresponding transition amplitude in the Schrödinger picture is

$$A_j(t) \quad = \quad \exp\Big[-iE_jt + iE_it_0\Big]A_j^I(t) \ , \tag{3.13}$$

and the full state vector of the target at time t is

$$|\psi;t\rangle \quad = \quad \sum_j A_j(t)|\beta_j\rangle \ . \tag{3.14}$$

3.2.5 Observables and the density distribution

Based on $|\psi;t\rangle$, we can calculate the expectation values of observables during the scattering as

$$\langle O(t)\rangle \;=\; \langle\psi;\ t|\ \hat{O}\ |\psi;\ t\rangle \;=\; \sum_{j,k} A_j^*(t)A_k(t)\ \langle\beta_j|\hat{O}|\beta_k\rangle\ , \tag{3.15}$$

where $\hat{O}$ denotes the operator for the selected observable.

As an example, we can study the dynamics of the target via the evolution of its effective charge density distribution, which is formulated as

$$\rho(\vec{r};t) \;=\; \langle\psi;t|\vec{r}\rangle\langle\vec{r}|\psi;t\rangle \;=\; \sum_{jk} A_k^*(t)A_j(t)\langle\beta_k|\vec{r}\rangle\langle\vec{r}|\beta_j\rangle\ , \tag{3.16}$$

where $\langle\vec{r}|\beta_j\rangle$ denotes the wave function of the j^{th} basis in coordinate space. The charge density distribution of the target in its relative coordinates will be simply referred to as the internal charge distribution in the following text.

3.3 Setup of the model problem

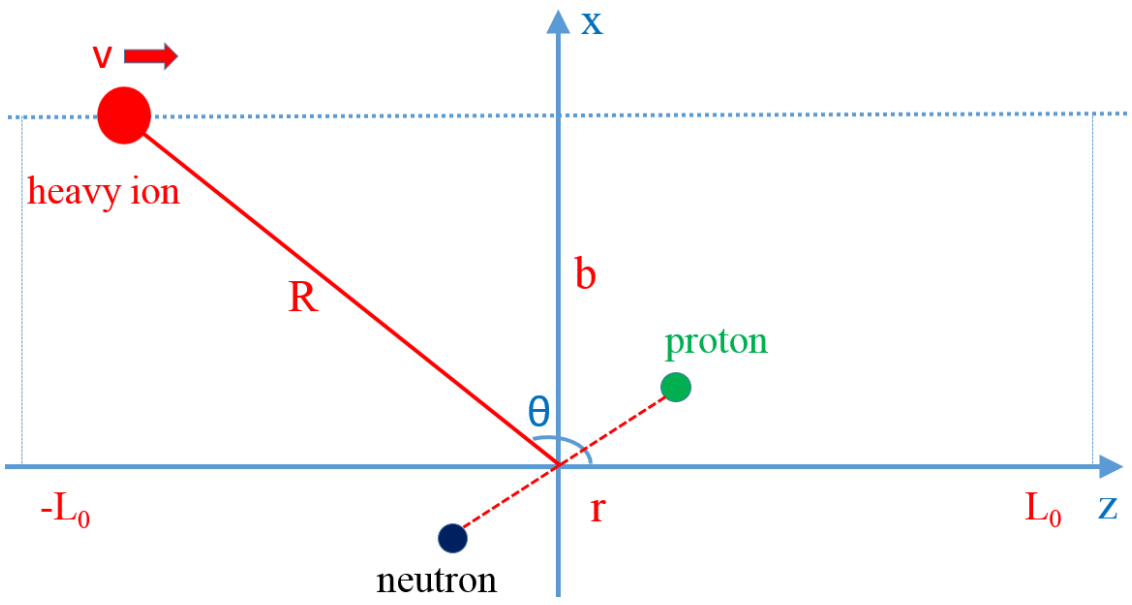

Figure 3.1: (Adopted from Refs. [4, 5]) Set up of the peripheral scattering. See the text for the details.

As shown in Fig. 3.1, we set the scattering plane to be the xz-plane. The target is a deuteron. For simplicity, we assume its COM is fixed at the origin, i.e., the recoil of the target during the scattering is neglected. The relative coordinates of the target are defined as $\vec{r} = \vec{r}_p - \vec{r}_n$, where $\vec{r}_p$ and $\vec{r}_n$ are the single-particle coordinates for the proton and the neutron, respectively. The masses of the neutron and the proton are taken to be their average mass 938.92 MeV. The mesonic degree of freedom is not considered and the unit charge of the target is carried by the proton.

The projectile is a HI. It carries charge Ze and is assumed to move, for simplicity here, with a constant velocity $\vec{v}$ parallel to the $\hat{z}$-axis. The impact parameter b is set to be sufficiently large such that the nuclear interaction is negligible compared to the EM interaction during the scattering. $\vec{R}$ denotes the position of the HI with respect to the origin.

3.3.1 Background field

As an initial application of the tBF method, we assume that the HI impinges with a low speed (non-relativistic) and the magnetic interaction between the target and the induced vector field $\vec{A}(\vec{r}, t)$ is ignored. That is, we evaluate only the interaction between the target and the time-varying Coulomb field. We then perform the multipole expansion of the Coulomb field [93] and, for this initial application, we retain only the contribution of the $E1$ multipole component. The investigation on the contributions of other components (e.g., $E0$, $E2$) as well as the magnetic transitions (e.g., $M1$) will be addressed in the future.

In the basis representation, the operator for the $E1$ multipole component [88, 94] of the time-varying Coulomb interaction $V_I(t)$ becomes a matrix with elements formulated as

$$\langle \beta_j | V_I(t) | \beta_k \rangle \quad = \quad \frac{4\pi}{3} Z e^2 e^{i(E_j - E_k)t} \sum_{\mu} \frac{Y^*_{1\mu}(\Omega_R)}{|R(t)|^2} \int d\vec{r} \, \langle \beta_j | \vec{r} \rangle \, \frac{r}{2} Y_{1\mu}(\Omega_r) \, \langle \vec{r} | \beta_k \rangle \ , \qquad (3.17)$$

where $Y_{\lambda\mu}(\Omega)$ denotes the spherical harmonics (the Condon-Shortley convention [95, 96] is adopted in this work). $\lambda = 1$ denotes the dipole contribution out of the multipole components of the Coulomb field. Ω_R denotes the direction of the HI, which is specified by the polar angle and the azimuth angle of $\vec{R}$. Similarly, Ω_r is specified by the polar and azimuth angles of $\vec{r}$. The matrix representation for the time-evolution operator $U_I(t; t_0)$ can thus be solved according to Eq. (3.17).

3.3.2 Structure calculation of the target

In our tBF method, we solve for target properties by an *ab initio* nuclear structure calculation. In this work, the three dimensional (spherical) harmonic oscillator (3DHO) representation in relative coordinates is implemented to calculate the eigenenergies and the corresponding eigenbases. For the internal motion of the deuteron system, each 3DHO basis $|nlSJM\rangle$ is specified by the radial quantum number n, the quantum number l for the orbital angular momentum, the quantum number S for the spin, the quantum number J for the total angular momentum (we adopt the scheme where l is coupled to S to form J) and the magnetic quantum number M for the $\hat{z}$-projection of the total angular momentum. Note that the $E1$ multipole component does not act on the isospin degree of freedom; we hence omit the isospin part of the 3DHO basis in this work. The truncation parameter for the model space is defined by $2n + l \leq N_{\max}$. Hence the model's 3DHO basis set $\{|nlSJM\rangle\}$ is specified by good quantum numbers S, J, M and parity (determined by $(-1)^l$) of the np system. We thus define our retained eigenbasis in Eq. (3.10) as

$$|\beta_j\rangle \quad = \quad \sum_{n_j l_j} a_{n_j l_j} |n_j l_j S_j J_j M_j\rangle \ , \tag{3.18}$$

where β stands for l, S, J and M for each channel. $\{a_{n_j l_j}\}$ denotes the set of the expansion coefficients, which are obtained by the diagonalization of the matrix H_0 in the 3DHO representation. The kernel in Eq. (3.15) thus becomes

$$\langle \beta_j | \hat{O} | \beta_k \rangle \quad = \quad \sum_{n_j l_j} \sum_{n_k l_k} a^*_{n_j l_j} a_{n_k l_k} \langle n_j l_j S_j J_j M_j | \hat{O} | n_k l_k S_k J_k M_k \rangle \ . \tag{3.19}$$

Details of our conventions for the 3DHO basis representation, the EM operators and the observables employed here in the 3DHO basis are presented in Appendix A.

3.4 Simulation conditions

In this work, we will adopt a concrete but simple test application to demonstrate the feasibility of the tBF method and to gain an initial appreciation of the coherent features available in time-dependent evolution at the amplitude level. The projectile is taken as a fully stripped uranium,

U^{92+}. The incident speeds are set to be 0.1, 0.2 and 0.4. We fix the duration of exposure time to be from -5 MeV^{-1} to 5 MeV^{-1}, which is approximately 6.582×10^{-21} sec. The impact parameter is chosen as $b = 5$ fm. That is, as an example, the projectile with the incident speed $v = 0.1$ travels from 100 fm before the distance of the closest approach between the projectile and the origin to 100 fm after the closest approach.

$$\begin{pmatrix} (^3S_1,^3D_1) & M=-1 & -0.65289\ \text{MeV} \\ (^3S_1,^3D_1) & M=\ 0 & -0.65289\ \text{MeV} \\ (^3S_1,^3D_1) & M=+1 & -0.65289\ \text{MeV} \\ ^3P_0 & M=\ 0 & 12.0733\ \text{MeV} \\ ^3P_1 & M=-1 & 12.7585\ \text{MeV} \\ ^3P_1 & M=\ 0 & 12.7585\ \text{MeV} \\ ^3P_1 & M=+1 & 12.7585\ \text{MeV} \end{pmatrix}$$

Figure 3.2: (Adopted from Refs. [4, 5]) The eigenbasis vector of the target deuteron confined in an external HO trap of strength 5 MeV. This vector makes explicit the basis representation for our model and lists the channel quantum numbers, the angular momentum projection, and the eigenenergies. For the *ab initio* structure calculation, the 3DHO bases are adopted, for which the basis strength is set to be $\omega = 5$ MeV and the truncation parameter $N_{\max}$ to be 60. The lowest-lying 7 states are chosen to construct the basis representation for the target. Note there are the expected degeneracies with respect to the target system's magnetic projection M.

One of the main features of the tBF approach is the ability to incorporate microscopic nuclear structure via the *ab initio* method with an adopted realistic nuclear interaction. For the current work, we adopt the JISP16 [97, 98, 99] realistic NN interaction to construct the target Hamiltonian (Eq. (3.2)). In the 3DHO representation, the eigenenergies and the corresponding eigenstates of the np target are solved according to Eq. (3.10) with both the trap and basis parameters taken to be 5 MeV and $N_{\max} = 60$. For simplicity, we take only three interaction channels for the target, which are ($^3S_1$, $^3D_1$), $^3P_0$ and $^3P_1$. The lowest states of each channel, as shown in Fig. 3.2, are taken into account. In applying the tBF method to this simple demonstration problem, we construct the basis representation for the total time-dependence of the target in terms of these states. The initial

state of the target is taken to be ($^3S_1$, $^3D_1$), $M = -1$, which is polarized against the $\hat{z}$-axis. More interaction channels, different NN interactions and different targets will be studied in the future work.

The interaction between the target and the time-varying external Coulomb field is then expressed as matrix elements in the basis representation. According to the EOM [Eq. (3.4)], the time-dependent state vector of the target can be solved in the form of Eq. (3.11) and Eq. (3.12).

In this work, we investigate selected observables of the target, the transition probability, the r.m.s. charge radius, the r.m.s. intrinsic momentum, the r.m.s. angular momentum, the intrinsic energy and the $\hat{z}$-projection of the total angular momentum, as functions of the exposure time and the incident speed (or, equivalently, bombarding energy). To help formulate our intuition, we also present some details of the evolution of the internal charge distribution (Eq. (3.16)) during the scattering.

3.5 Results and discussions

3.5.1 Transition probabilities

With the total exposure time fixed and only the incident speed altered, we present in Fig. 3.3 the transition probabilities of the basis states of the np target as functions of the time and the incident speed of the HI at intermediate times (from -1 MeV^{-1} to 2 MeV^{-1}), which covers the time period where the significant transitions occur. Note we ignore the corrections from the relativistic effects and the magnetic transitions caused by the induced vector field. For the numerical calculation, we apply the same method introduced in our previous paper [5], where we checked that the tBF method agrees with first-order perturbation theory when the external Coulomb field is sufficiently weak and the first-order effects dominate. In addition, we conduct two more validity checks. First, the normalization of the time-dependent wave function is verified during the evolution of the np target. Second, the time-reversal symmetry of the algorithm for the evolution is verified by explicitly running the solution backwards to the initial state.

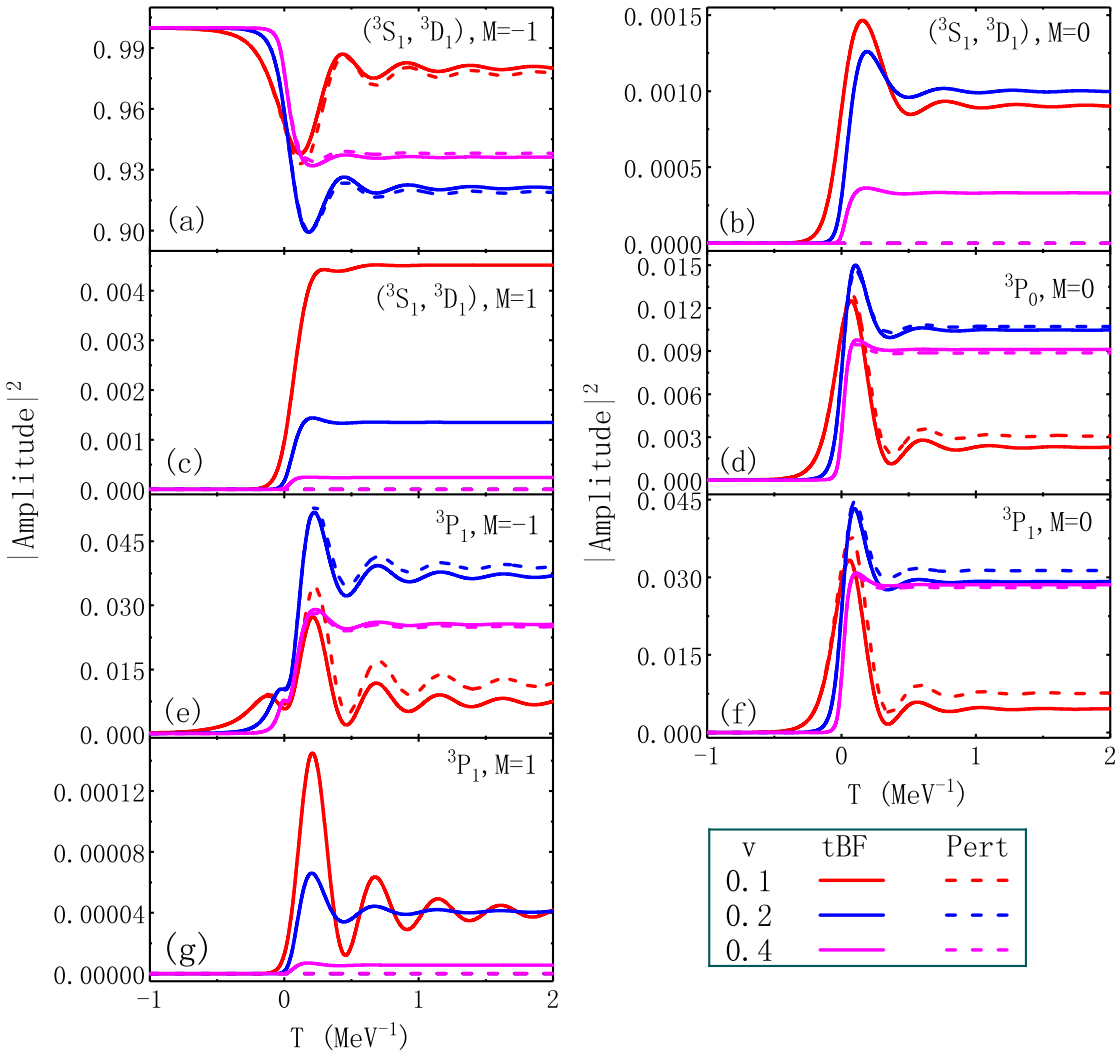

Figure 3.3: (Adopted from Ref. [4]) The Coulomb excitation (only the $E1$ multipole component is included) of the target illustrated as a function of the time and the incident speed of the HI in the middle of the scattering. The target is characterized by 7 basis states. It is initially prepared to be in the state $(^3S_1,\ ^3D_1),\ M = -1$. The HI projectile is taken to be a fully stripped uranium, U^{92+}, and the incident speed is taken as 0.1, 0.2 and 0.4. The transition probabilities of each basis state of the target are calculated via the non-perturbative tBF method and compared with results from first-order perturbation theory (curves labeled by "Pert" in the legend).

3.5.1.1 General features of the excitation

During the scattering, when the HI projectile is sufficiently close to the mass center of the target, abrupt transitions occur and the probabilities exhibit short-time fluctuations. Such quantum fluctuations are expected in the quantal treatment of scattering and we verified that these quantum fluctuations are consistent with the uncertainty relation. We clearly observe such quantum fluctuations in, for example, the evolution of the initial state $(^3S_1,\ ^3D_1),\ M = -1$ with an incident speed $v = 0.4$ in Fig. 3.3. Here, the elastic scattering probability dips sharply and relaxes to its asymptotic value. For this case, the full width half maximum (FWHM) (for the first dip during the evolution) is $\Delta t > 0.1$ MeV^{-1}, while the transition energy is $\Delta E > 12.7$ MeV, yielding a product greater than unity which is consistent with the uncertainty principle.

Eventually, short-time fluctuations attenuate and approach asymptotic values as the Coulomb field fades away. The excited target then evolves into a final superposition of the available eigenstates of the target Hamiltonian. From the produced scattering amplitude at later times, the amplitude for breakup into a particular, kinematically allowed, final state is found by projecting onto that final state. In reality, the excited target can also decay through other kinematically accessible channels, such as through spontaneous EM radiation, which is not included in the present model.

3.5.1.2 Allowed and forbidden transitions

In Fig. 3.3, the difference in the transition probabilities given by the non-perturbative tBF method and the corresponding first-order perturbation theory shows the importance of the higher-order effects during the scattering process. Specifically, since only the $E1$ multipole component of the time-varying Coulomb field is included, we expect the dominant transitions in Fig. 3.3 to reflect the $E1$-selection rule for the calculations based on first-order perturbation theory. We refer to transitions from the initial state that are permitted by first-order perturbation theory as "allowed" and all other transitions as "forbidden" for the purposes of this discussion. However, for the current setup ($Z = 92,\ b = 5$ fm), the Coulomb interaction is strong when the projectile is close to the

target; higher-order effects, which are included by the non-perturbative tBF approach, produce some major consequences when compared with first-order perturbation theory. For example, first-order perturbation theory predicts $(^3S_1,\ ^3D_1),\ M = 1$ to be a "dark" state (an $E1$-forbidden transition), while its population is clearly revealed by the non-perturbative tBF method during the scattering process via a succession of $E1$ transitions through the accessible intermediate states. The tBF population of two additional dark states is shown in Fig. 3.3, which is evident by the contrasting null results from first-order perturbation theory. For the allowed transitions in Fig. 3.3, there are visible differences in the magnitudes between the tBF and the perturbation theory results with first-order perturbation theory tending to overestimate the transition probability for the simulations with the incident speed 0.1 and 0.2.

The time sequence of the transition probabilities is illustrated in Fig. 3.4. The states that obey the $E1$-selection rule from the ground state are populated earlier with more population (e.g., $^3P_1,\ M = -1$), compared to transitions forbidden at leading order. Shortly thereafter, secondary transitions begin to populate the 1^{st}-order forbidden states (e.g., $(^3S_1,\ ^3D_1),\ M = 0$) (these secondary routes are referred to as populating the "1st-order forbidden" states). However, these effects do not significantly populate the forbidden states until the $E1$-allowed states accumulate appreciable population. It is important to note that the de-excitation of states is also included among the transitions. After the 1^{st}-order forbidden states are sufficiently populated, the transition network starts to build up the population for the 2^{nd}-order forbidden states, e.g., $^3P_1,\ M = 1$. In general, the forbidden states populated by the higher-order transitions build up relatively smaller populations.

3.5.1.3 Dependencies of the transitions on the incident speed

With increasing incident speed, we find that the transitions begin later and that the oscillations of the transition probabilities attenuate more rapidly (transitions experience damping of their oscillatory patterns and approach to asymptotic values). These behaviors can be understood based on the strength and time-variation of the Coulomb interaction sensed by the target. According to

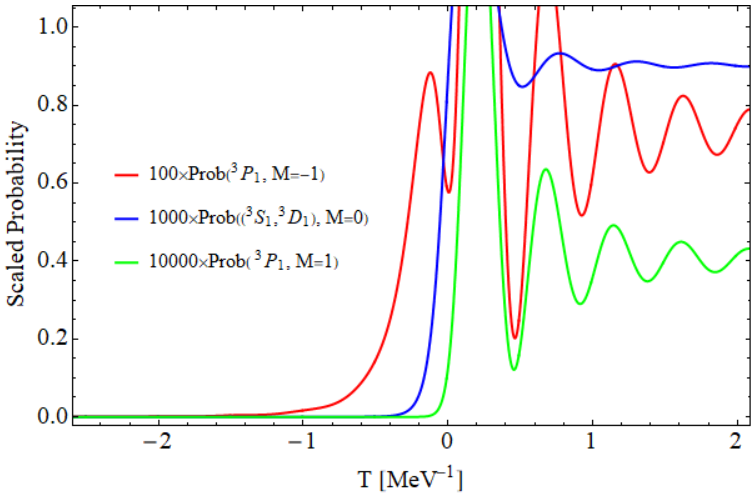

Figure 3.4: (Adopted from Ref. [4]) Illustration of the state populations changing with time during the scattering. Note the transition probabilities are all scaled. The $E1$-allowed state $^3P_1,\ M=-1$ is populated initially. Then one observes the transport of population from the state $^3P_1,\ M=-1$ to the 1^{st}-order forbidden state $(^3S_1,\ ^3D_1),\ M=0$. Later, the transition network populates the 2^{nd}-order forbidden state $^3P_1,\ M=1$ with that population fed from the state $(^3S_1,\ ^3D_1),\ M=0$. The forbidden states also receive population from other states, in which cases relative phases can lead to interference.

Eq. (3.17), the time-variation of the interaction matrix element is, in part, scaled by the geometric factor $\frac{Y^*_{1\mu}(\Omega_R)}{|R(t)|^2}$. Since we set the scattering plane to be the xz-plane, the azimuth angle for $\vec{R}$ vanishes and hence the geometric factor is real. As an example, the values of the geometric factor and its time-variation are shown for the scattering with incident speed $v=0.1$ in Fig. 3.5. We find that significant transitions occur only when the HI projectile is sufficiently close to the target (note the time for approaching differs with the incident speed), where the field strength is strong and the time-variation of the field is rapid. After the HI passes by, the transition probabilities attenuate asymptotically due to the decreasing geometric factor in the interaction matrix elements.

We note that the asymptotic transition probability of each level does not depend on the incident speed monotonically. This is due to the phase factor in Eq. (3.17), which depends on the transition energies. In fact, this phase favors specific transition energies depending on the incident speed. Taking into account the specified transitions included for the current description of the np target (Fig. 3.2), the non-monotonic dependencies of the transition probabilities on the incident speed

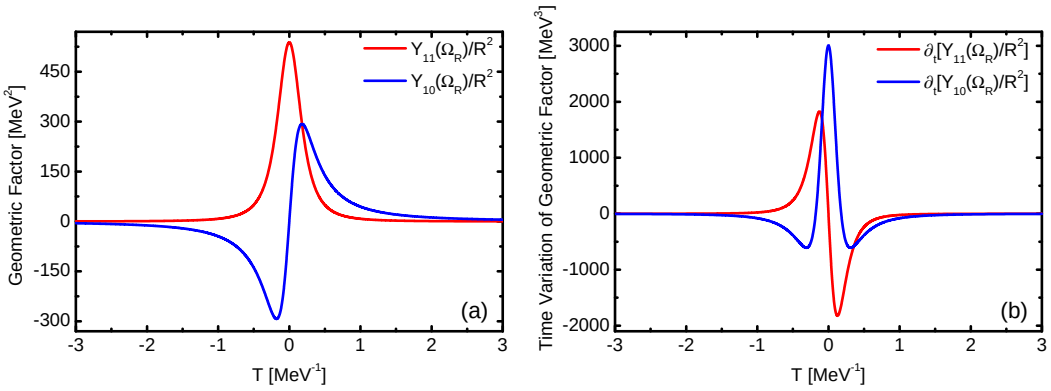

Figure 3.5: (Adopted from Ref. [4]) Illustration of the geometric factor (panel (a)) $\frac{Y^*_{1\mu}(\Omega_R)}{|R(t)|^2}$ ($\mu = \pm 1,\ 0$) and its time-variation (panel (b)) during the scattering. The incident speed is taken as $v = 0.1$. Since the scattering plane is the xz-plane, the azimuth angle vanishes and $Y^*_{1\mu}(\Omega_R)$ is real. The results related to $Y_{1-1}(\Omega_R)$ are omitted owing to the fact that $Y^*_{11}(\Omega_R) = -Y_{1-1}(\Omega_R)$.

can be understood. In other words, the transition probability of each state does not necessarily increase with incident speed. For example, the transition probability to the state $^3P_1, M = -1$ is the largest when the incident speed is $v = 0.2$.

In addition, we find that first-order effects increasingly dominate the final state populations as the incident speed of the HI projectile increases. This could be due to the limitation of the current 7-basis system, where higher-lying scattering states are yet to be included. One expects that higher-lying states receive more population as the incident speed increases. Since our main purpose is to define the approach and demonstrate the method of solution, we defer inclusion of a more complete basis to a future effort.

3.5.2 Observables

With the same simulation conditions as those in Fig. 3.3, we compute the wave functions of the target during the scattering and evaluate a selected set of operators (we refer to them as "observables" for brevity) as functions of the exposure time and the incident speed (Fig. 3.6). We again provide calculations based on first-order perturbation theory to compare with those from the non-perturbative tBF method. Note that the expectation values of the observables do not

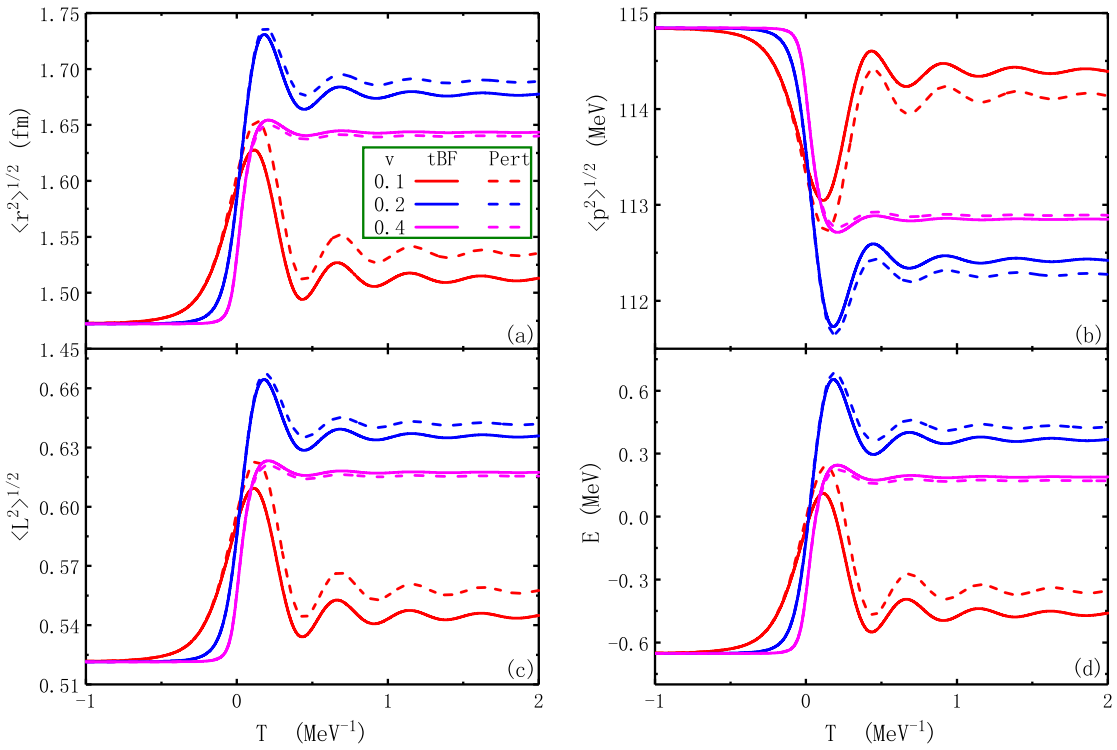

Figure 3.6: (Adopted from Ref. [4]) Selected observables of the *np* target as functions of the exposure time and the incident speed of the HI in the middle of the scattering. Panels (a), (b), (c) and (d) show the evolutions of r.m.s. charge radius, r.m.s. momentum, r.m.s. orbital angular momentum and intrinsic energy, respectively.

change appreciably until the HI gets sufficiently close to the target, while they relax to respective asymptotic values after the HI flies away from the target. We also comment that the initial values of the observables differ from those for a natural deuteron due to the external HO trap introduced in Eq. (3.2). For example, the r.m.s. charge radius of the target before the scattering is 1.472 fm, which is about 25% smaller the experimental measurement 1.975(3) fm for a natural deuteron [100, 101].

All the expectation values of the target observables are evaluated with the time-dependent wave function of the target during the scattering, in which the full quantal coherence is retained. With our limited basis set (Fig. 3.2), the matrix representation of each of our selected operators is diagonal. In other words, the expectation of each observable at a certain moment simplifies here to the calculation of the weighted average (the possible values of the observable weighted by respective

eigenbasis probabilities). Therefore, it is not surprising that the evolutions of different observables behave similarly; the time-dependencies of the observables can be easily understood by the results in Fig. 3.3 and by the fact that higher-lying basis states contribute larger r.m.s. charge radii, eigenenergies and r.m.s. orbital angular momenta together with smaller r.m.s. intrinsic momenta. That is, for each observable as a function of the different incident speeds, the sequence of the onsets of the quantum fluctuations in the middle, the subsidence of the oscillations at the end of the scattering, the importance of the higher-order effects and the dependence on the incident speed are easily interpreted in terms of the behaviors of the transition probabilities (Fig. 3.3). In future applications, with a larger eigenbasis, we anticipate this simple picture will be distorted, for example, by additional coherent effects on the transition matrix elements since the time-dependent amplitude will acquire contributions that are off-diagonal in the eigenbasis.

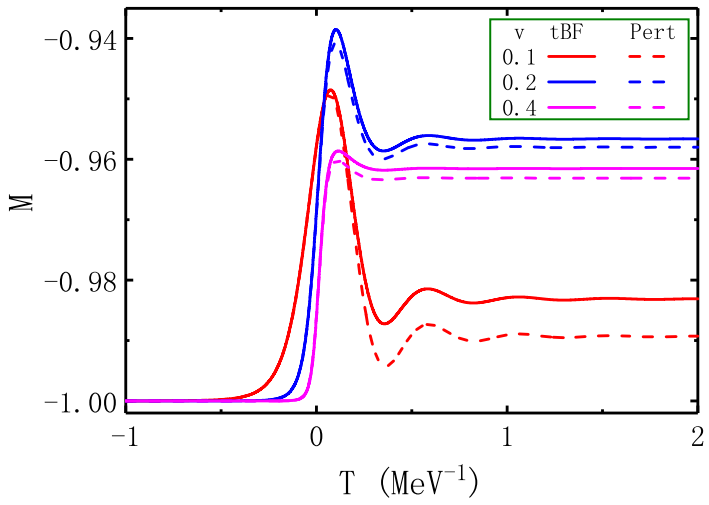

Figure 3.7: (Adopted from Ref. [4]) Expectation values of the $\hat{z}$-projection of the total angular momentum as functions of the exposure time and the incident speed in the middle of the scattering. These values are calculated in the same manner as the observables in Fig. 3.6.

We find that momentum, angular momentum and energy are transferred significantly to the target when the projectile is near its closest approach. The spikes indicating quantum fluctuations with short-time duration subside as the Coulomb field weakens following the HI's closest approach. After the scattering, we find from Fig. 3.6 that the intrinsic motion of the target is excited and that

excitation is greater when the incident speed leads to favorable phase coherence within the current level structure. For example, the average intrinsic energies of the scattered np target (panel (d)) increase by at least 0.7 MeV when the incident speeds are 0.2 and 0.4, indicating the important roles of the excited channels. Even for the case with the incident speed $v = 0.1$, the average intrinsic energy of the scattered target increases by about 10%.

We also note that the $\hat{z}$-projection of the total angular momentum, which determines the polarization of the target, is similarly affected during the scattering process as seen in Fig. 3.7. Indeed, the expectation value of the $\hat{z}$-projection of the total angular momentum indicates the orientation of the target during the scattering.

3.5.3 Evolution of the internal charge distribution

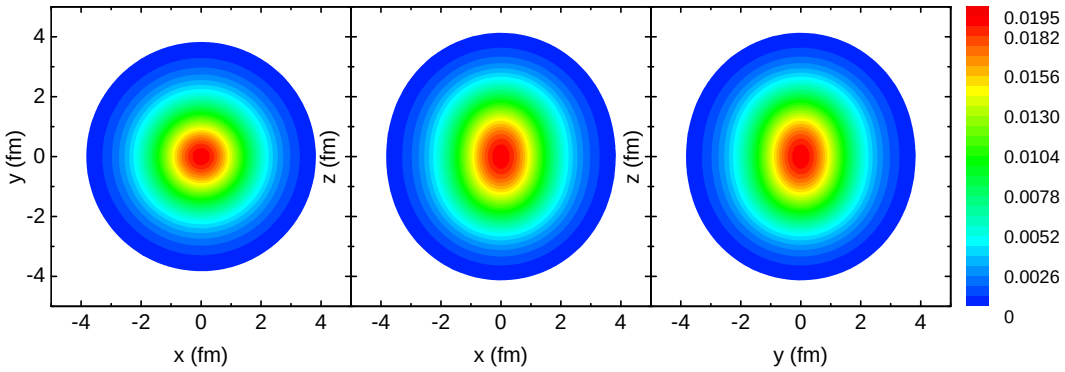

Figure 3.8: (Adopted from Ref. [4]) The internal charge distribution (in fm^{-3}) of the np target before scattering. The initial target is prepared in the state ($^3S_1$, $^3D_1$), $M = -1$, in which the polarization is anti-parallel to the $\hat{z}$-axis. The xz-plane is the scattering plane (see Fig. 3.1), the xy- and yz-planes are respectively perpendicular and parallel to the impinging HI.

The tBF method enables investigations of the detailed dynamics of the scattering process. As an example, we will show in this work the evolution of the internal charge distribution of the target during the scattering process. Since our main purpose here is to set up the methodology, we shall consider only the case with the incident speed $v = 0.1$, where higher-order effects are clearly visible in the complex flow of populations among the levels as discussed above.

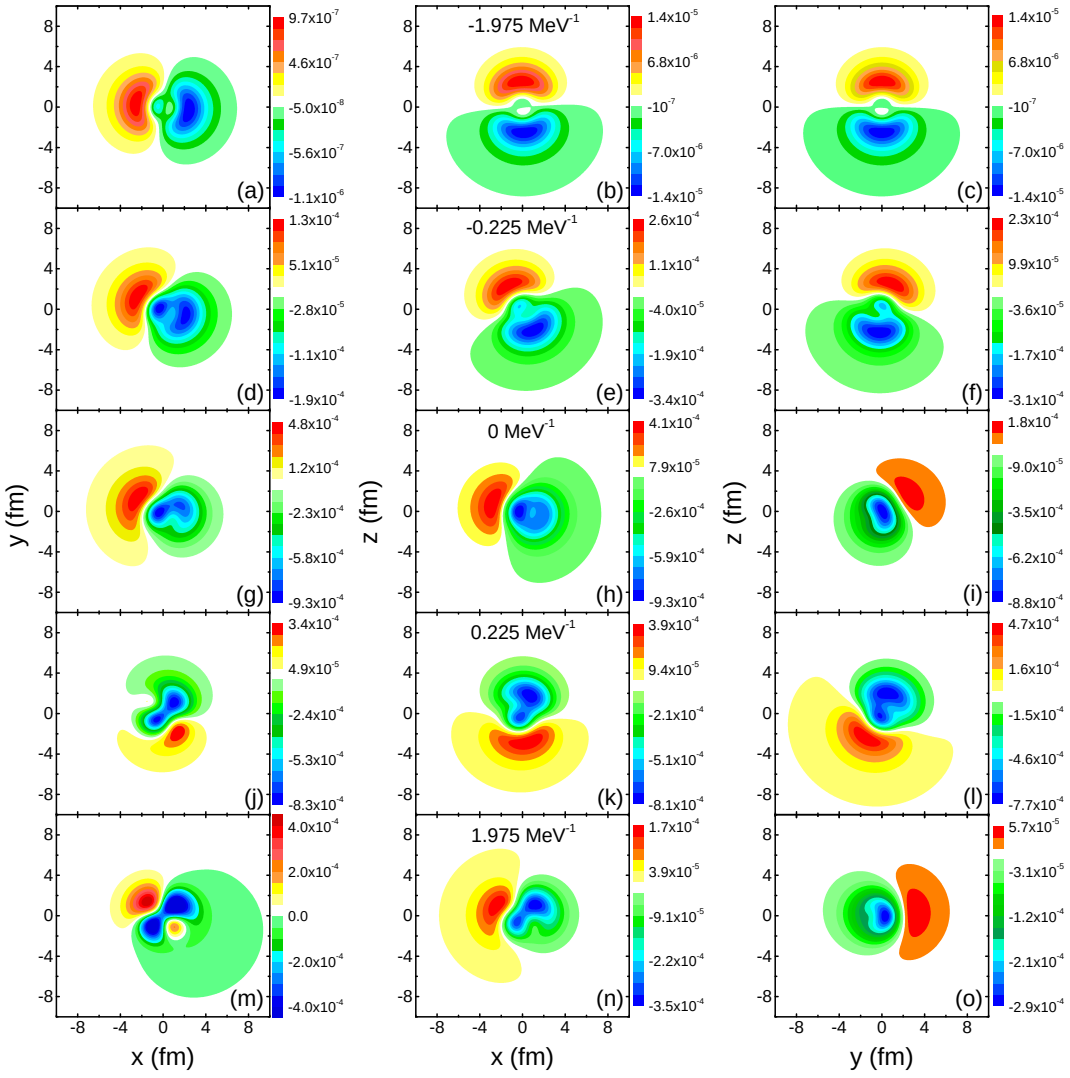

Figure 3.9: (Adopted from Ref. [4]) The overview of the evolution of the internal charge distribution (in fm^{-3}) of the np target during the scattering. The simulation conditions are the same as those in Fig. 3.3, except that the incident speed is chosen as 0.1. These graphs show the difference in the internal charge distributions between the scattered targets at $T = -1.975, -0.255, 0, 0.255, 1.975$ MeV^{-1} and the initial target ($T = -5$ MeV^{-1}) in three orthogonal coordinate planes, where the transition amplitudes of each basis state of the target at the selected moments are calculated via the non-perturbative tBF method. See the text for the details.

In Fig. 3.8, we present the initial internal charge distribution of the target. For the np system under investigation, it is a prolate spheroid with the major axis along the $\hat{z}$-axis. Our distribution differs from the two peaked structure shown in Refs. [102, 103] due to the fact that our wave functions of the np target are solved implementing the JISP16 NN potential, which is a realistic "soft" potential without strong short-range correlations. We present the difference in charge distributions between the initial and the scattered targets (Figs. 3.9, 3.10) to investigate the dynamics at selected intermediate exposure times. We emphasize that this is the information available within our time-dependent treatment. We provide this information to help develop one's intuition, though it is difficult to imagine an experiment that interrogates for this information.

We find, in general, the scattering of the target can be mainly divided into three sequential stages as described in the following.

Stage I: At the very beginning of the scattering, the internal charge distribution of the target begins to polarize due to the repulsive Coulomb interaction, producing a dumbbell shape (the 1^{st} row of Fig. 3.9). Shortly thereafter, more of the positive charge density shifts to the far-side (the side away from the HI) of the target, as would be expected from the effect of the repulsive Coulomb force in a classical picture. The dipole fluctuation of the charge density [104] is also observed together with the general migration of the positive charge density. As the HI approaches, the amplitude of the dipole fluctuation increases. These oscillations are the result of mixing in the excited states with the initial state, however small those mixings may be.

Stage II: As the HI nears the target, the strength of the Coulomb field sensed by the target is stronger and time-variation of the field intensifies. Transitions become stronger (the 2^{nd} row of Fig. 3.9); the modes of different internal motions become more apparent, generating more complex patterns for the charge distributions. The dipole fluctuation of the charge density is suppressed. The migrated positive charge density (forced by the Coulomb repulsion) still concentrates at the far-side of the target.

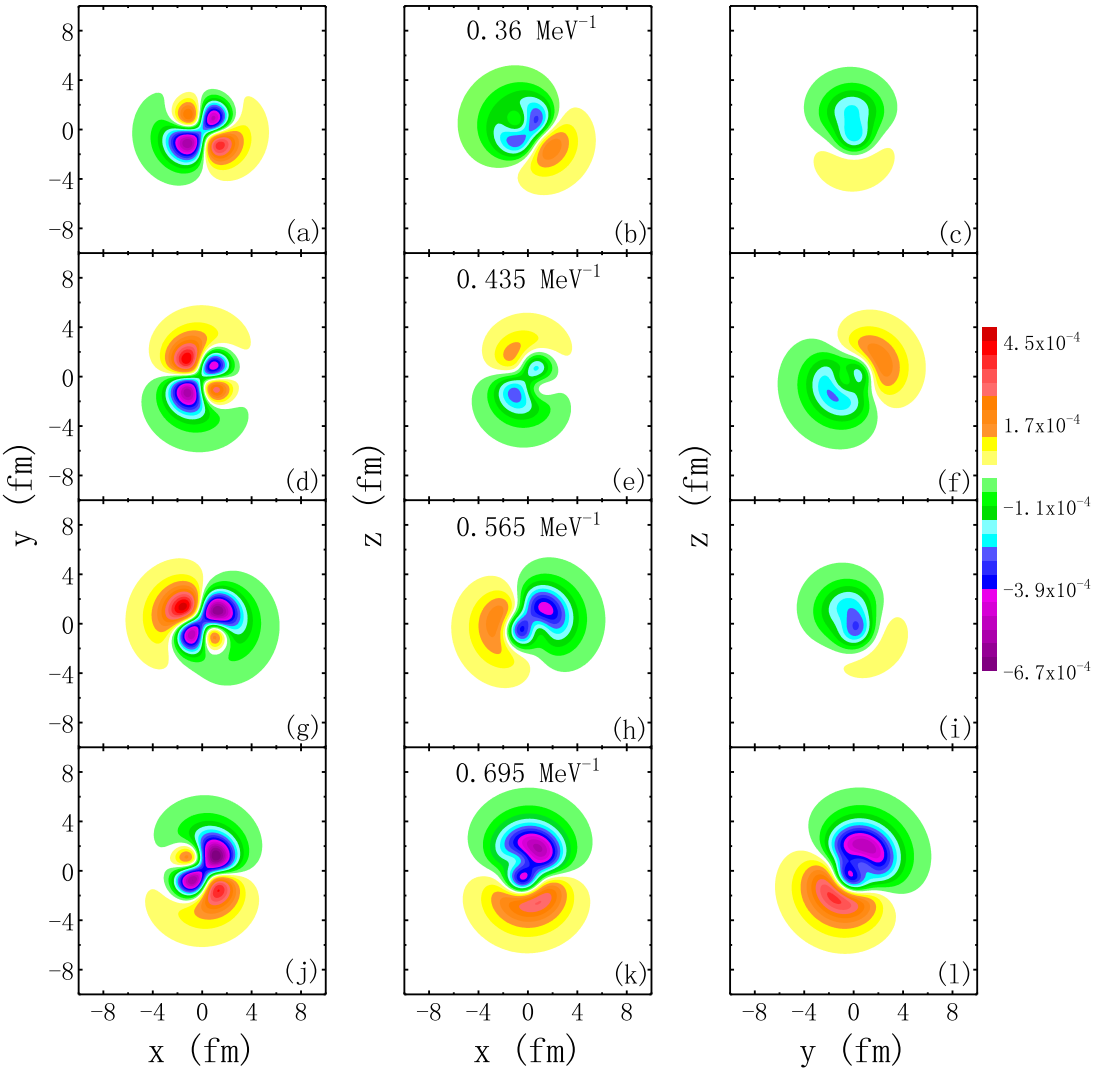

Figure 3.10: (Adopted from Ref. [4]) Stabilization of the target after the scattering. These graphs show the difference in the internal charge distributions (in fm^{-3}) between the initial target ($T = -5$ MeV^{-1}) and the scattered targets at $T = 0.36$ MeV^{-1} (top row), 0.435 MeV^{-1} (2$^{\rm nd}$ row), 0.565 MeV^{-1} (3$^{\rm rd}$ row), 0.695 MeV^{-1} (bottom row). The other simulation conditions are the same with Fig. 3.9 and the transition amplitudes of each basis state are calculated via the tBF method. See the text for the details.

Right after the HI passes its closest approach to the np system, different coordinate planes show the rotational motion of the np target (indicated by the 3$^{\rm rd}$ and 4$^{\rm th}$ rows of Fig. 3.9). The directions are counter-clockwise in the xy- and xz-planes and clockwise in the yz-plane. These rotational directions are determined by the preparation of the initial target. For example, if we had prepared $(^3S_1,\ ^3D_1),\ M = 1$ as the initial state for the target, the direction of the rotation would switch (e.g., the rotation would become clockwise in the xy-plane). We verified this by actual simulation. In addition to the rotational motion, fluctuations with complex modes in the charge density occur, as clearly shown in the 4$^{\rm th}$ row of Fig. 3.9.

Stage III: When the HI moves further away, the Coulomb field weakens and its time-variation decreases, reducing the amount of energy, momentum and angular momentum transferred to the target per unit time. The target begins to stabilize. The snapshots for the stabilization process are shown in Fig. 3.10. Note that we present the sequence of graphs such that the internal charge distribution rotates evenly in the xy-plane, as can be easily seen from the steady increase in the azimuth angle of the "green cloud" in the leftmost column.

After stabilization (the 5$^{\rm th}$ row of Fig. 3.9), the scattered target evolves as a superposition of the basis states according to the 'unperturbed' Hamiltonian H_0. The time evolution of the internal charge distribution of the target shown in Fig. 3.10 repeats, indicating the final state is reached. We find the range of the internal charge distribution of the scattered target expands compared to the initial distribution shown in Fig. 3.8. This is signified by the expansion of the r.m.s. charge radius as shown in the panel (a) of Fig. 3.6. In addition, the complex patterns in the internal charge distribution indicate the excitation of the orbital angular momentum (panel (c) in Fig. 3.6). Finally, we observe the combination of the rotation and oscillations in the charge density, again indicating the excitation of these degrees of freedom.

CHAPTER 4. CHIRAL NUCLEON-PION MODEL VIA BASIS LIGHT-FRONT QUANTIZATION

4.1 Introduction

Developing a relativistic methodology that is broadly applicable to nuclear physics is important for studying high-momentum transfer experiments on nuclear targets in exclusive, nearly exclusive or inclusive processes [105, 106, 107]. One of the promising methods for such investigations is the Basis Light-Front Quantization (BLFQ) approach [84].

BLFQ is a non-perturbative, *ab initio* method, which treats relativistic quantum field theory via the Hamiltonian approach within the light-front (LF) formalism. BLFQ has been shown to be a promising tool in a range of applications, such as the electron anomalous magnetic moment [108, 109], the positronium spectrum [110], and the heavy quarkonium structure and radiative transitions [111, 112, 113, 114, 115]. More recently, BLFQ has been applied successfully to the properties of the light mesons [116], which are then extended to higher scales by QCD evolution [117]. This Hamiltonian approach has also been extended to develop a non-perturbative scattering framework through time-dependent BLFQ (tBLFQ) [85, 118].

BLFQ employs the LF formalism [119, 120], where physical systems are quantized at fixed LF time $x^+ = t + z$ [121]. The structure and dynamics of the systems are characterized by the Hamiltonian formalism. The LF vacuum has a simple structure since the Fock vacuum is an exact eigensate of the full normal-ordered Hamiltonian [122, 123]. This provides access to the Fock-space expansion of the physical states in the LF field theory and thereby generates physical intuition for their underlying structures [122, 123].

BLFQ also takes the advantage of the developments in *ab initio* non-relativistic quantum many-body theories, such as the No-Core Shell Model (NCSM) [19, 20, 9], and the rapidly developing supercomputing techniques (algorithm and hardware) (see, e.g., [3] and references therein). In

BLFQ, the LF mass-squared operator of a hadron system in the basis representation becomes a sparse matrix whose dimensions are controlled by truncations that respect the relativistic symmetries. By matrix diagonalization, the eigenvalues produce the mass sprectum, while the resulting eigenfunctions are the light-front wave functions (LFWFs) that encode the hadronic properties. The LFWFs can be boosted to a general Lorentz frame for calculating, e.g., form factors and scattering processes [122].

The LF quantization approach to treat a chiral model of the nucleon-pion ($N\pi$) system was first proposed by Miller [124, 125] in studying the $N\pi$ scattering and the nucleon-nucleon scattering via perturbation theory. In this work, we will present the first non-perturbative, *ab initio* treatment of the same chiral model via the BLFQ method. In particular, we consider a physical proton as the relativistic bound state of the $N\pi$ system. Using the BLFQ approach, we obtain the LF mass-squared matrix of the $N\pi$ system within a truncated basis. We then compute the proton's mass and the corresponding LFWF by numerical diagonalization of the mass-squared matrix. We evaluate the proton's parton distribution function (PDF) and Dirac form factor based on the LFWF. In this work, we also implement an improved model to calculate the proton's Dirac form factor.

This chapter is based on Refs. [6, 7] and is organized in the following way. We begin by introducing our adopted Lagrangian density in Sec. 4.2. Then, in Sec. 4.3, we introduce the elements of BLFQ, such as the derivation of the LF Hamiltonian density, our choice of the basis construction and truncation schemes, the derivation of the mass-squared matrix element in the basis representation, and the formalism for obtaining additional observables in this work. We present the results in Sec. 4.4 for the proton's mass, the calculations of the proton's LFWF, PDF and the Dirac form factor.

4.2 Theory I: Lagrangian density of the chiral model

We begin with the nucleon-pion ($N\pi$) Lagrangian density (c.f., Eqs. (2.1) and (2.2) in Refs. [124, 125])

$$\mathcal{L}'_{\rm total} = \frac{1}{4}\Big(\frac{F}{g_A}\Big)^2 {\rm Tr}\Big(\partial_\mu U \partial^\mu U^\dagger\Big) + \frac{1}{4}M_\pi^2\Big(\frac{F}{g_A}\Big)^2 {\rm Tr}\Big(U + U^\dagger - 2\Big) + \mathcal{L}'_{N\pi} \ , \tag{4.1}$$

where $\mathcal{L}'_{N\pi}$ denotes the non-linear representation of the $N\pi$-interaction:

$$\mathcal{L}'_{N\pi} = \bar{N}\Bigg\{\gamma_\mu i\partial^\mu - M_N - \frac{1}{1+(\pi)^2\big(\frac{g_A}{2F}\big)^2}\Big[\frac{g_A}{2F}\gamma_\mu\gamma_5\vec{\tau}\cdot\partial^\mu\vec{\pi} + \frac{1}{4F^2}\gamma_\mu\vec{\tau}\cdot\vec{\pi}\times\partial^\mu\vec{\pi}\Big]\Bigg\}N \ . \tag{4.2}$$

N denotes the nucleon field operator. We set $F \equiv g_A \cdot f_\pi$ with $g_A = 1.25$ representing the tree-level axial-vector coupling constant and f_π representing the pion decay constant (set as 93 MeV in this work). M_π denotes the pion mass (taken to be 137 MeV in this work). The unitary operator U corresponds to the definition of the pion field (more details are available in Refs. [126, 124, 125]). In this work, we choose U as

$$U = (U^{-1})^\dagger = \frac{1 + i\gamma_5\vec{\tau}\cdot\vec{\pi}\frac{g_A}{2F}}{1 - i\gamma_5\vec{\tau}\cdot\vec{\pi}\frac{g_A}{2F}} \ = \ 1 + i\gamma_5\frac{g_A}{F}\vec{\tau}\cdot\vec{\pi} + \mathcal{O}\Big(\frac{g_A^2}{F^2}\Big), \tag{4.3}$$

where $\vec{\tau}$ denotes the Pauli matrices τ_a ($a = 1, 2, 3$), while $\vec{\pi}$ represents the pion fields π_a ($a = 1, 2, 3$).

In order to treat the chiral model [Eqs. (4.1) and (4.2)] via the LF Hamiltonian formalism, we first manipulate the factor $\frac{1}{4F^2}$ and obtain

$$\begin{aligned}\mathcal{L}'_{N\pi} =& \bar{N}\Bigg\{\gamma_\mu i\partial^\mu - M - \frac{1}{1+(\pi)^2\big(\frac{g_A}{2F}\big)^2}\Big[\frac{g_A}{2F}\gamma_\mu\gamma_5\vec{\tau}\cdot\partial^\mu\vec{\pi} + \Big(\frac{g_A}{2F}\Big)^2\gamma_\mu\vec{\tau}\cdot\vec{\pi}\times\partial^\mu\vec{\pi}\Big]\Bigg\}N \\ &+ \bar{N}\Bigg\{\frac{1}{1+(\pi)^2\big(\frac{g_A}{2F}\big)^2}\Big[\frac{g_A^2-1}{4F^2}\gamma_\mu\vec{\tau}\cdot\vec{\pi}\times\partial^\mu\vec{\pi}\Big]\Bigg\}N \ .\end{aligned} \tag{4.4}$$

We then transform/redefine the nucleon field (c.f., Refs. [124, 125]) as

$$N = U^{-\frac{1}{2}}\chi \ , \tag{4.5}$$

where χ denotes the transformed nucleon field. The unitary operator $U^{-\frac{1}{2}}$ is

$$U^{-\frac{1}{2}} = \Big(U^{\frac{1}{2}}\Big)^\dagger = \frac{1 - i\gamma_5\vec{\tau}\cdot\vec{\pi}\frac{g_A}{2F}}{\sqrt{1+(\pi)^2\big(\frac{g_A}{2F}\big)^2}} \ . \tag{4.6}$$

The following identities hold

$$U^{\pm\frac{1}{2}}\gamma_\mu = \gamma_\mu U^{\mp\frac{1}{2}} \ , \tag{4.7}$$

$$i\partial^\mu U^{-\frac{1}{2}} = R^\mu U^{-\frac{1}{2}} \ . \tag{4.8}$$

where we define

$$R^\mu \equiv \frac{1}{1+\left(\pi\right)^2\left(\frac{g_A}{2F}\right)^2}\left[\frac{g_A}{2F}\gamma_5\vec{\tau}\cdot\partial^\mu\vec{\pi} + \left(\frac{g_A}{2F}\right)^2\vec{\tau}\cdot\vec{\pi}\times\partial^\mu\vec{\pi}\right] \ . \tag{4.9}$$

Applying the transformation Eq. (4.5) and the identities Eqs. (4.7) and (4.8) to Eq. (4.4), we obtain the transformed $N\pi$ interaction Lagrangian density as

$$\mathcal{L}_{N\pi} = \bar{\chi}\Big[\gamma_\mu i\partial^\mu - M_N U^\dagger\Big]\chi + \frac{g_A^2-1}{4F^2}\bar{\chi}\left\{\frac{1}{1+\left(\pi\right)^2\left(\frac{g_A}{2F}\right)^2}\Big[\gamma_\mu\vec{\tau}\cdot\vec{\pi}\times\partial^\mu\vec{\pi}\Big]\right\}\chi \ . \tag{4.10}$$

Note that the first term of Eq. (4.10) is of the linear representation of the chiral symmetry used by Gürsey [126] and Miller [124, 125], while the second nonlinear term is proportional to the Weinberg-Tomozawa [127, 128] contact term.

Overall, we obtain the transformed total $N\pi$ Lagrangian density (c.f., Eqs. (2.1) and (2.2) in Ref. [124]) as

$$\mathcal{L}_{\rm total} = \frac{1}{4}\left(\frac{F}{g_A}\right)^2{\rm Tr}\Big(\partial_\mu U\partial^\mu U^\dagger\Big) + \frac{1}{4}M_\pi^2\left(\frac{F}{g_A}\right)^2{\rm Tr}\Big(U+U^\dagger-2\Big) + \mathcal{L}_{N\pi} \ , \tag{4.11}$$

where $\mathcal{L}_{N\pi}$ is shown in Eq. (4.10). Note that $\mathcal{L}'_{\rm total}$ [Eq. (4.1)] and (after the chiral transformation Eq. (4.5)) $\mathcal{L}_{\rm total}$ are approximately invariant ($M_\pi \neq 0$) under the chiral transformation [124, 125]

$$N \to {\rm e}^{i\gamma_5\vec{\tau}\cdot\vec{a}}\ N \ (\text{or } \chi \to \ {\rm e}^{i\gamma_5\vec{\tau}\cdot\vec{a}}\chi) \ , \tag{4.12}$$

$$U \to {\rm e}^{-i\gamma_5\vec{\tau}\cdot\vec{a}}\ U\ {\rm e}^{-i\gamma_5\vec{\tau}\cdot\vec{a}} \ . \tag{4.13}$$

If one works up to the terms with the one-pion processes (or, up to the order of g_A/F), Eq. (4.11) takes the following form:

$$\mathcal{L}_{\rm total} = \frac{1}{2}\partial_\mu\vec{\pi}\cdot\partial^\mu\vec{\pi} - \frac{1}{2}M_\pi^2\vec{\pi}\cdot\vec{\pi} + \bar{\chi}\Big[\gamma_\mu i\partial^\mu - M_N\Big(1 - i\frac{g_A}{F}\gamma_5\vec{\tau}\cdot\vec{\pi}\Big)\Big]\chi + \mathcal{O}\Big(\frac{g_A^2}{F^2}\Big) \ . \tag{4.14}$$

4.3 Theory II: BLFQ approach to the chiral model

In this section, we demonstrate the idea/methodology of treating the chiral Lagrangian [Eqs. (4.1) and (4.2)] via the non-perturbative BLFQ approach. We begin by obtaining the Hamiltonian density and follow with details about solving for the mass spectra and LFWFs. We also present the method for calculating selected observables. The interested reader is referred to our paper [7], which is to be submitted for publication soon.

4.3.1 Hamiltonian dynamics

The dynamical $N\pi$ system can be evaluated from the eigenvalue equation

$$P^\mu P_\mu |\Psi\rangle \quad = \quad M^2 |\Psi\rangle \ , \tag{4.15}$$

where P^μ is the four-vector operator of the energy-momentum. In the LF coordinates, the mass-squared operator,

$$H_{LC} \equiv P^2 = P^\mu P_\mu = P^+ P^- - (P^\perp)^2 \ , \tag{4.16}$$

is analogous to the Hamiltonian in non-relativistic quantum mechanics. The details of the LF conventions and notations in this work can be found in Appendix C. Since P^+ and $(P^\perp)^2$ are kinematical, the P^-,

$$P^- = \frac{(P^\perp)^2 + M^2}{P^+} \ , \tag{4.17}$$

is also referred to as LF Hamiltonian that generates the LF time-evolution (dynamics). P^- is obtained from the Lagrangian via a Legendre transformation.

H_{LC} can be numerically evaluated in a chosen set of basis states as in BLFQ. In principle, the set of basis states has infinite dimension. In practice, one limits the basis size by introducing truncation scheme(s). The resulting finite-dimensional eigenvalue problem can be evaluated numerically as a function of cutoff(s) in the truncation scheme(s). By extrapolation to the continuum limit, the physical observables can be obtained. Alternatively, as is frequently the case in an effective field

theory, one selects a truncation to match a limiting scale in the theory. For example, we can view the present effort as the application of an effective field theory valid on a scale below the scale where quark and gluon dynamics are essential.

4.3.2 LF Hamiltonian density by Legendre transformation

Applying the standard Legendre transformation (see, e.g., Refs. [85, 124]) to the Lagrangian density Eq. (4.14), we obtain the LF Hamiltonian density as

$$\begin{aligned}\mathcal{P}^- = &\underbrace{\frac{1}{2}\partial^\perp\pi_a\cdot\partial^\perp\pi_a + \frac{1}{2}M_\pi^2\pi_a\pi_a + \chi_+^\dagger\frac{(p^\perp)^2+M_N^2}{p^+}\chi_+}_{\text{kinetic energy for free pion and nucleon}}\\ &+\underbrace{\chi_+^\dagger\Big[-\gamma^\perp\cdot i\partial^\perp + M_N\Big]\frac{1}{p^+}M_N\Big[-i\gamma_5\frac{g_A}{F}\vec{\tau}\cdot\vec{\pi}\Big]\chi_+ + \chi_+^\dagger M_N\Big[+i\gamma_5\frac{g_A}{F}\vec{\tau}\cdot\vec{\pi}\Big]\frac{1}{p^+}\Big[\gamma^\perp\cdot i\partial^\perp + M_N\Big]\chi_+}_{\text{one-pion emission and absorption}}\\ &+\mathcal{O}(g_A^2/F^2)\ ,\end{aligned} \tag{4.18}$$

where χ_+ is the dynamical component of the nucleon field. It is related to the kinematic component of the nucleon field, χ_-, by the constraint equation:

$$\chi_- = \frac{1}{p^+}\gamma^0\Big[\gamma^\perp\cdot p^\perp + M_N\Big(1-i\gamma_5\frac{g_A}{F}\vec{\tau}\cdot\vec{\pi}\Big)\Big]\chi_+\ . \tag{4.19}$$

Note that in this prototype work that mainly focuses on demonstrating the features of the BLFQ framework for this dynamical system, we retain only the terms up to the order of g_A/F as for the interaction terms, which correspond to the processes of single-pion emission/absorption. Higher-order terms, such as the π^2 terms and the instantaneous fermion propagation terms (c.f., Refs. [124, 125]), are expected to be the corrections to the current calculation and will be the topic of a future work.

4.3.3 Basis representation: construction and truncation schemes

4.3.3.1 Symmetries

The BLFQ methodology of constructing the basis for carrying out the matrix eigenvalue solution of the LF mass-squared operator $H_{\rm LC}$ is discussed in Refs. [84, 85, 110]. In particular, we need to

pay specific attention to the symmetries of the LF Hamiltonian P^-. These symmetries are: (1) the translational symmetry in the longitudinal direction, which results in the conservation of the total longitudinal momentum P^+; (2) the rotational symmetry in the transverse direction, which means that the projection of the total angular momentum is conserved; (3) the conservation of net fermion number; and (4) transverse boost invariance. In this work, we also assume rotational symmetry in isospin space, where the projection of the isospin of the constituent system is conserved. We construct the LF basis set according to these symmetries.

4.3.3.2 Single-particle basis

We start with constructing the single-particle (s.p.) basis. In the longitudinal direction, we employ the discretized plane wave basis $\{|p^+\rangle\}$. In particular, we constrain a particle in a longitudinal box of length $x_+ = L$ and apply the periodic (anti-periodic) boundary condition to the boson (fermion). The longitudinal momentum is discretized as

$$p^+ = \frac{2\pi}{L} j \ , \tag{4.20}$$

with $j = 1, 2, 3, \cdots$ for the boson and $j = \frac{1}{2}, \frac{3}{2}, \frac{5}{2}, \cdots$ for the fermion. Note that we exclude the "zero modes" ($j = 0$) for the bosons (pions in this work).

It is useful to define the longitudinal momentum fraction x in terms of the total longitudinal momentum P^+ as the Bjorken variable

$$x \equiv \frac{p^+}{P^+} \ = \ \frac{j}{K} \ , \tag{4.21}$$

where the dimensionless parameter K is related to P^+ via the relation $P^+ = \frac{2\pi}{L} K$.

In the transverse direction, we employ the two dimensional harmonic oscillator (2DHO) basis. As explained in the Appendix D, the 2DHO basis in the momentum representation can be labeled by the radial number n and the angular quantum number m. Adopting the 2DHO basis in the transverse direction provides us with means to insure the transverse boost invariance of the LF kinematics [84, 122] as discussed further in Sec. 4.3.5 below.

In addition to the momentum space, we also have the the spin and isospin degrees of freedom for the $N\pi$ model. The s.p. basis can thus be classified according to the following set of quantum numbers

$$|\alpha\rangle = |x, n, m, s, t\rangle \ , \tag{4.22}$$

where s denotes the helicity and t denotes the projection of the isospin of the particle. It is understood that the nucleons are of spin $\frac{1}{2}$ and isospin $\frac{1}{2}$, while pions are of spin 0 and isospin 1. The orthonormality relation of the s.p. basis is

$$\langle x, n, m, s, t|x', n', m', s', t'\rangle = \delta_{x,x'}\delta_{n,n'}\delta_{m,m'}\delta_{s,s'}\delta_{t,t'} \ . \tag{4.23}$$

4.3.3.3 Multi-particle basis

The multi-particle basis is constructed as a direct product of the s.p. bases ($\otimes|\alpha\rangle$). According to the symmetries of P^- for the $N\pi$ system, we require the quantum numbers for all the constituent particles (labeled by i) in the retained multi-particle basis states to satisfy the following relations

$$\sum_i p_i^+ = P^+, \ \sum_i m_i + \sum_i s_i = M_J, \ \sum_i t_i = T_z, \ \sum_i n_f^i = N_f \ . \tag{4.24}$$

The first identity requires all the basis states to have the same total longitudinal momentum. It is equivalent to

$$\sum_i j_i = K \text{ or } \sum_i x_i = 1 \ , \tag{4.25}$$

according to Eqs. (4.20) and (4.21) for the fixed box-length L and the total longitudinal momentum P^+. The second identity in Eq. (4.24) states the conservation of the projection of the total angular momentum M_J, which is produced by the helicity s and the projection of the orbital angular momentum m of each constituent particle. (Note, however, the total angular momentum J is not a good quantum number in the LF basis states.) The third identity in Eq. (4.24) states that the projection of the total isospin T_z or, equivalently, total charge of the system is conserved. The last identity in Eq. (4.24) refers to the conservation of the net fermion number N_f, where $n_f^i = 1$ for a nucleon and $n_f^i = 0$ for each pion.

4.3.3.4 Truncation scheme

We apply three truncations in this work. First, the number of Fock sectors for the $N\pi$ system is truncated at the nucleon plus one-pion sector

$$|N_{\rm phys}\rangle \quad = \quad a|N\rangle + b|N\pi\rangle \ , \tag{4.26}$$

with the amplitudes $a = \langle N|N_{\rm phys}\rangle$ and $b = \langle N\pi|N_{\rm phys}\rangle$. It is also possible to include higher Fock sectors, e.g., $|N\pi\pi\rangle$. However, we would postpone this to future work. According to the Fock sector truncation Eq. (4.26), we have the net fermion number $N_f = 1$ for all the basis states.

According to the Fock sector truncation Eq. (4.26), the LF basis set in this work is

$$\{|\xi\rangle\} = \{|\xi_N\rangle\} \oplus \{|\xi_{N\pi}\rangle\} \ . \tag{4.27}$$

For the $|N\rangle$ sector, the LF basis set is

$$\{|\xi_N\rangle\} = \{|x_N, n_N, m_N, s_N, t_N\rangle\} \ , \tag{4.28}$$

with $x_N = 1$ due to the conservation of the longitudinal momentum. For the $|N\pi\rangle$ sector, the LF basis set is

$$\{|\xi_{N\pi}\rangle\} = \{|x_N, n_N, m_N, s_N, t_N; x_\pi, n_\pi, m_\pi, \lambda\rangle\} \ , \tag{4.29}$$

where λ denotes the isospin projection of the pion field. The null spin projection of the pion field ($s_\pi = 0$) is omitted. Note that $x_\pi \neq 0$ since we exclude the zero mode of the pion field in the longitudinal direction. Due to the conservation of the total longitudinal momentum, we also have $x_N + x_\pi = 1$ and $0 < x_N < 1$ for the $|N\pi\rangle$ sector.

Second, we cut off the total longitudinal momentum for the many-body basis state

$$K = K_{\rm max}, \tag{4.30}$$

which makes the number of the longitudinal modes finite [129]. The longitudinal continuum limit can be approached at the limit of $K_{\rm max} \to \infty$ for a given box length L.

Third, we truncate the number of the modes in the transverse direction for the many-body basis states by restricting the number of maximal excitation quanta, $N_{\max}$, as

$$\sum_i (2n_i + |m_i| + 1) \leq N_{\max}, \tag{4.31}$$

where i denotes the constituent particles. By taking $N_{\max} \to \infty$, the continuum limit in the transverse direction is realized.

4.3.3.5 UV and IR cutoffs

The 2DHO basis parameters are related, intrinsically, to the ultravilot (UV) and infrared (IR) cutoffs of the model space [130, 131]. In the momentum space, the UV and IR cutoffs can be, respectively, approximated by the basis truncation parameter $N_{\max}$ and the basis strength b as

$$p^{\perp}_{\max} \approx b\sqrt{2N_{\max}}\,, \tag{4.32}$$

$$p^{\perp}_{\min} \approx b/\sqrt{2N_{\max}}\,. \tag{4.33}$$

4.3.3.6 Factorization

The application of the 2DHO s.p. basis in the transverse direction with $N_{\max}$ truncation admits an exact factorization of the LFWF into "intrinsic" and COM components [110, 132, 9]. Taking advantage of this factorization, the spurious COM excitation due to the adoption of the 2DHO s.p. basis can be eliminated by the use of a Lagrange multiplier term as explained below. The analogous factorization scheme has been adopted in the studies of nuclear structures (c.f., Refs. [132, 9]), where the three dimensional harmonic oscillator basis is adopted.

4.3.4 Mode expansions

The pion field can be expressed in terms of the creation and annihilation operators (c.f., Refs. [85, 110])

$$\pi_a(x) = \sum_{k^+} \sum_{\lambda=-1}^{\lambda=1} \frac{1}{\sqrt{2Lk^+}} \int \frac{d^2k^{\perp}}{(2\pi)^2} \Big[a(k,\lambda)\varepsilon_a(\lambda) e^{-ikx} + a^{\dagger}(k,\lambda)\varepsilon_a{}^*(\lambda) e^{ikx} \Big]\,, \tag{4.34}$$

where we make it explicit that we are discretizing the longitudinal momenta and we introduce the following polarization vectors for the isospin degree of freedom of the pion field π_a $(a = 1, 2, 3)$

$$\varepsilon(+1) = \frac{1}{\sqrt{2}}(1, i, 0)^T,\ \varepsilon(0) = (0, 0, 1)^T,\ \varepsilon(-1) = \frac{1}{\sqrt{2}}(1, -i, 0)^T\ , \tag{4.35}$$

with $\varepsilon^\dagger(\lambda_i)\varepsilon(\lambda_j) = \delta_{\lambda_i,\lambda_j}$ and $\varepsilon(-\lambda) = \varepsilon^*(\lambda)$. The subscript "a" also indicates the component of the polarization vector $\varepsilon(\lambda)$. λ denotes the projection of the isospin of the physical pions, i.e., $\pi^\pm$ and π^0.

Similar to the pion field, the nucleon field can be represented with the creation and annihilation operators (c.f., Refs. [85, 110])

$$\chi_+(x) = \sum_{p^+}\sum_{s,t}\frac{1}{\sqrt{2L}}\zeta(s)T(t)\int\frac{d^2p^\perp}{(2\pi)^2}\left[b(p,s,t)e^{-ipx} + d^\dagger(p,-s,-t)e^{ipx}\right]\ , \tag{4.36}$$

where

$$\zeta(+\frac{1}{2}) = (1,0,0,0)^T,\ \zeta(-\frac{1}{2}) = (0,1,0,0)^T\ , \tag{4.37}$$

$$T(+\frac{1}{2}) = (1,0)^T,\ T(-\frac{1}{2}) = (0,1)^T\ . \tag{4.38}$$

With the discretized longitudinal momentum [Eq. (4.21)], the commutation and anticommutation relations are

$$[a(k,\lambda), a^\dagger(k',\lambda')] = (2\pi)^2\delta^{(2)}(k_\perp - k'_\perp)\delta_{\lambda,\lambda'}\delta_{x,x'}\ , \tag{4.39}$$

$$\{b(p,s,t), b^\dagger(p',s',t')\} = (2\pi)^2\delta^{(2)}(p_\perp - p'_\perp)\delta_{s,s'}\delta_{t,t'}\delta_{x,x'}\ , \tag{4.40}$$

$$\{d(p,s,t), d^\dagger(p',s',t')\} = (2\pi)^2\delta^{(2)}(p_\perp - p'_\perp)\delta_{s,s'}\delta_{t,t'}\delta_{x,x'}\ . \tag{4.41}$$

Note that with our limited Fock space [Eq. (4.26)], the independent field for the anti-nucleon is not included. The canonical anti/commutation relations are

$$[\pi_a(x), \pi_b(y)]_{x^+=y^+} = -\frac{i}{4}\epsilon(x^- - y^-)\delta^{(2)}(x^\perp - y^\perp)\delta_{ab}\ , \tag{4.42}$$

$$\{\chi_+(x), \chi_+^\dagger(y)\}_{x^+=y^+} = \frac{1}{2}\gamma^0\gamma^+\delta(x^- - y^-)\delta^{(2)}(x^\perp - y^\perp)\ . \tag{4.43}$$

$\epsilon(x) = \theta(x) - \theta(-x)$ is the antisymmetric step function, where the step function is

$$\theta(x) = 0 \quad \text{for } x \le 0\ ;\ \theta(x) = 1 \quad \text{for } x > 0\ . \tag{4.44}$$

The relations $\frac{\partial\epsilon(x)}{\partial x} = 2\delta(x)$ and $|x| = x\epsilon(x)$ hold. For the representation of the gamma matrices in this work, we follow the convention in Ref. [121].

The creation and annihilation operators in terms of the 2DHO basis with the momentum fraction weighted variables are

$$a(x,k^\perp,\lambda) = \frac{1}{\sqrt{x}}\sum_{n,m}\Psi_n^m(\frac{k^\perp}{\sqrt{x}})\alpha(x,n,m,\lambda)\ , \tag{4.45}$$

$$b(x,p^\perp,s,t) = \frac{1}{\sqrt{x}}\sum_{n,m}\Psi_n^m(\frac{q^\perp}{\sqrt{x}})\beta(x,n,m,s,t)\ , \tag{4.46}$$

with the anti/commutation relations

$$[\alpha(x,n,m,\lambda),\alpha^\dagger(x',n',m',\lambda)] = \delta_{x,x'}\delta_{n,n'}\delta_{m,m'}\delta_{\lambda,\lambda'}\ , \tag{4.47}$$

$$\{\beta(x,n,m,s,t),\beta^\dagger(x',n',m',s',t')\} = \delta_{x,x'}\delta_{n,n'}\delta_{m,m'}\delta_{s,s'}\delta_{t,t'}\ . \tag{4.48}$$

4.3.5 Mass-squared operator

The adoption of the 2DHO s.p. basis in the transverse direction allows the spurious COM excitation for the mass spectrum. In order to eliminate the states with COM excitation in the BLFQ approach, we follow Ref. [110] and introduce a Lipkin-Lawson Lagrange multiplier term [134, 133] to the mass-squared operator $H_{\rm LC}$ [Eq. (4.16)]. The modified mass-squared operator is

$$H = H_{\rm LC} + \Lambda(H_{\rm COM} - 2b^2 I)\ , \tag{4.49}$$

where $\Lambda > 0$ is the Lagrangian multiplier. The intrinsic motion in the solutions is not influenced by this Lawson term $(H_{\rm COM} - 2b^2 I)$ due to the factorization of the LFWF in the 2DHO basis with $N_{\rm max}$ truncation. The mass spectrum of the intrinsic motion is only determined by the intrinsic part of the LFWF below the scale set by Λ. The COM motion is governed by

$$H_{\rm COM} = \left(P^\perp\right)^2 + b^4\left(R^\perp\right)^2, \tag{4.50}$$

where the COM momentum and coordinate in the transverse direction are, respectively,

$$P^\perp = \sum_i p_i^\perp,\ R^\perp = \sum_i x_i r_i^\perp. \tag{4.51}$$

In terms of momentum fraction weighted variables (see definitions in Appendix D), these COM variables are

$$P^{\perp} = \sum_i \sqrt{x_i} q_i^{\perp}, \; R^{\perp} = \sum_i \sqrt{x_i} s_i^{\perp}. \tag{4.52}$$

$H_{\rm COM}$ satisfies the eigenequation

$$H_{\rm COM}|\tilde{N}\tilde{M}\rangle = (2\tilde{N} + |\tilde{M}| + 1)2b^2|\tilde{N}\tilde{M}\rangle, \tag{4.53}$$

where $|\tilde{N}\tilde{M}\rangle$ is the eigenvector that corresponds to the eigenvalue $\mathcal{E}_{\tilde{N}\tilde{M}} = (2\tilde{N} + |\tilde{M}| + 1)2b^2$. Based on Eq. (4.53), it is easy to see that the states with COM excitation (i.e., states with $\tilde{N} \neq 0$ and/or $\tilde{M} \neq 0$) are lifted in the spectrum; only the states with the lowest COM mode (i.e., states with $\tilde{N} = \tilde{M} = 0$) remain without a shift [135]. In general, the spectrum of H is a set of equally spaced approximate copies [1] (named as subspectra), with the spacing characterized by $2\Lambda b^2$ for every additional excitation quanta in the COM degree of freedom. In practice, we choose Λ to be sufficiently large such that the subspectra with different COM modes are well separated.

Making use of the LF Hamiltonian density $\mathcal{P}^-$ [Eq. (4.18)] and the mode expansions for the pion and nucleon fields [Eqs. (4.34) and (4.36)], we calculate the mass-squared operator [Eq. (4.16)] as

$$H_{\rm LC} = P^+ \underbrace{\left(P^-_{\rm KE_N} + P^-_{\rm KE_\pi} - P^-_{\rm int}\right)}_{P^-} - \left(P^{\perp}\right)^2, \tag{4.54}$$

where $P^-_{\rm KE_N}$ and $P^-_{\rm KE_\pi}$ denote the contributions from a free nucleon and a free pion, respectively. $P^-_{\rm int}$ denotes the $N\pi$-interaction term (only for one-pion processes) in this work. The detailed expressions of $P^+P^-_{\rm KE_N}$, $P^+P^-_{\rm KE_\pi}$ and $P^+P^-_{\rm int}$ are shown in Appendix E.

4.3.6 Observables

In terms of the LF basis set $\{|\xi\rangle\}$ [Eq. (4.27)], the matrix of the modified mass-squared operator for the $N\pi$ system [Eq. (4.49)] can be constructed. By solving the eigenequation (via numerical

[1] The copies are not exact numerical copies since the addition of available quanta to the COM motion means the loss of available quanta in the relative motion.

matrix diagonalization)

$$H|\Psi_i\rangle = M_i^2|\Psi_i\rangle \ , \tag{4.55}$$

we obtain the eigenmass M_i and the corresponding eigenvector

$$|\Psi_i\rangle \equiv \sum_\xi C_i(\xi)\ |\xi\rangle \ , \tag{4.56}$$

with $C_i(\xi) = \langle\xi|\Psi_i\rangle$ being the LF amplitude corresponding to the basis state $|\xi\rangle$. The summation is taken over the LF basis set $\{|\xi\rangle\}$. The LFWF is made up by the LF amplitudes $\{\langle\xi|\Psi_i\rangle\}$. For computational efficiency, we limit the summation in Eq. (4.56) to basis states of a specified symmetry as discussed above in Sec. 4.3.3.3. Separate calculations are then performed to obtain solutions of each desired symmetry.

We can apply the LFWF [2] to compute observables for the hadronic structure, such as the PDF, the elastic electric and magnetic form factors, and the spin decomposition. As illustrations, we present the calculations of the PDF and the Dirac form factor in this work.

4.3.6.1 PDF

The probability to find a constituent nucleon of the longitudinal momentum fraction x_N in the current $N\pi$ model is

$$f(x_N) = {\sum}' C^*(\xi)C(\xi) \ , \tag{4.57}$$

where it is understood that $x_\pi = 1 - x_N$ due to the conservation of the longitudinal momentum. The primed sum in Eq. (4.57) denotes that the sum is over all the quantum numbers in Eq. (4.27) except x_N (and x_π). Since the sum is performed for the amplitudes corresponding to a selected state of interest, the index i is suppressed. Note that the right hand side of the above equation is a function of x_N.

[2] In principle, the application of the Fock-sector truncation requires the renormalization of the LFWF (see, e.g., Ref. [109]). However, we will defer this study to a future effort.

4.3.6.2 Dirac form factor

In the LF coordinates, the Dirac form factor can be computed as [136]

$$F_1(Q^2) = \langle P', \uparrow | \frac{J^+(0)}{2P^+} | P, \uparrow \rangle \ , \tag{4.58}$$

where the upward arrows denote the initial and final states with the projections of the total angular momenta being $+\frac{1}{2}$. P and P' are the momenta of the initial and finial states, respectively. $q = P' - P$ is the momentum carried by the probing virtual photon. Adopting the Drell-Yan frame, we have

$$q = \left(q^+, q^-, q^\perp\right) = \left(0, -\frac{q^2}{P^+}, q^\perp\right) \ , \tag{4.59}$$

$$P = \left(P^+, P^-, P^\perp\right) = \left(P^+, \frac{M^2}{P^+}, 0\right) \ , \tag{4.60}$$

$$q^2 = -2P \cdot q = -\left(q^\perp\right)^2 \ \equiv -Q^2 \ , \tag{4.61}$$

where Q^2 is referred to as the squared transverse momentum transfer in the following. In principle, the Dirac form factor (or, more generally, observables) should be frame independent due to the Lorentz invariance. In practice, however, the Lorentz symmetry is broken by the Fock-sector truncation in our model [137, 138, 139].[3] The frame dependence of the Dirac form factor could hence serve as a measure of the Lorentz symmetry violation, which will be the topic of a future work.

In our current model, the Fock-sector expansion for the physical proton can be schematically written as

$$|p_{\rm phys}\rangle = a_p |p\rangle + a_{p\pi^0} |p\pi^0\rangle + a_{n\pi^+} |n\pi^+\rangle \ \ , \tag{4.62}$$

where a_p, $a_{p\pi^0}$ and $a_{n\pi^+}$ schematically represent the amplitudes since each term on the right hand side of Eq. (4.62) represents a sum over of the basis states with corresponding amplitudes. Hence, there are three different classes of contributions to the Dirac form factor of the physical proton:

[3] In this work, higher Fock sectors, such as $|N\pi\pi\rangle$, are omitted in Eq. (4.26). As the higher Fock sectors are systematically included in our model, the Lorentz symmetry can be dynamically restored, through which we anticipate that the Dirac form factor gradually becomes frame independent.

(1) the virtual photon couples to the current of the bare proton $|p\rangle$, which results in $F^p_{1,f}(Q^2)$; (2) the virtual photon couples to the current of the bare proton when dressed by charge-neutral π^0, which results in $F^{p\pi^0}_{1,f}(Q^2)$; and (3) the virtual photon couples to the current of π^+, which results in $F^{n\pi^+}_{1,b}(Q^2)$. The Dirac form factor for the physical proton is hence

$$F_1(Q^2) = F^p_{1,f}(Q^2) + F^{p\pi^0}_{1,f}(Q^2) + F^{n\pi^+}_{1,b}(Q^2) \ , \tag{4.63}$$

where the subscripts f and b denote the contributions to $F_1(Q^2)$ from the fermionic current and the bosonic current, respectively. The detailed expression of $F_1(Q^2)$ is shown in Appendix F.

4.4 Results and discussions

In this work, we adopt the Fock-sector-dependent renormalization (FSDR) [140, 141, 142, 143] scheme. We numerically diagonalize the matrix of the modified mass-squared operator H [Eq. (4.49)] using an iterative process where the bare nucleon mass is tuned in the matrix elements within the single-nucleon sector. This process continues until the square-root of the eigenvalue of the ground state (identified as a physical proton) matches the mass of the physical proton (taken as 938 MeV in this work).

According to the FSDR scheme, the mass counterterm is introduced only to the single-nucleon sector. We expect the mass counterterm to compensate for the mass correction due to the radiative processes: the quantum fluctuation from the single-nucleon sector to the $N\pi$ sector and back again. On the other hand, the nucleon mass in the $N\pi$ sector remains as the physical value until a future effort would renormalize it with the inclusion of a higher Fock sector. We fix the pion mass at 137 MeV in the FSDR procedure.

4.4.1 Mass spectrum of the $N\pi$ system

We first study the dependence of the mass spectrum of the $N\pi$ system on the model space, which is determined by the truncation parameters, $N_{\max}$ and $K_{\max}$, and the basis strength, b. For convenience, we set $K_{\max}$ to be $N_{\max} + 1/2$ throughout this work.

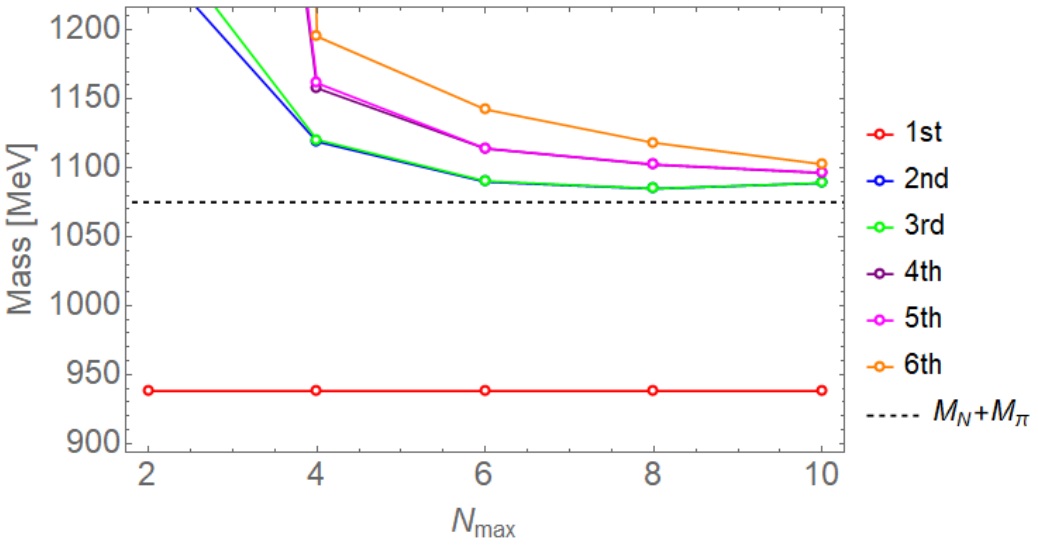

Figure 4.1: (Adopted from Ref. [6]) Model space dependence of the spectrum of the $N\pi$ system computed via the BLFQ approach. The masses corresponding to the lowest 6 eigenstates are plotted as functions of $N_{\max}$ (set to be $K_{\max} - \frac{1}{2}$). The basis strength is fixed as $b = 250$ MeV. The dashed line (at 1075 MeV) shows the threshold of the continuum of the $N\pi$ system. The ground state (bound) is identified as the physical proton whose mass is set to 938 MeV in the FSDR scheme (see the text for details).

In Fig. 4.1, we show the lowest 6 states in the mass spectrum of the $N\pi$ system as a function of $N_{\max}$, where we choose $b = 250$ MeV as an example. We identify the ground (and also bound) state as the (physical) proton, of which the eigenvalue has been renormalized to 938 MeV by the FSDR procedure. The corresponding LFWF is boost invariant; it encodes the information of the intrinsic structure of the proton. The other states lie above the threshold of the continuum, which is the sum of the physical pion and proton masses adopted in this work (i.e., 1075 MeV), and therefore represent $N\pi$ scattering states.

We find all the eigenenergies of these 6 states seem to converge as $N_{\max}$ increases. The proof of the convergence is complicated and demanding in computing power, especially with continuum states emerging in the spectrum. As $N_{\max}$ increases, a better representation of the scattering states of the $N\pi$ system is anticipated. This can be inferred from the increasing level density of

the scattering states as $N_{\max}$ increases. We defer detailed investigation of these continuum states to a later effort.

4.4.2 Proton's LFWF

To compute the proton's LFWF, we need to fix the basis strength b besides fixing the bare nucleon mass via the FSDR procedure for each choice of $N_{\max}$ (recall $K_{\max} = N_{\max} + 1/2$). This is achieved by varying b to fit the r.m.s. charge radius of a proton $\sqrt{\langle r^2_{p,E}\rangle}$, which is 0.844 fm (see, e.g., Ref. [144]). Overall, we fit for each $N_{\max}$ both the mass and the r.m.s. charge radius to respective physical values in order to determine the mass counterterm and b in computing the proton's LFWF. In Table 4.1, we list the resulting model space parameters ($N_{\max}$ and b) to obtain the proton's LFWFs.

Table 4.1: Model space parameters employed to obtain the proton's LFWFs.

$N_{\max}$	6	8	10
b [MeV]	176.95	245.54	279.55

Table 4.2: Fock-sector probabilities [Eq. (4.62)] computed from the proton's LFWFs.

$N_{\max}$	$\lvert a_p\rvert^2$	$\lvert a_{n\pi^+}\rvert^2$	$\lvert a_{p\pi^0}\rvert^2$
6	0.829	0.114	0.057
8	0.694	0.204	0.102
10	0.619	0.254	0.127

Via the proton's LFWFs, we compute the probability of each Fock sector according to Eq. (4.62), as shown in Table 4.2. For each model space we apply to compute the proton LFWF (Table 4.1), we find that the probability of the bare proton sector ($|a_p|^2$) dominates, while the probability of the $|n\pi^+\rangle$ sector ($|a_{n\pi^+}|^2$) is twice of that of the $|p\pi^0\rangle$ sector ($|a_{p\pi^0}|^2$).

4.4.3 Proton's PDF

We apply the proton's LFWF to compute its PDF, which encodes the distribution of the longitudinal momentum carried by its constituents. In this work, such PDF also represents the probability that a proton fluctuates into the constituent nucleon (of the longitudinal momentum fraction x_N) and pion (of the longitudinal momentum fraction x_π).

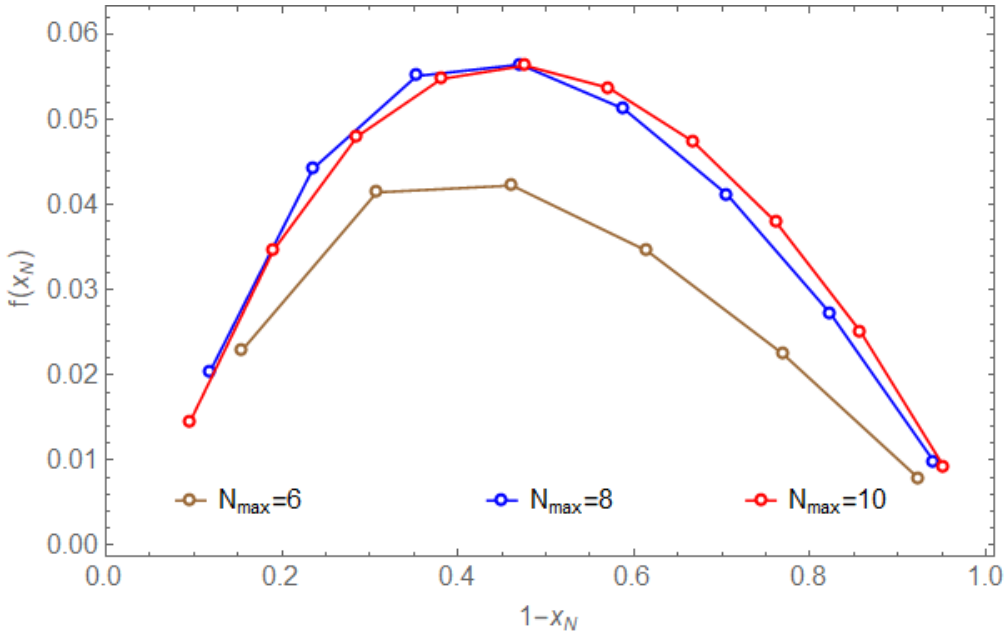

Figure 4.2: (Adopted from Ref. [6]) The proton's PDF, $f(x_N)$, as a function of the longitudinal momentum fraction of the constituent nucleon x_N (note we rescale the x-axis as $1 - x_N = x_\pi$ in the plot) and of the model space (defined by $N_{\max}$ and b). The details are in the text.

In Fig. 4.2, the proton's PDF, $f(x_N)$, is shown as a function of x_N and of the model space (with parameter set shown in Table 4.1). Note we rescale the x-axis as $x_\pi = 1 - x_N$ in the plot. We do not show the result for $f(x_N = 1)$ in Fig. 4.2, which represents the probability to find a bare nucleon in the physical proton ($|a_p|^2$ as in Eq. (4.62)) in different model spaces. For the cases with $N_{\max} = 6$, 8 and 10, such probabilities are 0.83, 0.69, and 0.62, respectively.

For each $N_{\max}$, we checked that $f(x_N)$ satisfies both the normalization condition and the momentum sum rule. As $N_{\max}$ increases, $f(x_N)$ seems to converge (as indicated by the spacing

between the curves and the positions of the peaks in the plot). Our results of $f(x_N)$ peak at about $x_\pi = 0.45$ (or $x_N = 0.55$) for the model spaces with $N_{\max} = 8$ and 10. In the future, we plan to investigate in detail the model-space dependence of $f(x_N)$. Also, the internal degrees of freedom of the constituent nucleon and pion will be included to study the flavor asymmetry of the proton [145, 146, 147, 148].

4.4.4 Proton's Dirac form factor

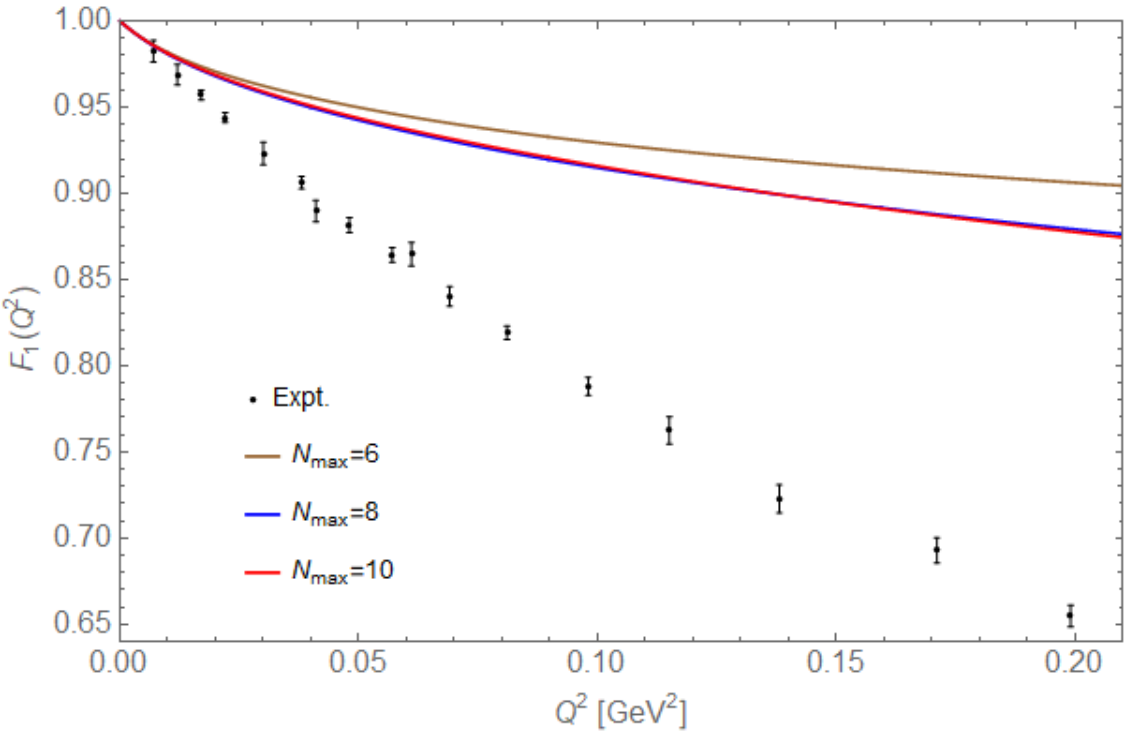

Figure 4.3: The computed Dirac form factor $F_1(Q^2)$ of the proton as a function of the squared transverse momentum transfer Q^2 and of the model space (determined by $N_{\max}$ and b, with $N_{\max} = K_{\max} - \frac{1}{2}$). The basis parameters used to computed the LFWFs are given in Table 4.1. The experimental results (black) [149], along with the corresponding error bars, are also presented for comparison.

We apply the boost invariant LFWFs to compute the proton's Dirac form factor. In Fig. 4.3, we present the proton's Dirac form factor $F_1(Q^2)$ [Eq. (4.63)] as a function of the squared transverse momentum transfer Q^2 [Eq. (4.61)] and of the model space (determined by $N_{\max}$ and b).

As $N_{\max}$ increases, the computed $F_1(Q^2)$ seems to converge (as seen from the spacing of curves). Note we tune b for each choice of $N_{\max}$ such that the proton's LFWF produce the experimental value of $\sqrt{\langle r_{p,E}^2 \rangle}$ (and also the physical proton's mass). This can be seen from the agreement between the slopes of the computed $F_1(Q^2)$ and that of the experimental result in the vicinity of the origin (details shown in Fig. 4.4). Note the slope of the $F_1(Q^2)$ in the limit of vanishing Q^2 is related to the r.m.s. charge radius as [150]

$$\langle r_{p,E}^2 \rangle = -6 \frac{dG_E(Q^2)}{dQ^2}\bigg|_{Q^2 \to 0} , \tag{4.64}$$

where $G_E(Q^2)$ is the Sachs electric form factor

$$G_E(Q^2) = F_1(Q^2) - \frac{Q^2}{4M_N^2} F_2(Q^2) . \tag{4.65}$$

In this work, we take proton Pauli form factor at $Q^2 = 0$ to be $F_2(0) = 1.79280$, in units of the nuclear magneton μ_N, when extracting the r.m.s. charge radius according to Eq. (4.64). Refining this approach will be a future research effort. In the limit of vanishing Q^2, we find $F_1(0) = 1$, which indicates the conservation of charge. This also shows a proper normalization of the proton's LFWFs. In the current work, the normalization is precise to at least eight significant figures. In the limit of $Q^2 \to \infty$, the $F_1(\infty)$ is equal to the probability of the bare proton sector $|a_p|^2$ (as shown in Eq. (4.62) and Table 4.2), representing the point-like proton.

We find the computed $F_1(Q^2)$ deviates from the experimental results as Q^2 increases. Implementing larger model spaces (by increasing $N_{\max}$) could increase the range of agreement. However, the major reason for this deviation is the simplicity of the chiral model adopted in this work. As pointed out (e.g., Ref. [151]), inclusion of the vector mesons and also the Δ-resonance state of pion and nucleon can increase the range of agreement up to about $Q^2 = 0.16$ GeV^2. To achieve the agreement for even higher Q^2, more fundamental degrees of freedom (quarks and gluons) need to be included (e.g., Ref. [152]).

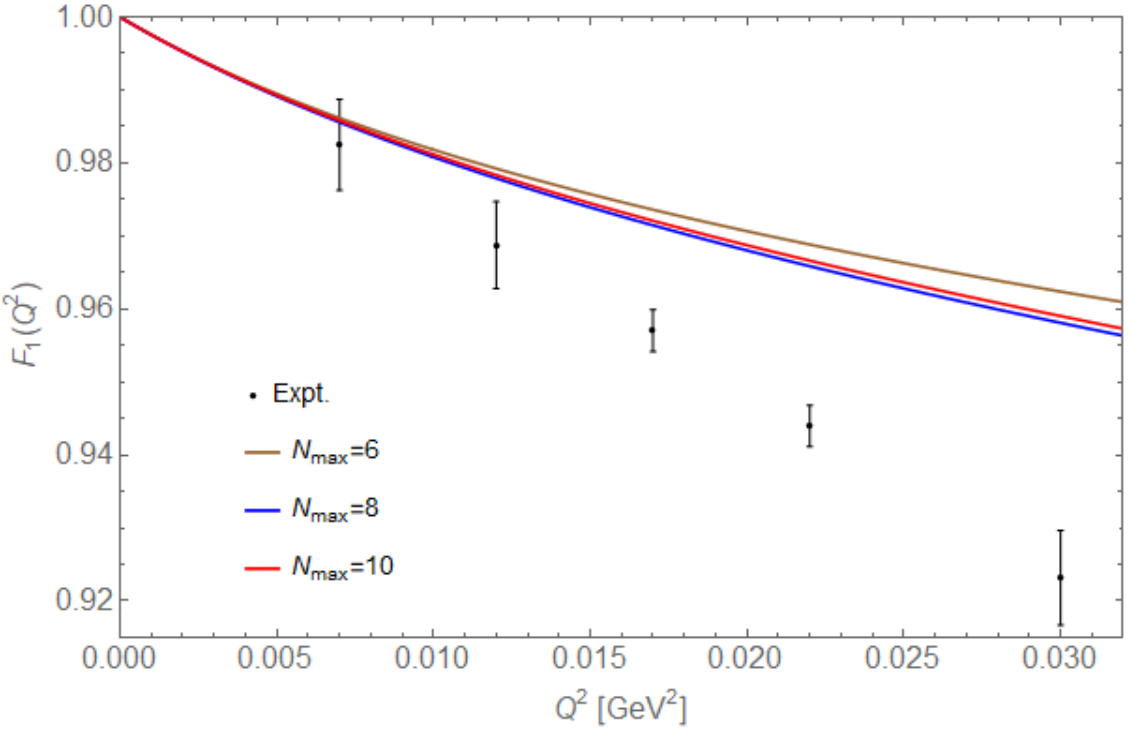

Figure 4.4: Dirac form factor $F_1(Q^2)$ for the proton as a function of the squared transverse momentum transfer Q^2 and of the model space (determined by $N_{\max}$ and b). The basis parameters used for calculating the LFWFs are presented in Table 4.1. The experimental results (black), along with the corresponding error bars, are also presented for comparison. Note the result with the model space parameter $N_{\max} = 8$ and $b = 245.54$ MeV nearly coincides with the result computed with $N_{\max} = 10$ and $b = 279.55$ MeV over the range of Q^2 shown here.

4.4.5 An improved model for the proton's Dirac form factor

We implement a simple model in order to improve the calculation of the proton's Dirac form factor. To this end, we modify Eq. (4.63) to be

$$F_1(\alpha_1, \alpha_2, Q^2) = D_1(\alpha_1, Q^2)\left[F^p_{1,f}(Q^2) + F^{p\pi^0}_{1,f}(Q^2)\right] + D_2(\alpha_2, Q^2)F^{n\pi^+}_{1,b}(Q^2)\ , \tag{4.66}$$

where $D_1(\alpha_1, Q^2)$ and $D_2(\alpha_2, Q^2)$ are the auxiliary functions to correct for anticipated contributions from the finite charge distributions of the bare proton and the charged π^+, respectively. α_1 and α_2

are the parameters. We remark that (1) we do not consider the corrections of the charge-neutral constituents (i.e., the bare neutron and π^0) since they do not contribute to the Dirac form factor up to the chiral order in this work (i.e., next to leading order); (2) the explicit forms of the auxiliary functions could be determined by fitting the experimental data or by the input from other theories (on, e.g., more fundamental degrees of freedom of the nucleon and pion).

As an initial test to gain some useful insights, we take the auxiliary functions to be of the same dipole form [4]

$$D_1(\alpha_1, Q^2) = D_2(\alpha_2, Q^2) \equiv D(\alpha, Q^2) = \frac{1}{(1+\alpha Q^2)^2} \ , \tag{4.67}$$

with a parameter α. The modified model for the proton's Dirac form factor [Eq. (4.66)] hence simplifies

$$F_1(\alpha, Q^2) = D(\alpha, Q^2)\Big[F_{1,f}^{p}(Q^2) + F_{1,f}^{p\pi^0}(Q^2) + F_{1,b}^{n\pi^+}(Q^2)\Big] \ . \tag{4.68}$$

With this improved model, we calculate the proton's LFWF following the similar procedures of parameter fitting as before. That is, we tune α, b and bare nucleon mass for each $N_{\max}$ such that (1) the ground state of the $N\pi$ system produces the physical proton mass after the FSDR procedure; (2) the computed proton's r.m.s. charge radius matches the experimental value. The resulting parameter set are shown in Table 4.3.

Table 4.3: Parameter set of the model spaces (determined by $N_{\max}$ and b) and of the auxiliary function $D(\alpha, Q^2)$ employed to obtain the mass and r.m.s. charge radius of the proton. Note the modified model Eq. (4.68) is employed to calculate the proton's Dirac form factor. We again set $N_{\max} = K_{\max} - \frac{1}{2}$.

$N_{\max}$	6	8	10
α [GeV^{-2}]	1.00	1.05	1.10
b [MeV]	754.96	1147.04	1198.44

[4] A monopole form is more realistic, and commonly used for the pion form factor; we will present the corresponding investigation in an upcoming work.

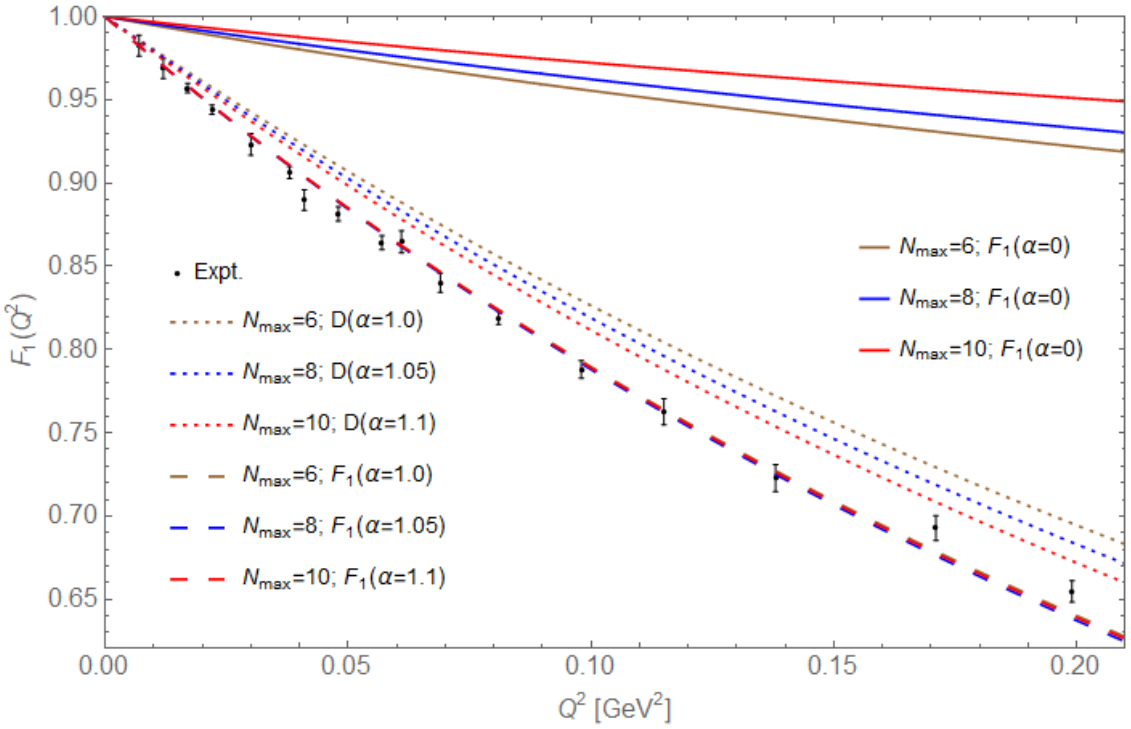

Figure 4.5: The computed Dirac form factor $F_1(Q^2)$ of the proton as a function of the squared transverse momentum transfer Q^2 based on the improved model [Eq. (4.68)]. The parameters of the model spaces, $N_{\max}$ and b, and the corresponding parameter of the auxiliary function, α, are shown in Table 4.3. The experimental results (black), along with the corresponding error bars, are also presented for comparison. The colored lines with the coarse dashes (which coincide with the experimental data) present the computed $F_1(Q^2)$ based on Eq. (4.68). The colored lines with the fine dashes show the behavior of the auxiliary function $D(\alpha, Q^2)$, while the colored solid lines present the contributions from $F_1(\alpha = 0, Q^2)$, i.e., F_1 calculated with the point-charge assumption.

We show this improved proton's Dirac form factor $F_1(Q^2)$, along with the auxiliary function, as a function of the squared transverse momentum transfer Q^2 and of the model space (determined by $N_{\max}$ and b) in Fig. 4.5. For each model space and the corresponding auxiliary function with parameters shown in Table 4.3, we find the computed $F_1(Q^2)$ based on the modified model [Eq. (4.68)] agrees well with the experimental data within the range of the squared transverse momentum

transfer up to 0.20 GeV^2. Beyond this range, our simple model needs to be further improved (see, e.g., [153]).

CHAPTER 5. CONCLUSIONS AND OUTLOOKS

5.1 Effective interactions and operators

Our initial application to the deuteron ground state revealed the order-of-magnitude effects of simple P-space (or "model space") basis truncations compared with exact results as a function of the harmonic oscillator (HO) basis strength $\hbar\Omega$ for a set of realistic nucleon-nucleon (NN) interactions. The smallest value studied, $\hbar\Omega = 5$ MeV, produced the largest truncation effects (hence the largest renormalization effects) for these interactions. We also showed that, for a wide range of P-spaces and a selection of NN interactions, the Okubo-Lee-Suzuki (OLS) approach consistently reproduced the exact results which one anticipates from a theoretical perspective.

Effective Hamiltonians and effective electroweak operators were then calculated for two nucleons in a confining harmonic oscillator trap as a function of the P-space. For this system, matrix elements of all OLS-derived effective operators again agree with exact results in all model spaces and for all traps investigated. We quantify the deviations of the simple truncated space results from the exact results for three different traps as a function of the P-space. We illustrate these effects for the root-mean-square (r.m.s.) point-proton radius, electric quadrupole moment, magnetic dipole moment, Gamow-Teller (GT) transition and neutrinoless double-beta ($0\nu2\beta$) decay operators using NN interactions from chiral effective field theory.

From the results shown in Figs. 2.3, 2.4 and 2.5, we found that the size of the error in the matrix element of an observable introduced by a truncated basis space approach depends on the observable, the value of the HO parameter of the trap $\hbar\Omega$, and the severity of the P-space truncation given by $N_{\max}$. Long-range observables, such as the r.m.s. point-proton radius and the electric quadrupole moment exhibited larger errors due to truncation to smaller spaces than the magnetic dipole and GT operators. We also found surprisingly large truncation errors for the $0\nu2\beta$ decay operator — larger than that of the electric quadrupole moment, and of the same order as the r.m.s.

point-proton radius. Such cases suggest that a careful treatment of renormalization effects must be implemented for $0\nu2\beta$-decay matrix elements in limited basis spaces. This careful theoretical effort is needed in view of the significant experimental efforts that are aimed at searches for $0\nu2\beta$ decay which require significant investments in new experimental facilities. On the other hand, the GT operator exhibited behaviors similar to the magnetic moment as may be expected.

While these results appear to be reasonable in the qualitative sense and are consistent with previous investigations, the quantitative dependences shown here may be useful in estimating uncertainties for observables obtained in truncated many-body calculations with realistic NN interactions. In particular, since renormalization effects tend to be larger in cases with weaker traps and smaller basis spaces, applications to heavier nuclei, for both transitions between weakly bound nucleons and to continuum states, will likely be subject to the more significant renormalization effects.

The results presented here also signal the approximate magnitude of the corrections that the OLS renormalization provides for each of our selected observables. These corrections, which can be obtained with OLS renormalization, should be carried forward to the appropriate many-body applications. It will also be important to implement the chiral effective field theory treatment of the electroweak operators that are consistent with the chiral effective field theory of the strong internucleon interactions.

(This section is essentially from the published paper [2].)

5.2 Time-dependent basis function method

We develop an *ab initio*, non-perturbative approach to treat the non-relativistic nuclear structure and scattering problems in a unified manner. We call this approach the time-dependent Basis Function (tBF) method. Within the tBF formalism, the state vector of the system is calculated at the amplitude level during the scattering, by explicitly evaluating the time-evolution operator. The full quantal coherence is therefore retained and we are able to study the detailed dynamics for complex scattering processes.

As an initial test problem for illustrating the tBF method, we study the Coulomb excitation of a deuteron in a weak harmonic potential (the setup shown in Fig. 3.1). We scatter a U^{92+} projectile (with the incident speed $v = 0.1,\ 0.2,\ 0.4$ and the impact parameter $b = 5$ fm) to generate the time-varying Coulomb field, for which the multipole decomposition is performed and only the $E1$ component is kept for illustration.

In this simple application of the tBF formalism, the structure of the target is solved using the JISP16 NN interaction. With the 3DHO representation, we construct the target Hamiltonian setting the full space truncation parameter $N_{\max} \leq 60$ and basis strength $\omega = 5$ MeV. To localize the target and to regulate the continuum states, we also introduce a weak HO trap of strength 5 MeV for the target Hamiltonian. By diagonalization of the target Hamiltonian, the lowest 7 states in the interaction channels $({}^3S_1,\ {}^3D_1)$, ${}^3P_0$ and ${}^3P_1$ are solved (Fig. 3.2). We select these states as a basis set to construct a basis representation for the time-dependent solution of the target under scattering. Note the center of mass excitation of the target is neglected for simplicity.

Within the basis representation, the time-dependent state vector of the target becomes the wave function, which consists of a set of amplitudes of respective basis states. Meanwhile, the equation of motion for the scattering takes the form of matrix multiplications. In this work, we prepare the initial target to be polarized in the state $({}^3S_1,\ {}^3D_1),\ M = -1$ and solve the wave function during the scattering numerically by the MSD2 scheme. In order to reveal the importance of higher-order effects in the scattering, we also solve the wave function via first-order perturbation theory.

The time-dependent wave function, obtained via either the MSD2 or first-order perturbation theory, is used to investigate the intrinsic excitations of the target. We study the transition probabilities to different basis states as functions of the exposure time and the incident speed. We find that abrupt transitions occur during the scattering, when the strength of the Coulomb field is strong and its time-variation is rapid. The transitions subside and approach asymptotic values as the Coulomb field subsides.

We also study the feeding of allowed and forbidden states. We find that higher-order transitions occur later and build smaller populations for the forbidden states. With increasing incident speed,

first-order effects dominate the transitions, with non-monotonic dependencies of the transition probabilities on the incident speed clearly visible in the simulations. This could be due to the restricted basis representation for the target in the current model problem.

The tBF method enables us to study the evolution of the target observables, such as the r.m.s. charge radius, the r.m.s. intrinsic momentum, the r.m.s. angular momentum, the intrinsic energy and the $\hat{z}$-projection of the total angular momentum. Applying the matrix representations of the corresponding operators as well as the time-dependent wave functions, we study the evolution of the observables according to the exposure time and the incident speed. The evolution of these observables is analyzed based on the transition probabilities to different basis states, from which we obtain the transfer of the energy, the momentum and the angular momentum between the background field and the target during the scattering.

By the tBF method, we expose the dynamics of the scattering directly from the evolution of the internal charge distribution of the target. To illustrate, we show the difference in internal charge distributions between the scattered and initial targets for the case with the incident speed $v = 0.1$. We find that the scattering of the target in the time-varying Coulomb field is divided into three sequential stages, i.e., the polarization stage, the transition stage and the stabilization stage. At the end of the scattering, the excitation in the intrinsic degrees of freedom, such as the rotation and fluctuation of the charge density, is evident.

In the future, we will remove the trap and adopt a more complete description for both the interaction channels and the time-varying EM field to investigate the complex processes such as the reorientation [154, 155, 156], the dissociation [157, 158, 159] of the deuteron system and the dependence on the NN interaction. The scattering due to the strong nuclear interaction with the heavy ion will also be included in future work.

(This section is essentially from the published paper [4].)

5.3 Chiral nucleon-pion model via Basis Light-Front Quantization

In this work, we apply, for the first time, the Basis Light-Front Quantization (BLFQ) approach [84] to study a chiral model for the nucleon-pion ($N\pi$) system via an *ab initio*, non-perturbative, Hamiltonian approach. We demonstrate the approach with a test problem, in which a physical proton is treated as the relativistic bound state of the $N\pi$ system.

Starting from the Lagrangian density for the chiral model of the $N\pi$ system [124, 125], we proceed with a Legendre transformation to obtain the corresponding light-front (LF) Hamiltonian density. In this work, we keep only the Fock sectors $|N\rangle$ and $|N\pi\rangle$. Correspondingly, we restrict the interaction terms in the LF Hamiltonian density and keep only the terms that correspond to the single-pion emission and absorption processes.

We then show our choice of the construction and truncation schemes of the LF basis. In particular, we employ the discretized plane wave basis in the longitudinal direction and the two dimensional harmonic oscillator basis in the transverse direction. Besides the basis sets in momentum space, we also discuss our choice of the basis set in spin and isospin degrees of freedom. We prune our basis according to the symmetries of the Hamiltonian for our chosen system.

We construct the matrix of the mass-squared operator within the LF basis representation, where we regulate the center of mass excitation by the Lipkin-Lawson method [133, 134]. Incorporating the Fock-sector-dependent renormalization (FDSR) [140, 141, 142, 143] scheme, we obtain the mass spectrum of the proton and the corresponding boost-invariant light-front wave function (LFWF) by solving the eigenvalue problem of the mass-squared operator.

The mass spectrum of the $N\pi$ system in our solution includes both the bound and scattering states. We study the model space dependence of the spectrum. In particular, we investigate the lowest 6 states as a function of the model space, which is determined by the truncation parameters ($N_{\max}$ and $K_{\max}$), basis strength (b), and the current choice of Fock sectors. With increasing dimensionality, we find all the eigenvalues of these 6 states seem to converge, while the scattering states of the $N\pi$ system produce improving representations of the continuum. We also find the eigenvalue of the ground state produces the physical proton mass for each model space with proper

choice of the mass counterterm. Note that larger Fock spaces are necessary in order to verify the convergence which we postpone to a future work.

To study the proton's parton distribution function (PDF) and also its Dirac form factor $F_1(Q^2)$, we compute the proton's LFWFs in a sequence of model spaces (determined by $N_{\max}$, $K_{\max}$ and b) where both the proton's mass and its r.m.s. charge radius are fitted to respective experimental values. We investigate the dependencies of the resulting PDF on the longitudinal momentum fraction of the constituent nucleon (x_N) and on the model space. We find the proton's PDF seems to converge with increasing dimension of model space. For the model spaces with $N_{\max} = 8$ and 10, the computed PDFs peak at about $x_N = 0.55$ (or $x_\pi = 0.45$). Further inclusion of the quark distribution functions of the constituents will hopefully reveal the pion cloud's role in the light quark flavor asymmetry of the proton (see, e.g., Ref. [148]).

We also study the proton's Dirac form factor $F_1(Q^2)$ as a function of the squared transverse momentum transfer Q^2 and the model space. We find that $F_1(Q^2)$, as for the PDF, seems also to converge with increasing dimension of the model space. However, for all choices of model space, the results of $F_1(Q^2)$ deviate from the experimental results when Q^2 increases. We argue this is mainly because of the simplicity of the chiral model in this work, i.e., 1) only nucleons and pions are included; 2) both species are taken to be structureless, point-like particles. For a phenomenological improvement, we implement a simple model that describes the finite charge distributions of the constituents to calculate the proton's $F_1(Q^2)$. We find the resulting $F_1(Q^2)$ agrees well with the experimental data for $Q^2 \leq 0.20$ GeV^2.

This work can lead to multiple paths in the future. We attempt to connect the current chiral model to the modern chiral effective theory (see, e.g., [42, 160] and references therein). This work is currently ongoing. After this connection is accomplished, we plan to extend the current calculation to incorporate systematically the contributions from higher Fock sectors, where we will examine the basis-space dependence as well as the convergence of the Fock-sector expansion. We expect such investigations to be demanding in computing power. We plan to incorporate the technology of high performance computing (see Ref. [3] and references therein).

The current framework can be straightforwardly extended to investigate more nucleonic observables of experimental interest, such as the transverse momentum distribution, and various categories of form factors. In addition, this framework can be extended to study more complicated nuclear systems, such as the deuteron, where the role of the relativistic dynamics is important but still unclear.

BIBLIOGRAPHY

[1] DOE/NSF Nuclear Science Advisory Committe, The Frontiers of Nuclear Science: A Long-Range Plan, 2007.

[2] J. P. Vary, R. Basili, W. Du, M. Lockner, P. Maris, S. Pal and S. Sarker, Phys. Rev. C **98**, no. 6, 065502 (2018).

[3] J. P. Vary, R. Basili, W. Du, M. Lockner, P. Maris, D. Oryspayev, S. Pal, S. Sarker, H. M. Aktulga, E. Ng, M. Shao and C. Yang, Proceedings of the International Conference 'Nuclear Theory in the Supercomputing Era-2016' (NTSE-2016), Khabarovsk, Russia, September 19-23, 2016. Eds. A. M. Shirokov and A. I. Mazur. Pacific National University, Khabarovsk, Russia, 2018, p. 15.

[4] W. Du, P. Yin, Y. Li, G. Chen, W. Zuo, X. Zhao and J. P. Vary, Phys. Rev. C **97**, no. 6, 064620 (2018).

[5] W. Du, P. Yin, G. Chen, X. Zhao and J. P. Vary, Proceedings of the International Conference 'Nuclear Theory in the Supercomputing Era-2016' (NTSE-2016), Khabarovsk, Russia, September 19-23, 2016. Eds. A. M. Shirokov and A. I. Mazur. Pacific National University, Khabarovsk, Russia, 2018, p. 102.

[6] W. Du, Y. Li, X. Zhao, and J. P. Vary, Proceedings of the International Conference 'Nuclear Theory in the Supercomputing Era - 2018' (NTSE-2018), Daejeon, South Korea, October 29 - November 2, 2018, eds. A. M. Shirokov and A. I. Mazur. Pacific National University, Khabarovsk, Russia, 2019, p. 92.

[7] W. Du, Y. Li, X. Zhao, G. A. Miller and J. P. Vary, in preparation.

[8] J. Carlson and R. Schiavilla, Rev. Mod. Phys. **70**, 743 (1998).

[9] B. R. Barrett, P. Navratil and J. P. Vary, Prog. Part. Nucl. Phys. **69**, 131 (2013).

[10] R. B. Wiringa, V. G. J. Stoks and R. Schiavilla, Phys. Rev. C **51**, 38 (1995).

[11] P. Doleschall, Phys. Rev. C **69**, 054001 (2004).

[12] R. Machleidt, Phys. Rev. C **63**, 024001 (2001).

[13] A. M. Shirokov, J. P. Vary, A. I. Mazur and T. A. Weber, Phys. Lett. B **644**, 33 (2007).

[14] A. M. Shirokov, I. J. Shin, Y. Kim, M. Sosonkina, P. Maris and J. P. Vary, Phys. Lett. B **761**, 87 (2016).

[15] S. C. Pieper, V. R. Pandharipande, R. B. Wiringa and J. Carlson, Phys. Rev. C **64**, 014001 (2001).

[16] S. C. Pieper, R. B. Wiringa and J. Carlson, Phys. Rev. C **70**, 054325 (2004).

[17] M. Pervin, S. C. Pieper and R. B. Wiringa, Phys. Rev. C **76**, 064319 (2007).

[18] L. E. Marcucci, M. Pervin, S. C. Pieper, R. Schiavilla and R. B. Wiringa, Phys. Rev. C **78**, 065501 (2008).

[19] P. Navratil, J. P. Vary and B. R. Barrett, Phys. Rev. Lett. **84**, 5728 (2000).

[20] P. Navratil, J. P. Vary and B. R. Barrett, Phys. Rev. C **62**, 054311 (2000).

[21] H. Kummel, K. H. Luhrmann and J. G. Zabolitzky, Phys. Rept. **36**, 1 (1978).

[22] E. Epelbaum, H. Krebs, D. Lee and U. G. Meissner, Phys. Rev. Lett. **106**, 192501 (2011).

[23] S. K. Bogner, H. Hergert, J. D. Holt, A. Schwenk, S. Binder, A. Calci, J. Langhammer and R. Roth, Phys. Rev. Lett. **113**, 142501 (2014).

[24] G. R. Jansen, J. Engel, G. Hagen, P. Navratil and A. Signoracci, Phys. Rev. Lett. **113**, no. 14, 142502 (2014).

[25] G. A. Negoita *et al.*, Phys. Rev. C **99**, no. 5, 054308 (2019).

[26] I. C. Cloët *et al.*, arXiv:1903.05453 [nucl-th].

[27] V. Somà, Eur. Phys. J. Plus **133**, no. 10, 434 (2018).

[28] S. Weinberg, Phys. Lett. B **251**, 288 (1990).

[29] S. Weinberg, Nucl. Phys. B **363**, 3 (1991).

[30] U. van Kolck, Phys. Rev. C **49**, 2932 (1994).

[31] C. Ordonez, L. Ray and U. van Kolck, Phys. Rev. Lett. **72**, 1982 (1994).

[32] S. K. Bogner, R. J. Furnstahl and R. J. Perry, Phys. Rev. C **75**, 061001 (2007).

[33] S. Okubo, Prog. Theor. Phys. **12**, 603 (1954).

[34] K. Suzuki and S. Y. Lee, Prog. Theor. Phys. **64**, 2091 (1980).

[35] K. Suzuki, Prog. Theor. Phys. **68**, 246 (1982).

[36] K. Suzuki and R. Okamoto, Prog. Theor. Phys., **92**, 1045 (1994).

[37] E. Epelbaum, H. Krebs and U. G. Meiner, Phys. Rev. Lett. **115**, no. 12, 122301 (2015).

[38] E. Epelbaum, H. Krebs and U. G. Meiner, Eur. Phys. J. A **51**, no. 5, 53 (2015).

[39] P. Maris *et al.*, EPJ Web Conf. **113**, 04015 (2016).

[40] S. Binder *et al.* [LENPIC Collaboration], Phys. Rev. C **93**, no. 4, 044002 (2016).

[41] S. Binder *et al.* [LENPIC Collaboration], Phys. Rev. C **98**, no. 1, 014002 (2018).

[42] D. R. Entem and R. Machleidt, Phys. Rev. C **68**, 041001 (2003).

[43] R. Machleidt and D. R. Entem, Phys. Rept. **503**, 1 (2011).

[44] I. Stetcu, B. R. Barrett, P. Navratil and J. P. Vary, Phys. Rev. C **71**, 044325 (2005).

[45] I. Stetcu, B. R. Barrett, P. Navratil and J. P. Vary, Phys. Rev. C **73**, 037307 (2006).

[46] A. F. Lisetskiy, M. K. G. Kruse, B. R. Barrett, P. Navratil, I. Stetcu and J. P. Vary, Phys. Rev. C **80**, 024315 (2009).

[47] E. Dikmen, A. F. Lisetski, B. R. Barrett, P. Maris, A. M. Shirokov and J. P. Vary, Phys. Rev. C **91**, no. 6, 064301 (2015).

[48] D. R. Tilley, C. M. Cheves, J. L. Godwin, G. M. Hale, H. M. Hofmann, J. H. Kelley, C. G. Sheu and H. R. Weller, Nucl. Phys. A **708**, 3 (2002).

[49] I. J. Shin, Y. Kim, P. Maris, J. P. Vary, C. Forssén, J. Rotureau and N. Michel, J. Phys. G **44**, no. 7, 075103 (2017).

[50] C. P. Viazminsky and J. P. Vary, J. Math. Phys., **42**, 2055 (2001).

[51] A. Bohr and B. Mottelson, *Nuclear Structure* (World Scientific, Singapore, 1998), Vol. 1, p. 407.

[52] G. Martínez-Pinedo, A. Poves, E. Caurier and A. P. Zuker, Phys. Rev. C **53**, no. 6, R2602 (1996).

[53] G. Prezeau, M. Ramsey-Musolf and P. Vogel, Phys. Rev. D **68**, 034016 (2003).

[54] H. Feshbach, Annals Phys. **5**, 357 (1958).

[55] H. Feshbach, Annals Phys. **19**, 287 (1962) [Annals Phys. **281**, 519 (2000)].

[56] H. Witala, W. Gloeckle, J. Golak, H. Kamada, J. Kuros-Zolnierczuk, A. Nogga and R. Skibinski, Phys. Rev. C **63**, 024007 (2001).

[57] R. Lazauskas and J. Carbonell, Phys. Rev. C **70**, 044002 (2004).

[58] R. Lazauskas, Phys. Rev. C **79**, 054007 (2009).

[59] A. Deltuva and A. C. Fonseca, Phys. Rev. C **75**, 014005 (2007).

[60] A. Deltuva and A. C. Fonseca, Phys. Rev. Lett. **98**, 162502 (2007).

[61] A. Kievsky, S. Rosati, M. Viviani, L. E. Marcucci and L. Girlanda, J. Phys. G **35**, 063101 (2008).

[62] L. E. Marcucci, A. Kievsky, L. Girlanda, S. Rosati and M. Viviani, Phys. Rev. C **80**, 034003 (2009).

[63] S. Quaglioni and P. Navrátil, Phys. Rev. Lett. **101**, 092501 (2008).

[64] S. Quaglioni and P. Navrátil, Phys. Rev. C **79**, 044606 (2009).

[65] P. Navrátil, S. Quaglioni, I. Stetcu and B. R. Barrett, J. Phys. G **36**, 083101 (2009).

[66] P. Navrátil and S. Quaglioni, Phys. Rev. Lett. **108**, 042503 (2012).

[67] S. Baroni, P. Navrátil and S. Quaglioni, Phys. Rev. Lett. **110**, no. 2, 022505 (2013).

[68] S. Baroni, P. Navrátil and S. Quaglioni, Phys. Rev. C **87**, no. 3, 034326 (2013).

[69] P. Navrátil, S. Quaglioni, G. Hupin, C. Romero-Redondo and A. Calci, Phys. Scripta **91**, no. 5, 053002 (2016).

[70] G. Hagen, T. Papenbrock and M. Hjorth-Jensen, Phys. Rev. Lett. **104**, 182501 (2010).

[71] G. Hagen, M. Hjorth-Jensen, G. R. Jansen, R. Machleidt and T. Papenbrock, Phys. Rev. Lett. **108**, 242501 (2012).

[72] G. Hagen and N. Michel, Phys. Rev. C **86**, 021602 (2012).

[73] G. Papadimitriou, A. T. Kruppa, N. Michel, W. Nazarewicz, M. Płoszajczak and J. Rotureau, Phys. Rev. C **84**, 051304 (2011).

[74] G. Papadimitriou, J. Rotureau, N. Michel, M. Płoszajczak and B. R. Barrett, Phys. Rev. C **88**, no. 4, 044318 (2013).

[75] B. R. Barrett, G. Papadimitriou, N. Michel and M. Płoszajczak, arXiv:1508.07529.

[76] J.M. Bang, A.I. Mazur, A.M. Shirokov, Yu.F. Smirnov, S.A. Zaytsev, Ann. Phys. (N.Y.) **280**, 299 (2000).

[77] A. M. Shirokov, A. I. Mazur, I. A. Mazur and J. P. Vary, Phys. Rev. C **94**, no. 6, 064320 (2016).

[78] A. M. Shirokov, G. Papadimitriou, A. I. Mazur, I. A. Mazur, R. Roth and J. P. Vary, Phys. Rev. Lett. **117**, 182502 (2016).

[79] K. Kravvaris and A. Volya, Phys. Rev. Lett. **119**, no. 6, 062501 (2017).

[80] J. E. Lynn, I. Tews, J. Carlson, S. Gandolfi, A. Gezerlis, K. E. Schmidt and A. Schwenk, Phys. Rev. Lett. **116**, no. 6, 062501 (2016).

[81] K. M. Nollett, S. C. Pieper, R. B. Wiringa, J. Carlson and G. M. Hale, Phys. Rev. Lett. **99**, 022502 (2007).

[82] G. Rupak and D. Lee, Phys. Rev. Lett. **111**, no. 3, 032502 (2013).

[83] S. Elhatisari, D. Lee, G. Rupak, E. Epelbaum, H. Krebs, T. A. Lähde, T. Luu and U. G. Meiner, Nature **528**, 111 (2015).

[84] J. P. Vary *et al.*, Phys. Rev. C **81**, 035205 (2010).

[85] X. Zhao, A. Ilderton, P. Maris and J. P. Vary, Phys. Rev. D **88**, 065014 (2013).

[86] X. Zhao, A. Ilderton, P. Maris and J. P. Vary, Proceedings of International Conference Nuclear Theory in the Supercomputing Era 2013 (NTSE-2013), Ames, IA, USA, May 1317, 2013. Eds. A. M. Shirokov and A. I. Mazur. Pacific National University, Khabarovsk, Russia, 2014, p. 204.

[87] G. Chen, X. Zhao, Y. Li, K. Tuchin and J. P. Vary, Phys. Rev. D **95**, no. 9, 096012 (2017).

[88] K. Alder, A. Bohr, T. Huus, B. Mottelson and A. Winther, Rev. Mod. Phys. **28**, 432 (1956).

[89] A. Winther and K. Alder, Nucl. Phys. A **319**, 518 (1979).

[90] J. M. Eisenberg and W. Greiner, *Nuclear Theory: Nuclear Models, 3rd. ed.* North-Holland, 1987, p. 584.

[91] A. Askar and A. S. Cakmak, J. Chem. Phys. **68**, 2794 (1978).

[92] T. Iitaka, Phys. Rev. E **49**, 4684 (1994).

[93] A. Bohr and B. Mottelson, *Nuclear Structure*, Vol. 1, World Scientific Publishing Co. Pte. Ltd, 1998, p. 92.

[94] J. M. Eisenberg and W. Greiner, *Nuclear Theory: Excitation Mechanisms of the Nucleus, 3rd. ed.* North-Holland, 1988, p. 235.

[95] J. Suhonen, *From Nucleons to Nucleus: Concepts of Microscopic Nuclear Theory* Springer-Verlag Berlin Heidelberg, 2007.

[96] Condon, E. U. and Shortley, G. The Theory of Atomic Spectra. Cambridge, England: Cambridge University Press, 1951.

[97] A. M. Shirokov, A. I. Mazur, S. A. Zaytsev, J. P. Vary and T. A. Weber, Phys. Rev. C **70**, 044005 (2004).

[98] A. M. Shirokov, J. P. Vary, A. I. Mazur, S. A. Zaytsev and T. A. Weber, Phys. Lett. B **621**, 96 (2005).

[99] A. M. Shirokov, J. P. Vary, A. I. Mazur and T. A.Weber, Phys. Lett. B **644**, 33 (2007).

[100] J. Martorell, D. W. L. Sprung and D. C. Zheng, Phys. Rev. C **51**, 1127 (1995).

[101] A. Huber, T. Udem, B. Gross, J. Reichert, M. Kourogi, K. Pachucki, M. Weitz and T. W. Hansch, Phys. Rev. Lett. **80**, 468 (1998).

[102] J. L. Forest, V. R. Pandharipande, S. C. Pieper, R. B. Wiringa, R. Schiavilla and A. Arriaga, Phys. Rev. C **54**, 646 (1996).

[103] M. Garçon, J.W. Van Orden, *The Deuteron: Structure and Form Factors. In: Negele J.W., Vogt E.W. (eds) Advances in Nuclear Physics. Advances in the Physics of Particles and Nuclei*, Vol. 26, Springer, Boston, MA, (2001).

[104] J. M. Eisenberg and W. Greiner, *Nuclear Models: Collective and Single-Particle Phenomena, 3rd. ed.* North-Holland, 1987, p. 44.

[105] O. Hen, G. A. Miller, E. Piasetzky and L. B. Weinstein, Rev. Mod. Phys. **89**, no. 4, 045002 (2017).

[106] J. J. Aubert *et al.* [European Muon Collaboration], Phys. Lett. **123B**, 275 (1983).

[107] H. Cheng and T. Wu, *Expanding Protons: Scattering at High Energies* (MIT Press, Cambridge, 1987).

[108] H. Honkanen, P. Maris, J. P. Vary and S. J. Brodsky, Phys. Rev. Lett. **106**, 061603 (2011).

[109] X. Zhao, H. Honkanen, P. Maris, J. P. Vary and S. J. Brodsky, Phys. Lett. B **737**, 65 (2014).

[110] P. Wiecki, Y. Li, X. Zhao, P. Maris and J. P. Vary, Phys. Rev. D **91**, no. 10, 105009 (2015).

[111] J. P. Vary *et al.*, Few Body Syst. **59**, no. 4, 56 (2018).

[112] Y. Li, P. Maris, X. Zhao and J. P. Vary, Phys. Lett. B **758**, 118 (2016).

[113] Y. Li, P. Maris and J. P. Vary, Phys. Rev. D **96**, no. 1, 016022 (2017).

[114] S. Tang, Y. Li, P. Maris and J. P. Vary, Phys. Rev. D **98**, no. 11, 114038 (2018).

[115] M. Li, Y. Li, P. Maris and J. P. Vary, Phys. Rev. D **98**, no. 3, 034024 (2018).

[116] S. Jia and J. P. Vary, Phys. Rev. C **99**, no. 3, 035206 (2019).

[117] J. Lan, C. Mondal, S. Jia, X. Zhao and J. P. Vary, Phys. Rev. Lett. **122**, no. 17, 172001 (2019).

[118] X. Zhao, A. Ilderton, P. Maris and J. P. Vary, Phys. Lett. B **726**, 856 (2013).

[119] P. A. M. Dirac, Rev. Mod. Phys. **21**, 392 (1949).

[120] P. A. M. Dirac, Can. J. Math. **2**, 129 (1950).

[121] A. Harindranath, Saha Institute of Nuclear Physics, 2005 (unpublished).

[122] S. J. Brodsky, H. C. Pauli and S. S. Pinsky, Phys. Rept. **301**, 299 (1998).

[123] J. R. Hiller, Prog. Part. Nucl. Phys. **90**, 75 (2016).

[124] G. A. Miller, Phys. Rev. C **56**, 2789 (1997).

[125] G. A. Miller, Prog. Part. Nucl. Phys. **45**, 83 (2000).

[126] P. Chang and F. Gursey, Phys. Rev. **164**, 1752 (1967).

[127] S. Weinberg, Phys. Rev. Lett. **17**, 616 (1966).

[128] Y. Tomozawa, Nuovo Cim. A **46**, 707 (1966).

[129] K. Hornbostel, S. J. Brodsky and H. C. Pauli, Phys. Rev. D **41**, 3814 (1990).

[130] S. A. Coon, M. I. Avetian, M. K. G. Kruse, U. van Kolck, P. Maris and J. P. Vary, Phys. Rev. C **86**, 054002 (2012).

[131] R. J. Furnstahl, G. Hagen and T. Papenbrock, Phys. Rev. C **86**, 031301 (2012).

[132] M. A. Caprio, P. Maris and J. P. Vary, Phys. Rev. C **86**, 034312 (2012).

[133] H. J. Lipkin, Phys. Rev. **109**, 2071 (1958).

[134] D. H. Gloeckner and R. D. Lawson, Phys. Lett. **53B**, 313 (1974).

[135] P. Maris, P. Wiecki, Y. Li, X. Zhao and J. P. Vary, Acta Phys. Polon. Supp. **6**, 321 (2013).

[136] S. J. Brodsky, D. S. Hwang, B. Q. Ma and I. Schmidt, Nucl. Phys. B **593**, 311 (2001).

[137] J. Carbonell, B. Desplanques, V. A. Karmanov and J. F. Mathiot, Phys. Rept. **300**, 215 (1998).

[138] Y. Li, P. Maris and J. Vary, Phys. Rev. D **97**, no. 5, 054034 (2018).

[139] M. Li, Y. Li, P. Maris and J. P. Vary, Phys. Rev. D **100**, no. 3, 036006 (2019).

[140] J. R. Hiller and S. J. Brodsky, Phys. Rev. D **59**, 016006 (1999).

[141] V. A. Karmanov, J.-F. Mathiot and A. V. Smirnov, Phys. Rev. D **77**, 085028 (2008).

[142] V. A. Karmanov, J.-F. Mathiot and A. V. Smirnov, Phys. Rev. D **82**, 056010 (2010).

[143] V. A. Karmanov, J. F. Mathiot and A. V. Smirnov, Phys. Rev. D **86**, 085006 (2012).

[144] J. M. Alarcón, D. W. Higinbotham, C. Weiss and Z. Ye, Phys. Rev. C **99**, no. 4, 044303 (2019).

[145] C. A. Aidala *et al.* [SeaQuest Collaboration], arXiv:1706.09990 [physics.ins-det].

[146] R. S. Towell *et al.* [NuSea Collaboration], Phys. Rev. D **64**, 052002 (2001).

[147] E. A. Hawker *et al.* [NuSea Collaboration], Phys. Rev. Lett. **80**, 3715 (1998).

[148] M. Alberg and G. A. Miller, arXiv:1712.05814 [nucl-th].

[149] J. Arrington, W. Melnitchouk and J. A. Tjon, Phys. Rev. C **76**, 035205 (2007).

[150] G. A. Miller, Phys. Rev. C **99**, no. 3, 035202 (2019).

[151] C. F. Perdrisat, V. Punjabi and M. Vanderhaeghen, Prog. Part. Nucl. Phys. **59**, 694 (2007).

[152] G. A. Miller, Phys. Rev. C **66**, 032201 (2002).

[153] I. C. Cloët and G. A. Miller, Phys. Rev. C **86**, 015208 (2012).

[154] L. Ou , Z. Xiao, H. Yi, N. Wang, M. Liu, and J. Tian, Phys. Rev. Lett. **115**, 212501 (2015).

[155] V. Baryshevsky, and A. Rouba, Phys. Lett. B **683**, 299 (2010).

[156] H. Seyfarth, R. Engels, F. Rathmann, H. Ströher, V. Baryshevsky, A. Rouba, C. Düweke, R. Emmerich, A. Imig, K. Grigoryev, M. Mikirtychiants, and A. Vasilyev, Phys. Rev. Lett. **104**, 222501 (2010).

[157] C. A. Bertulani and L. F. Canto, Nucl. Phys. **A539**, 163 (1992).

[158] L. F. Canto, R. Donangelo, A. Romanelli, M. S. Hussein, and A. F. R. de Toledo Piza, Phys. Rev. C **55**, R570(R) (1997).

[159] N. Austern, Y. Iseri, M. Kamimura, M. Kawai, G. Rawitscher and M. Yahiro, Phys. Rept. **154**, 125 (1987).

[160] E. Epelbaum, H. W. Hammer and U. G. Meissner, Rev. Mod. Phys. **81**, 1773 (2009).

[161] J. M. Eisenberg and W. Greiner, *Nuclear Theory: Microscopic Theory of the Nucleus, 1st. ed.* North-Holland, 1976, p. 62.

[162] Eite Tiesinga, Peter J. Mohr, David B. Newell, and Barry N. Taylor (2019), "The 2018 CODATA Recommended Values of the Fundamental Physical Constants" (Web Version 8.0). Database developed by J. Baker, M. Douma, and S. Kotochigova. Available at http://physics.nist.gov/constants, National Institute of Standards and Technology, Gaithersburg, MD 20899.

[163] Yang Li, Paul W. Wiecki, Xingbo Zhao, Pieter Maris and James P. Vary, Proceedings of International Conference 'Nuclear Theory in the Supercomputing Era 2013 (NTSE-2013), Ames, IA, USA, May 1317, 2013. Eds. A. M. Shirokov and A. I. Mazur. Pacific National University, Khabarovsk, Russia, 2014, p. 136.

APPENDIX A. 3DHO BASIS AND OPERATORS

For the NN system, we introduce the 3DHO basis in the relative coordinate as

$$\langle \vec{r}\,|nlSJMTt_z\rangle \;=\; \sum_{m_l,m_s} (lm_lSm_s|JM)R_{nl}(r)Y_{lm_l}(\hat{r})\chi_{Sm_s}\chi_{Tt_z}\;, \tag{A.1}$$

where n is the radial quantum number, l is the quantum number of the orbital angular momentum $\vec{l}$. S is the quantum number for the total spin $\vec{s}$ of the NN system. m_l and m_s are the z-components of $\vec{l}$ and $\vec{S}$, respectively. The total angular momentum $\vec{J}$ is coupled by the LS scheme with M being the z-component. t_z is the z-component of isospin T. $Y_{lm_l}(\hat{r})$ denotes the spherical harmonics and $(lm_lSm_s|JM)$ is the CG-coefficient (both following the Condon-Shortley convention [95, 96]). χ_{Sm_s} and χ_{Tt_z} are, respectively, the spin and isospin parts of the wave function. We include χ_{Tt_z} in our definition of the 3DHO basis for the convenience in evaluating the weak operators. As for the rest of the operators in this thesis that do not operate on the isospin degree of freedom, χ_{Tt_z} can be omitted whenever there is no risk of confusion. $R_{nl}(r)$ is the radial part of 3DHO wave function

$$R_{nl}(r) \;=\; \sqrt{\frac{2n!}{r_0^3\Gamma(n+l+\frac{3}{2})}}\left(\frac{r}{r_0}\right)^l \exp\Big[-\frac{r^2}{2r_0^2}\Big]\; L_n^{l+\frac{1}{2}}\Big(\frac{r^2}{r_0^2}\Big)\;, \tag{A.2}$$

where r denotes the separation between the two nucleons in the relative coordinates. $\Gamma(n+l+3/2)$ is the Gamma function. $L_n^{l+\frac{1}{2}}(r^2/r_0^2)$ is the associated Laguerre polynomial. Since we work in the relative coordinates, the length scale of the 3DHO basis [Eq. (2.4)] becomes

$$r_0 = \sqrt{\frac{1}{M_{\rm red}\Omega}}, \tag{A.3}$$

where $M_{\rm red} = M_N/2 = 469.46$ MeV is the reduced mass for the NN system, while Ω is the oscillator strength.

The normalization condition for the 3DHO basis Eq. (A.1) is

$$\langle nlSJMTt_z|n'l'S'J'M'T't_z'\rangle = \delta_{n,n'}\delta_{l,l'}\delta_{S,S'}\delta_{J,J'}\delta_{M,M'}\delta_{T,T'}\delta_{t_z,t_z'}\;. \tag{A.4}$$

The matrix element of the operator O in the 3DHO representation, $\langle nlSJMTt_z|O|n'l'S'J'M'T't'_z\rangle$, is computed analytically in the coordinate space. The results for the operators that are relevant to this work are shown in the following.

A.1 r^2

The matrix element for the operator r^2 is

$$\begin{aligned}&\langle nlSJMTt_z|r^2|n'l'S'J'M'T't'_z\rangle \\ =&r_0^2\ \delta_{ll'}\delta_{SS'}\delta_{JJ'}\delta_{MM'}\delta_{TT'}\delta_{t_zt'_z}\times\begin{cases}(2n+l+\frac{3}{2}) & \text{for } n=n' \\ -\sqrt{(n+l+\frac{3}{2})(n+1)} & \text{for } n=n'-1 \\ -\sqrt{(n'+l+\frac{3}{2})(n'+1)} & \text{for } n=n'+1 \\ 0 & \text{else}\end{cases}.\end{aligned} \tag{A.5}$$

The rms point-proton charge radius of the NN system is evaluated as $\frac{1}{2}\sqrt{\langle r^2\rangle}$ in this work.

A.2 p^2

The matrix element of the operator p^2 is

$$\begin{aligned}&\langle nlSJMTt_z|p^2|n'l'S'J'M'T't'_z\rangle \\ =&p_0^2\ \delta_{ll'}\delta_{SS'}\delta_{JJ'}\delta_{MM'}\delta_{TT'}\delta_{t_zt'_z}\times\begin{cases}2n+l+\frac{3}{2} & \text{for } n=n' \\ \sqrt{(n+l+\frac{3}{2})(n+1)} & \text{for } n=n'-1 \\ \sqrt{(n'+l'+\frac{3}{2})(n'+1)} & \text{for } n=n'+1 \\ 0 & \text{else}\end{cases},\end{aligned} \tag{A.6}$$

where $p_0=\sqrt{M_{\rm red}\Omega}$ is the oscillator momentum.

A.3 L^2

The matrix element of the operator L^2 is

$$\langle nlSJMTt_z|L^2|n'l'S'J'M'T't'_z\rangle \ = \ l(l+1)\ \delta_{nn'}\delta_{ll'}\delta_{SS'}\delta_{JJ'}\delta_{MM'}\delta_{TT'}\delta_{t_zt'_z}\ . \tag{A.7}$$

A.4 J_z

The matrix element for the operator J_z, the $\hat{z}$-projection of the total angular momentum, is

$$\langle nlSJMTt_z|J_z|n'l'S'J'M'Tt'_z\rangle \;=\; M\;\delta_{nn'}\delta_{ll'}\delta_{SS'}\delta_{JJ'}\delta_{MM'}\delta_{TT'}\delta_{t_zt'_z}\;. \tag{A.8}$$

A.5 $rY_{1\mu}(\hat{r})$

The matrix element of the operator $rY_{1\mu}(\hat{r})$ in the 3DHO representation is

$$\begin{aligned}
&\langle nlSJMTt_z|rY_{1\mu}(\hat{r})|n'l'S'J'M'T't'_z\rangle \\
=&\delta_{TT'}\delta_{t_zt'_z}\int R^*_{nl}(r)rR_{n'l'}(r)r^2dr \\
&\times\sum_{m_lm_s}\sum_{m_{l'}m_{s'}}\delta_{SS'}\delta_{m_sm_{s'}}(lm_lSm_s|JM)(l'm_{l'}S'm_{s'}|J'M') \\
&\times(-1)^{m_l}\sqrt{\frac{3(2l+1)(2l'+1)}{4\pi}}\begin{pmatrix} l & 1 & l' \\ -m_l & \mu & m_{l'}\end{pmatrix}\begin{pmatrix} l & 1 & l' \\ 0 & 0 & 0\end{pmatrix}\quad.
\end{aligned} \tag{A.9}$$

In our calculation, we adopt the $3j$-symbols, e.g.,

$$\begin{pmatrix} l & 1 & l' \\ -m_l & \mu & m_{l'}\end{pmatrix}$$

following the Condon-Shortley convention [95, 96]. The radial integral in Eq. (A.9) can be computed as

$$\int R^*_{nl}(r)rR_{n'l'}(r)r^2dr \;=\; r_0\begin{cases}\sqrt{n+l+\frac{3}{2}}\;\delta_{n,n'}-\sqrt{n}\delta_{n,n'+1} & \text{for } l'=l+1\\ \sqrt{n'+l'+\frac{3}{2}}\;\delta_{n,n'}-\sqrt{n'}\delta_{n',n+1} & \text{for } l=l'+1\\ 0 & \text{else}\end{cases}\;. \tag{A.10}$$

A.6 $r^2Y_{2\sigma}(\hat{r})$

The matrix element of the operator $r^2Y_{2\sigma}(\hat{r})$ in 3DHO representation is

$$
\begin{aligned}
&\langle nlSJMTt_z|r^2\ Y_{2\sigma}(\hat{r})|n'l'S'J'M'T't'_z\rangle \\
=&r_0^2\sqrt{\frac{3ll'(l+1)(l'+1)}{2\pi}}\delta_{TT'}\delta_{t_zt'_z}\delta_{SS'}\mathscr{R}(n,l;n',l') \\
&\times\sum_{m_lm_s}\sum_{m'_lm'_s}\delta_{m_sm'_s}(lm_lSm_s|JM)(l'm'_lS'm'_s|J'M')(-1)^{m_l}\begin{pmatrix} l & 2 & l' \\ -m_l & \sigma & m'_l\end{pmatrix}\begin{pmatrix} l & 2 & l' \\ 0 & 0 & 0\end{pmatrix}\ ,
\end{aligned}
$$

where the radial part of the integration is

$$
\begin{aligned}
&\mathscr{R}(n,l;n',l') \\
=&\left[(2n+l+\frac{3}{2})\delta_{nn'}-\sqrt{(n+l+\frac{3}{2})(n+1)}\delta_{n,n'-1}-\sqrt{(n'+l+\frac{3}{2})(n'+1)}\delta_{n,n'+1}\right]\delta_{l,l'} \\
&+\left[\sqrt{(n'+l+\frac{3}{2})(n'+l+\frac{5}{2})}\delta_{nn'}-2\sqrt{(n'+1)(n'+l+\frac{5}{2})}\delta_{n,n'+1}+\sqrt{(n'+1)(n'+2)}\delta_{n,n'+2}\right]\delta_{l',l+2} \\
&+\left[\sqrt{(n+l'+\frac{3}{2})(n+l'+\frac{5}{2})}\delta_{nn'}-2\sqrt{(n+1)(n+l'+\frac{5}{2})}\delta_{n',n+1}+\sqrt{(n+1)(n+2)}\delta_{n',n+2}\right]\delta_{l,l'+2}
\end{aligned}
\tag{A.11}
$$

The E2 operator can be used to calculate the quadrupole moment (see, e.g., [95, 96]) as

$$
Q(\alpha,J) \quad = \quad \sqrt{\frac{16\pi}{5}}\langle\ \alpha J,M=J|\Big(\frac{r}{2}\Big)^2\ Y_{20}(\hat{r})|\ \alpha J,M=J\rangle\ , \tag{A.12}
$$

where α denotes all the other quantum numbers necessary to specify the state of the NN system.

A.7 Operator of the static magnetic dipole moment

The magnetic dipole ($M1$) operator for the NN system can be found in textbooks[1] (see, e.g., [93, 161]). Since we only calculate the static magnetic dipole moment of the deuteron system ($S=1$, $J=1$, $T=0$ and $t_z=0$), we adopt a simplified form of the operator μ_{10} (e.g., [161]). The

[1]Note that these definitions does not count the mesonic degree of freedom.

corresponding matrix element in 3DHO representation is

$$\begin{aligned}&\langle nlSJMTt_z|\mu_{10}|n'l'SJMTt_z\rangle\\ =&\delta_{nn'}\delta_{ll'}\Big\{(K_p+K_n)M+(K_p+K_n-\frac{1}{2})\Big[\sum_{m_l,m_s} m_l(lm_lSm_s|JM)(l'm_lSm_s|JM)\Big]\Big\}\ . \end{aligned} \tag{A.13}$$

In the unit of nuclear magneton μ_N, the proton magnetic moment K_p and neutron magnetic moment K_n are [162]

$$K_p = 2.7928473508(85)\ , \tag{A.14}$$

$$K_n = -1.91304273(45)\ . \tag{A.15}$$

The dipole moment of the deuteron is calculated as [95, 96]

$$\mu(\alpha,J) = \langle \alpha J, M=J|\mu_{10}|\alpha J, M=J\rangle\ . \tag{A.16}$$

A.8 Allowed Gammow-Teller operator

In the 3DHO representation, the one-body operator for the allowed Gammow-Teller (GT) transition of the NN system [93] is

$$\langle nlSJMTt_z\Big|M_{1\sigma}\Big|n'l'S'J'M'T't'_z\rangle, \tag{A.17}$$

where the one-body operator $M_{1\sigma}$ is [93]

$$M_{1\mu} = \frac{g_A}{\sqrt{4\pi}}\sum_{k=1}^{2} t_+(k)\sigma_\mu(k)\ , \tag{A.18}$$

with $g_A = 1.25$ being the axial coupling constant [93]. The summation is over all the nucleons (labled by k). $t_+(k)$ is the rising operator acting on the isospinors as $t_+|n\rangle = |p\rangle$ and $t_+|p\rangle = 0$. σ_μ (with $\mu = 0, \pm 1$) is the covariant spherical component of the Pauli operator. The corresponding matrix element is

$$\begin{aligned}&\langle nlSJMTt_z\Big|M_{1\mu}\Big|n'l'S'J'M'T't'_z\rangle\\ =&\frac{g_A}{\sqrt{4\pi}}\delta_{nn'}\delta_{ll'}\sum_{m_lm_s}\sum_{m'_lm'_s}\delta_{m_lm'_l}(lm_lSm_s|JM)(l'm'_lS'm'_s|J'M')\langle Sm_sTt_z\Big|\sum_{k=1}^{2}t_+(k)\sigma_\mu(k)\Big|S'm'_sT't'_z\rangle\ . \end{aligned} \tag{A.19}$$

A.9 $0\nu2\beta$ decay

In this work, we evaluate the $0\nu2\beta$ decay up to the NLO in the framework of the chiral effective field theory. In 3DHO representation, the matrix element of the $0\nu2\beta$ operator is

$$\left\langle nlSJMTt_z|M_{0\nu\beta\beta}\right|\, n'l'S'J'M'T't'_z\big\rangle\ , \tag{A.20}$$

where the expression of the $M_{0\nu\beta\beta}$ is given by Eq. (54) in Ref. [53].

As a test problem for the application of the OLS procedure, we consider the transition from the ground state of a di-neutron system in the channel $(nn;\ ^1S_0)$ to the ground state of a di-proton system in the channel $(pp;\ ^1S_0)$, where the initial and final NN systems are both enclosed in a HO potential trap. The quantum numbers for the initial and final channels are $l = l' = 0$, $S = S' = 0$, $J = J' = 0$, $T = T' = 1$, $t_z = 1$, $t'_z = -1$. The corresponding matrix element is

$$\begin{aligned}&\big\langle \alpha_f n0001-1\big|M_{0\nu\beta\beta}\big|\alpha_i n'000011\big\rangle\\ &=-6\sqrt{\frac{2n!}{r_0^3\Gamma(n+\frac{3}{2})}}\sqrt{\frac{2n'!}{r_0^3\Gamma(n'+\frac{3}{2})}}\int r(M_\pi r-2)\exp\Big[-\frac{r^2}{r_0^2}-M_\pi r\Big]L_n^{\frac{1}{2}}\Big(\frac{r^2}{r_0^2}\Big)L_{n'}^{\frac{1}{2}}\Big(\frac{r^2}{r_0^2}\Big)dr\ ,\end{aligned} \tag{A.21}$$

where r is the separation between the two nucleons in initial/finial system. M_π is the mass of the charged pions. Note that the second term in Eq. (54) in Ref. [53] vanishes for the $0\nu2\beta$ decay between the spin-singlet initial and final states. In practice, we evaluate Eq. (A.21) numerically.

APPENDIX B. OKUBO-LEE-SUZUKI TRANSFORMATION

B.1 Non-Hermitian effective Hamiltonian

There is more than one way to construct effective Hamiltonians (and, consistently, other operators) via the Okubo-Lee-Suzuki (OLS) transformation. In the section, we present a formal theory for the OLS transformation. The interested reader is also referred to, e.g., Refs. [9, 33, 34, 35, 36]. These different methods are equivalent to within a residual unitary transformation that does not mix the $\mathcal{P}$ and $\mathcal{Q}$-spaces. This difference could be interesting when approximations are employed.

We start from the arbitrary Hamiltonian equation

$$H|k\rangle = E_k|k\rangle \ , \tag{B.1}$$

where H is the Hamiltonian, e.g., for a many-body system. We assume that H is Hermitian. $|k\rangle$ is the eigenvector corresponding to the eigenvalue E_k. The set $\{|k\rangle\}$ spans the the full basis space for the system.

We divide the full basis space into the $\mathcal{P}$-space and the complementary $\mathcal{Q}$-space. The projection operator for the $\mathcal{P}$- and $\mathcal{Q}$-spaces are, respectively,

$$P = \sum_{\alpha_P} |\alpha_P\rangle\langle\alpha_P| \ , \tag{B.2}$$

$$Q = \sum_{\alpha_Q} |\alpha_Q\rangle\langle\alpha_Q| \ , \tag{B.3}$$

where $\{|\alpha_P\rangle\}$ is the basis set of the $\mathcal{P}$-space of dimension d_P, while $\{|\alpha_Q\rangle\}$ is the basis set of the $\mathcal{Q}$-space of dimension d_Q. The following conditions hold for the projection operators

$$P^2 = P,\ Q^2 = Q, P + Q = \mathbb{1},\ PQ = QP = 0 \ , \tag{B.4}$$

where $\mathbb{1}$ is the identity operator of the full basis space.

The similarity transformation of the arbitrary Hamiltonian H and that of the corresponding eigenvector $|k\rangle$ [Eq. (B.1)] are defined as

$$H \longmapsto \widetilde{H} = e^{-\omega} H e^{\omega} \ , \tag{B.5}$$

$$|k\rangle \longmapsto |\widetilde{k}\rangle = e^{-\omega}|k\rangle \ , \tag{B.6}$$

where the the generator of the similarity transformation satisfies

$$\omega = Q\omega P. \tag{B.7}$$

The following conditions hold for ω

$$\omega^2 = 0 \ , \tag{B.8}$$

$$(\omega^\dagger)^2 = 0 \ , \tag{B.9}$$

$$e^{\omega} = 1 + \omega \ , \tag{B.10}$$

$$e^{-\omega} = 1 - \omega \ . \tag{B.11}$$

The transformed Hamiltonian equation is

$$\widetilde{H}|\widetilde{k}\rangle = E_k|\widetilde{k}\rangle \ , \tag{B.12}$$

or, in the matrix representation,

$$\begin{pmatrix} P\widetilde{H}P & P\widetilde{H}Q \\ Q\widetilde{H}P & Q\widetilde{H}Q \end{pmatrix} \begin{pmatrix} P|\widetilde{k}\rangle \\ Q|\widetilde{k}\rangle \end{pmatrix} = E_k \begin{pmatrix} P|\widetilde{k}\rangle \\ Q|\widetilde{k}\rangle \end{pmatrix} \ . \tag{B.13}$$

We can choose a set $\mathcal{K}$ that contains d_P eigenvectors of the Hamiltonian H, i.e.,

$$\mathcal{K} = \{|k\rangle\}, \ k = 1, 2, \cdots, d_P. \tag{B.14}$$

where d_P is the dimension of the space $\mathcal{P}$. We will construct the effective Hamiltonian that preserves the eigenvalues for the eigenvector in set $\mathcal{K}$. Based on Eqs. (B.6), (B.7) and (B.11), we require the following mapping conditions to hold for $|k\rangle \in \mathcal{K}$

$$P|\widetilde{k}\rangle = P|k\rangle \ , \tag{B.15}$$

$$Q|\widetilde{k}\rangle = 0 \ . \tag{B.16}$$

Assuming these state vectors in the set $\{P|\widetilde{k}\rangle\}$, with $k = 1, 2, \cdots, d_P$, are linearly independent, it follows from Eq. (B.15) and (B.16) that [50]

1. The generator of the similarity transformation ω satisfies

$$Q|k\rangle = \omega P|k\rangle \quad \text{for} \quad \forall |k\rangle \in \mathcal{K}. \tag{B.17}$$

2. The decoupling condition holds

$$Q\widetilde{H}P = 0 \ . \tag{B.18}$$

3. $P|\widetilde{k}\rangle$ is the eigenvectors of $P\widetilde{H}P$ with the eigenvalue E_k

$$P\widetilde{H}P \ P|\widetilde{k}\rangle = E_k P|\widetilde{k}\rangle, \ k = 1, 2, \cdots, d_P. \tag{B.19}$$

We remark that

1. The transformed Hamiltonian $\widetilde{H}$ is not Hermitian since $P\widetilde{H}Q$ does not necessarily vanish.

2. The effective Hamiltonian that preserves the spectrum for the set $\mathcal{K}$ is defined as

$$\widetilde{H}_{\text{eff}} \equiv P\widetilde{H}P \ . \tag{B.20}$$

3. ω can be solved from Eq. (B.17) as

$$\sum_{\alpha_Q \in \mathcal{Q}} \langle \alpha_Q | k \rangle = \sum_{\alpha_P \in \mathcal{P}} \langle \alpha_Q | \omega | \alpha_P \rangle \langle \alpha_P | k \rangle \ . \tag{B.21}$$

Assuming the $d_P \times d_P$ matrix of the element $\langle \alpha_P | k \rangle$ (with $|k\rangle \in \mathcal{K}$) is invertible, ω in terms of the basis sets $\{|\alpha_P\rangle\}$ and $\{|\alpha_Q\rangle\}$ is

$$\langle \alpha_Q | \omega | \alpha_P \rangle = \sum_{k \in \mathcal{K}} \langle \alpha_Q | k \rangle \langle \hat{k} | \alpha_P \rangle \ , \tag{B.22}$$

where $\langle \hat{k} | \alpha_P \rangle$ denotes the element of the inverse of the matrix with the element $\langle \alpha_P | k \rangle$, i.e.,

$$\sum_{\alpha_P \in \mathcal{P}} \langle \hat{k} | \alpha_P \rangle \langle \alpha_P | k' \rangle = \delta_{k,k'}, \ \forall k, k' \in \mathcal{K} \ . \tag{B.23}$$

B.2 Hermitian effective Hamiltonian

The Hermitian effective Hamiltonian can be obtained directly by a unitary transformation of the Hamiltonian H [35, 36]. We start with the arbitrary Hamiltonian equation [Eq. (B.1)]

$$H|k\rangle = E_k|k\rangle \ .$$

To proceed, we assume that H is Hermitian and that

$$\omega = Q\omega P \ . \tag{B.24}$$

Again, we choose d_P eigenvectors to form the set $\mathcal{K}$ and the following condition holds for these d_P eigenvectors

$$Q|k\rangle = \omega P|k\rangle, \ k = 1, 2, \cdots, d_P \ , \tag{B.25}$$

while the rest d_Q eigenvectors forms the set $\mathcal{S}$

$$\mathcal{S} = \{|k\rangle\}, \ k = d_P + 1, d_P + 2, \cdots, d_P + d_Q \ , \tag{B.26}$$

which is complementary to $\mathcal{K}$.

We define the left and right identity operators $Pe^{\omega^\dagger}$ and $e^{\omega}P$ for the eigenvectors in set $\mathcal{K}$

$$Pe^{\omega^\dagger} = P(1 + \omega^\dagger), \ s.t. \ \langle k'| = \langle k'|Pe^{\omega^\dagger} \ , \tag{B.27}$$

$$e^{\omega}P = (1 + \omega)P, \ s.t. \ |k\rangle = e^{\omega}P|k\rangle \ , \tag{B.28}$$

with $k, \ k' \in \mathcal{K}$. Eq. (B.1) can be modified as

$$\langle k'|Pe^{\omega^\dagger}He^{\omega}P|k\rangle = E_k\langle k'|Pe^{\omega^\dagger}e^{\omega}P|k\rangle \ . \tag{B.29}$$

By applying the Hermitian metric

$$M = M^\dagger \equiv Pe^{\omega^\dagger}e^{\omega}P = P(1 + \omega^\dagger)(1 + \omega)P = P(1 + \omega^\dagger\omega)P \ , \tag{B.30}$$

on both sides of Eq. (B.29), we get

$$\langle \bar{k}'|e^{-S}He^{S}|\bar{k}\rangle = E_k\langle \bar{k}'|e^{-S}e^{S}|\bar{k}\rangle \ , \tag{B.31}$$

where we have defined the transformation e^S as

$$e^{-S} \equiv M^{-\frac{1}{2}} e^{\omega^\dagger} \ , \tag{B.32}$$

$$e^{S} \equiv e^{\omega} M^{-\frac{1}{2}} \ , \tag{B.33}$$

$$|\bar{k}\rangle \equiv e^{-S}|k\rangle \ , \tag{B.34}$$

$$\langle\bar{k}'| \equiv e^{S}\langle k'| \ . \tag{B.35}$$

The transformation for the Hamiltonian H is correspondingly

$$\bar{H} \equiv e^{-S} H e^{S} \ . \tag{B.36}$$

The formal solution of the generator $S(\omega)$ of the transformation is [35, 36]

$$S = \text{arctanh}(\omega - \omega^\dagger) \ . \tag{B.37}$$

It is straightforward to show that

$$S^\dagger = -S, \ e^{-S} = (e^S)^\dagger \ . \tag{B.38}$$

Hence $\bar{H}$ is Hermitian due to the unitary transformation e^S. It follows from Eq. (B.25) that the mapping conditions

$$P|\bar{k}\rangle = |k\rangle \ , \tag{B.39}$$

$$Q|\bar{k}\rangle = 0 \ , \tag{B.40}$$

hold for $k = 1, 2, \cdots, d_P$.

In the matrix representation, we have

$$\begin{pmatrix} P\bar{H}P & P\bar{H}Q \\ Q\bar{H}P & Q\bar{H}Q \end{pmatrix} \begin{pmatrix} P|\bar{k}\rangle \\ Q|\bar{k}\rangle \end{pmatrix} = E_k \begin{pmatrix} P|\bar{k}\rangle \\ Q|\bar{k}\rangle \end{pmatrix} \ . \tag{B.41}$$

It follows that

1. The *full* decoupling condition holds

$$Q\bar{H}P = P\bar{H}Q = 0. \tag{B.42}$$

2. The effective Hamiltonian in the $\mathcal{P}$-space

$$\bar{H}^P_{\text{eff}} \equiv P\bar{H}P \ , \tag{B.43}$$

reproduces the eigenvalue E_k of the eigenvector $|k\rangle \in \mathcal{K}$ as

$$\bar{H}^P_{\text{eff}} \ P|\bar{k}\rangle = E_k \ P|\bar{k}\rangle, \ \ k = 1, 2, \cdots, d_P, \tag{B.44}$$

with $P|\bar{k}\rangle$ being the eigenvectors of $\bar{H}^P_{\text{eff}}$.

3. The operator ω that can be solved from [Eq. (B.25)] in the form of Eq. (B.23).

4. Due to the *full* decoupling condition Eq. (B.42), the effective Hamiltonian in the $\mathcal{Q}$-space can be consistently defined as

$$\bar{H}^Q_{\text{eff}} \equiv Q\bar{H}Q \ , \tag{B.45}$$

which reproduces the eigenvalue of each eigenvector $|k\rangle \in \mathcal{S}$ as

$$\bar{H}^Q_{\text{eff}} \ Q|\bar{k}\rangle = E_k \ Q|\bar{k}\rangle, \ \ k = d_P + 1, d_P + 2, \cdots, d_P + d_Q \ . \tag{B.46}$$

5. The effective Hamiltonians in the $\mathcal{P}$- and $\mathcal{Q}$-spaces are Hermitian as

$$P\bar{H}P = P\bar{H}^\dagger P, \ \ Q\bar{H}Q = Q\bar{H}^\dagger Q \ . \tag{B.47}$$

B.2.1 Remarks

1. A formal solution for the *full* decoupling problem can be found in [36].

2. More discussions on the OLS transformation (e.g., mathematical conditions and possible pitfalls) are shown in Ref. [50].

3. The expression of $S(\omega)$ [Eq. (B.37)] can be solved in the following way

$$\begin{aligned}
\ln[e^S P] &= \ln[e^{\omega} M^{-\frac{1}{2}} P] \\
&= \ln[(1+\omega)P(1+\omega^\dagger\omega)^{-\frac{1}{2}}P] \\
&= \ln[(1+\omega-\omega^\dagger)P] - \frac{1}{2}\ln[(1+\omega-\omega^\dagger)(1-\omega+\omega^\dagger)P] \\
&= \ln[(1+\omega-\omega^\dagger)P] - \frac{1}{2}\ln[(1+\omega-\omega^\dagger)P] - \frac{1}{2}\ln[(1-\omega+\omega^\dagger)P] \\
&= \frac{1}{2}\ln[(1+\omega-\omega^\dagger)P] - \frac{1}{2}\ln[(1-\omega+\omega^\dagger)P] \\
&= \frac{1}{2}\ln\left[\frac{1+(\omega-\omega^\dagger)}{1-(\omega-\omega^+)}P\right] \\
&= \operatorname{arctanh}(\omega-\omega^\dagger)P \ , \qquad \text{(B.48)}
\end{aligned}$$

where from the 2nd to the 3rd line, we have applied the identities

$$\begin{aligned}
\omega^\dagger P =& P\omega^\dagger Q P = 0 \ , \\
\omega\omega =& Q\omega P Q\omega P = 0 \ , \\
\omega^\dagger\omega^\dagger =& 0 \ . \qquad \text{(B.49)}
\end{aligned}$$

One gets

$$\begin{aligned}
\ln[e^S P] &= \operatorname{arctanh}(\omega-\omega^\dagger)\ P \ , \\
\ln[e^S]\ P &= \operatorname{arctanh}(\omega-\omega^\dagger)\ P \ , \\
S\ P &= \operatorname{arctanh}(\omega-\omega^\dagger)\ P \ . \qquad \text{(B.50)}
\end{aligned}$$

Since the $\mathcal{P}$-space and hence its projector P can be chosen arbitrarily, we have

$$S(\omega) = \operatorname{arctanh}(\omega-\omega^\dagger) \ . \qquad \text{(B.51)}$$

4. When the bases of the $\mathcal{P}$- and $\mathcal{Q}$-spaces, i.e., $|\alpha_P\rangle$ and $|\alpha_Q\rangle$, are chosen to be the eigenbases of the Hamiltonian $|k\rangle$ ($k = 1, 2, \cdots, d_P, d_P+1, \cdots, d_P+d_Q$), the effective Hamiltonian $\bar{H}^P_{\text{eff}}$ admits the form of Eq. (2.14) (note the same form is adopted in Ref. [47]).

APPENDIX C. CONVENTION OF THE LF COORDINATES

The light-front (LF) variable is defined as

$$x^\mu \;=\; (x^+, x^-, x^\perp)\ , \tag{C.1}$$

where the "LF time" is $x^+ = x^0 + x^3$ and the longitudinal variable is $x^- = x^0 - x^3$. The transverse coordinates are $x^\perp \;\equiv\; x^\perp = (x^1, x^2)$.

The metric tensors are

$$g^{\mu\nu} = \begin{pmatrix} 0 & 2 & 0 & 0 \\ 2 & 0 & 0 & 0 \\ 0 & 0 & -1 & 0 \\ 0 & 0 & 0 & -1 \end{pmatrix},\ g_{\mu\nu} = \begin{pmatrix} 0 & \frac{1}{2} & 0 & 0 \\ \frac{1}{2} & 0 & 0 & 0 \\ 0 & 0 & -1 & 0 \\ 0 & 0 & 0 & -1 \end{pmatrix}\ . \tag{C.2}$$

The following is true

$$x^\pm = 2x_\mp\ . \tag{C.3}$$

In terms of the LF variables, the inner product is

$$x \cdot y = \frac{1}{2}x^+y^- + \frac{1}{2}x^-y^+ - x^\perp \cdot y^\perp\ . \tag{C.4}$$

The partial derivatives $\partial_\mu = \frac{\partial}{\partial x^\mu}$ are

$$\partial^+ = 2\partial_- \;=\; 2\frac{\partial}{\partial x^-},\ \partial^- = 2\partial_+ \;=\; 2\frac{\partial}{\partial x^+}\ . \tag{C.5}$$

where the LF time-derivative is $\partial_+ = \frac{\partial}{\partial x^+}$ and the derivative of the longitudinal variable is $\partial_- = \frac{\partial}{\partial x^-}$.

The dispersion relation is

$$k^- = \frac{(k^\perp)^2 + m^2}{k^+}\ . \tag{C.6}$$

In the the light-cone region (time-light region and the light-front), $k^0 \geq k^3$ and $k^- = k^0 - k^3 \geq 0$. This implies the longitudinal momentum to be semipositive definite $k^+ \geq 0$, in which

$$k^+ k^- = (k^\perp)^2 + m^2 \ \geq \ 0 \ . \tag{C.7}$$

k^+ vanishes only if $m = 0$ and $k^\perp = 0$.

We follow the convention in Ref. [121] for the gamma matrices

$$\gamma^0 = \beta = \begin{bmatrix} 0 & -i \\ i & 0 \end{bmatrix}, \ \gamma^3 = \begin{bmatrix} 0 & i \\ i & 0 \end{bmatrix}, \ \gamma^1 = \begin{bmatrix} -i\sigma^2 & 0 \\ 0 & i\sigma^2 \end{bmatrix}, \ \gamma^2 = \begin{bmatrix} i\sigma^1 & 0 \\ 0 & -i\sigma^1 \end{bmatrix}, \ \gamma^5 = \begin{bmatrix} \sigma^3 & 0 \\ 0 & -\sigma^3 \end{bmatrix}, \tag{C.8}$$

where $\sigma = (\mathbb{1}, \vec{\sigma})$ are the standard Pauli matrices with

$$\sigma^0 = \begin{pmatrix} 1 & 0 \\ 0 & 1 \end{pmatrix}, \ \sigma^1 = \begin{pmatrix} 0 & 1 \\ 1 & 0 \end{pmatrix}, \ \sigma^2 = \begin{pmatrix} 0 & -i \\ i & 0 \end{pmatrix}, \ \sigma^3 = \begin{pmatrix} 1 & 0 \\ 0 & -1 \end{pmatrix} \ . \tag{C.9}$$

Then we have

$$\gamma^+ = \gamma^0 + \gamma^3 = \begin{bmatrix} 0 & 0 \\ 2i & 0 \end{bmatrix}, \ \gamma^- = \gamma^0 - \gamma^3 = \begin{bmatrix} 0 & -2i \\ 0 & 0 \end{bmatrix}. \tag{C.10}$$

The definition of the alpha matrices are

$$\vec{\alpha} \ = \ \gamma^0 \vec{\gamma} \ . \tag{C.11}$$

We have

$$\alpha^1 = \begin{bmatrix} 0 & \sigma^2 \\ \sigma^2 & 0 \end{bmatrix}, \ \alpha^2 = \begin{bmatrix} 0 & -\sigma^1 \\ -\sigma^1 & 0 \end{bmatrix}, \ \alpha^3 = \begin{bmatrix} 1 & 0 \\ 0 & -1 \end{bmatrix}. \tag{C.12}$$

The projection operators are defined as

$$\Lambda^+ = \begin{bmatrix} 1 & 0 \\ 0 & 0 \end{bmatrix}, \ \Lambda^- = \begin{bmatrix} 0 & 0 \\ 0 & 1 \end{bmatrix}, \tag{C.13}$$

with

$$\Lambda^+ + \Lambda^- = \mathbb{1}, \ (\Lambda^\pm)^2 = \Lambda^\pm, \ (\Lambda^\pm)^\dagger = \Lambda^\pm. \tag{C.14}$$

The following identities hold for the projection operators

$$\Lambda^{\pm} = \frac{1}{4}\gamma^{\mp}\gamma^{\pm} = \frac{1}{2}\gamma^{0}\gamma^{\pm} = \frac{1}{2}(\mathbb{1} \pm \alpha^{3}), \tag{C.15}$$

$$\gamma^{\mp} = 2\Lambda^{\pm}\gamma^{0} = \gamma^{\mp}\Lambda^{\mp}, \tag{C.16}$$

$$[\gamma^{\perp}, \Lambda^{\pm}] = [\gamma^{0}, \Lambda^{\pm}] = [\gamma^{5}, \Lambda^{\pm}] = 0, \tag{C.17}$$

$$\alpha^{\perp}\Lambda^{\pm} = \Lambda^{\mp}\alpha^{\perp}, \tag{C.18}$$

$$\gamma^{i}\Lambda^{\mp} = \frac{1}{2}\gamma^{i} \pm i\frac{1}{2}\epsilon^{ij}\gamma^{j}\gamma^{5} \ . \tag{C.19}$$

where the ϵ^{ij} is 2-dimensional Levi-Civita symbol.

APPENDIX D. 2DHO BASIS AND RELEVANT INTEGRALS

D.1 2DHO basis

The generating operator for the 2DHO basis can be expressed as [110]

$$P_+^\Omega = \frac{(p^\perp)^2}{2p^+} + \frac{1}{2}\Omega^2 p^+ (r^\perp)^2 \;=\; \frac{1}{2}\Omega\Big[\frac{(p^\perp)^2}{xP^+\Omega} + xP^+\Omega(r^\perp)^2\Big] \,, \tag{D.1}$$

where the oscillator energy Ω is related to the energy scale of the 2DHO basis set as

$$b = \sqrt{P^+\Omega} \,. \tag{D.2}$$

We refer to b as the basis strength.

For the convenience in evaluating integrals involving the 2DHO basis, one can further introduce the momentum fraction weighted variables [135] as

$$q^\perp \equiv \frac{p^\perp}{\sqrt{x}},\; s^\perp \equiv \sqrt{x} r^\perp \,, \tag{D.3}$$

where the canonical commutator $[s_i^\perp, q_j^\perp] = i\delta_{ij}$ $(i,j=1,2)$ holds. The generating operator of the 2DHO basis in terms of the conjugate variables $(s^\perp, q^\perp)$ can be rewritten as

$$P_+^\Omega = \frac{1}{2}\Omega\Big[\Big(\frac{q^\perp}{\sqrt{P^+\Omega}}\Big)^2 + \Big(\sqrt{P^+\Omega}s^\perp\Big)^2\Big] \,. \tag{D.4}$$

In the momentum representation, the 2DHO wave function is

$$\langle q^\perp | nm\rangle \;=\; \Psi_n^m(q^\perp) \;=\; \frac{1}{b}\sqrt{\frac{4\pi n!}{(n+|m|)!}}\rho^{|m|}\mathrm{e}^{-\frac{1}{2}\rho^2} L_n^{|m|}(\rho^2)\; e^{im\phi} \,, \tag{D.5}$$

where the transverse momentum in the complex representation is

$$q^\perp = b\rho\mathrm{e}^{i\phi} \,,\; (q^\perp)^* = b\rho\mathrm{e}^{-i\phi} \,, \tag{D.6}$$

with $\phi = \arg\, q^\perp$, $|q^\perp| = b\rho$. n, m are the quantum numbers for the radial part and angular part of the wave function, respectively. They define the eigenenergy of the corresponding 2DHO wave function

$$E_{nm} = (2n + |m| + 1)\Omega \,. \tag{D.7}$$

For completeness, we also present the 2DHO wave function in the coordinate representation:

$$\langle s^{\perp}|nm\rangle \;=\; \widetilde{\Psi}_n^m(s^{\perp}) \;=\; \underbrace{\mathrm{e}^{i\frac{\pi}{2}(2n+|m|)}}_{\text{phase}} \frac{1}{l}\sqrt{\frac{n!}{\pi(n+|m|)!}}\rho^{|m|}\mathrm{e}^{-\frac{1}{2}\rho^2}L_n^{|m|}(\rho^2)\; e^{im\theta}\;, \tag{D.8}$$

where, in the complex representation, the transverse position vector is

$$s^{\perp} = l\rho\mathrm{e}^{i\theta},\;\; \left(s^{\perp}\right)^* = l\rho\mathrm{e}^{-i\theta}\;, \tag{D.9}$$

with $\theta = \arg\, s^{\perp}$, $|s^{\perp}| = l\rho$ and $l = \frac{1}{b}$. The phase $\mathrm{e}^{i\frac{\pi}{2}(2n+|m|)}$ is fixed by the Fourier transformation:

$$\widetilde{\Psi}_n^m(s^{\perp}) = \int \frac{d^2q^{\perp}}{(2\pi)^2}\; \mathrm{e}^{iq^{\perp}\cdot s^{\perp}}\,\Psi_n^m(q^{\perp})\;, \tag{D.10}$$

$$\Psi_n^m(q^{\perp}) = \int d^2s^{\perp}\; \mathrm{e}^{-iq^{\perp}\cdot s^{\perp}}\,\widetilde{\Psi}_n^m(s^{\perp})\;, \tag{D.11}$$

with the conjugate variables $(s^{\perp}, q^{\perp})$.

The orthonormality relation of the 2DHO basis is

$$\langle nm|n'm'\rangle = \delta_{n,n'}\delta_{m,m'}\;. \tag{D.12}$$

D.2 Talmi-Moshinsky transformation

The Talmi-Moshinsky (TM) transformation of the 2DHO wave function [Eq. (D.5)] is defined via the following relation:

$$\Psi_{n_1}^{m_1}(q_1^{\perp})\Psi_{n_2}^{m_2}(q_2^{\perp}) = \sum_{NMnm} \mathcal{M}^{N,M,n,m}_{n_1,m_1,n_2,m_2}(x_1,x_2)\Psi_N^M(Q^{\perp})\Psi_n^m(q^{\perp})\;, \tag{D.13}$$

where the TM bracket is defined as

$$\mathcal{M}^{N,M,n,m}_{n_1,m_1,n_2,m_2}(x_1,x_2) = \mathcal{M}^{N,M,n,m}_{n_1,m_1,n_2,m_2}(\delta_{\mathrm{TM}}) \equiv \langle NMnm|n_1m_1n_2m_2\rangle\;, \tag{D.14}$$

with $2n_1 + |m_1| + 2n_2 + |m_2| = 2N + |M| + 2n + |m|$ and $m_1 + m_2 = M + m$. The phase δ_{TM} is given by $\tan\delta_{TM} = \sqrt{x_2/x_1}$. The analytic expression of the TM bracket can be found in Refs. [163, 110]. $q_1^{\perp}$ and $q_2^{\perp}$ are defined according to Eq. (D.3) as

$$q_1^{\perp} = \frac{p_1^{\perp}}{\sqrt{x_1}},\;\; q_2^{\perp} = \frac{p_2^{\perp}}{\sqrt{x_2}}\;. \tag{D.15}$$

The relative momentum $q^\perp$ and COM momentum $Q^\perp$ are, respectively,

$$q^\perp = \frac{\sqrt{x_2}q_1^\perp - \sqrt{x_1}q_2^\perp}{\sqrt{x_1+x_2}} \ , \tag{D.16}$$

$$Q^\perp = \frac{\sqrt{x_1}q_1^\perp + \sqrt{x_2}q_2^\perp}{\sqrt{x_1+x_2}} \ . \tag{D.17}$$

D.3 Some integrals involving the 2DHO basis

D.3.1 Identities

$$\mathcal{P}^{(k)}(n,m) = \int \frac{d^2q^\perp}{(2\pi)^2}\big(q^\perp\big)^k \Psi_n^m(q^\perp) = b^{k+1}(-1)^n 2^k \sqrt{\frac{(n+k)!}{\pi n!}}\delta_{k,-m} \ . \tag{D.18}$$

$$\mathcal{PC}^{(k)}(n,m) = \int \frac{d^2q^\perp}{(2\pi)^2}\Big[\Big(q^\perp\Big)^*\Big]^k \Psi_n^m(q^\perp) = b^{k+1}(-1)^n 2^k \sqrt{\frac{(n+k)!}{\pi n!}}\delta_{k,m} \ . \tag{D.19}$$

$$\begin{aligned}\mathcal{P}^{(1)}(n',m';n,m) =& \langle n'm'|q^\perp|nm\rangle \ = \ \langle n'm'|q^\perp|nm\rangle \\ =& b\ \delta_{m',m+1}\begin{cases} \sqrt{n+|m|+1}\delta_{n,n'} - \sqrt{n}\delta_{n,n'+1} \ , & m\geq 0,\ n\geq n' \\ \sqrt{n+|m|}\delta_{n,n'} - \sqrt{n+1}\delta_{n',n+1} \ , & m<0,\ n\leq n' \end{cases} \ .\end{aligned} \tag{D.20}$$

$$\begin{aligned}\mathcal{PC}^{(1)}(n',m';n,m) =& \langle n'm'|\big(q^\perp\big)^*|nm\rangle \ = \ \langle n'm'|\big(q^\perp\big)^*|nm\rangle \\ =& b\ \delta_{m,m'+1}\begin{cases} \sqrt{n'+|m'|+1}\delta_{n,n'} - \sqrt{n'}\delta_{n',n+1} \ , & m'\geq 0 \\ \sqrt{n'+|m'|}\delta_{n,n'} - \sqrt{n'+1}\delta_{n,n'+1} \ , & m'<0 \end{cases} \ .\end{aligned} \tag{D.21}$$

$$\begin{aligned}\langle n'm'|q^\perp(q^\perp)^*|nm\rangle \ =& \int \frac{d^2q^\perp}{(2\pi)^2}\Big(\Psi_{n'}^{m'}(q^\perp)\Big)^*|q^\perp|^2\Psi_n^m(q^\perp) \\ =& b^2\delta_{m',m}\Big[(2n+|m|+1)\delta_{n',n} - \sqrt{n'(n'+|m'|)}\delta_{n',n+1} - \sqrt{n(n+|m|)}\delta_{n,n'+1}\Big] \ .\end{aligned} \tag{D.22}$$

D.3.2 Shifted operator

The shifted operator, in the 2DHO representation, is defined as $\langle n', m'; u^\perp + q^\perp | n, m; u^\perp \rangle$, where the initial and final transverse momenta are $u^\perp$ and $u^\perp + q^\perp$, respectively. According to the translational invariance of the 2DHO basis function, it can be evaluated as

$$\langle n', m'; u^\perp + q^\perp | n, m; u^\perp \rangle = \langle n', m'; u^\perp + \frac{1}{2} q^\perp | n, m; u^\perp - \frac{1}{2} q^\perp \rangle \ . \tag{D.23}$$

Applying the 2DHO wave function in the complex momentum representation [Eq. (D.5)], the shifted operator reads

$$\begin{aligned} \int \frac{d^2 u^\perp}{(2\pi)^2} \Big(\Psi_{n'}^{m'}(u^\perp + q^\perp) \Big)^* \Psi_n^m(u^\perp) &= \int \frac{d^2 u^\perp}{(2\pi)^2} \Psi_{n'}^{m'*}\big(u^\perp + \frac{1}{2} q^\perp\big) \Psi_n^m\big(u^\perp - \frac{1}{2} q^\perp\big) \\ &= \sum_\nu \mathcal{M}^{N,0,\nu,\mu}_{n',-m',n,m}\Big(\frac{\pi}{4}\Big) \ \frac{b}{\sqrt{4\pi}} (-1)^N \Psi_\nu^\mu\Big(\frac{1}{\sqrt{2}} q^\perp\Big) \ , \end{aligned} \tag{D.24}$$

with

$$\mu = m - m', \tag{D.25}$$

$$N = n' + n - \nu + \frac{1}{2}\big(|m'| + |m| - |\mu|\big) \ , \tag{D.26}$$

$$0 \leq \nu \leq n + n' + \frac{1}{2}\big(|m'| + |m| - |\mu|\big) \ . \tag{D.27}$$

D.3.3 Integrals involving three 2DHO basis functions

$$\begin{aligned} &\int \frac{d^2 q_1^\perp}{(2\pi)^2} \frac{d^2 q_2^\perp}{(2\pi)^2} \frac{d^2 q'^\perp}{(2\pi)^2} (2\pi)^2 \delta^2(\sqrt{x_1} q_1^\perp + \sqrt{x_2} q_2^\perp - \sqrt{x'} q'^\perp) \ \Psi_{n_1}^{m_1}(q_1^\perp) \Psi_{n_2}^{m_2}(q_2^\perp) \Psi_{n'}^{m'*}(q'^\perp) \\ =&\delta_{m_1+m_2,m'} \ \frac{1}{x'} \ \mathcal{M}^{n',m',n,0}_{n_1,m_1,n_2,m_2}(x_1, x_2) \ \mathcal{P}^{(0)}(n, 0) \ , \end{aligned} \tag{D.28}$$

where $n = n_1 + n_2 - n' + \frac{1}{2}(|m_1| + |m_2| - |m_1 + m_2|) \geq 0$.

$$\begin{aligned} &\int \frac{d^2 q_1^\perp}{(2\pi)^2} \frac{d^2 q_2^\perp}{(2\pi)^2} \frac{d^2 q'^\perp}{(2\pi)^2} (2\pi)^2 \delta^2(\sqrt{x_1} q_1^\perp + \sqrt{x_2} q_2^\perp - \sqrt{x'} q'^\perp) \cdot q'^\perp \cdot \Psi_{n_1}^{m_1}(q_1^\perp) \Psi_{n_2}^{m_2}(q_2^\perp) \Psi_{n'}^{m'*}(q'^\perp) \\ =&\delta_{m_1+m_2,m'-1} \ \frac{1}{x'} \sum_{N=max[0,n'-1]}^{min[\nu,n'+1]} \mathcal{M}^{N,m'-1,\nu-N,0}_{n_1,m_1,n_2,m_2}(x_1, x_2) \ \mathcal{P}^{(1)}(n', m'; N, m'-1) \ \mathcal{P}^{(0)}(\nu - N, 0) \end{aligned} \tag{D.29}$$

where $\nu = N + n = n_1 + n_2 + \frac{1}{2}(|m_1| + |m_2| - |m_1 + m_2|)$.

$$\begin{aligned}
&\int \frac{d^2q_1^\perp}{(2\pi)^2}\frac{d^2q_2^\perp}{(2\pi)^2}\frac{d^2q'^\perp}{(2\pi)^2}(2\pi)^2\delta^2(\sqrt{x_1}q_1^\perp + \sqrt{x_2}q_2^\perp - \sqrt{x'}q'^\perp)\cdot(q'^\perp)^*\cdot\Psi_{n_1}^{m_1}(q_1^\perp)\Psi_{n_2}^{m_2}(q_2^\perp)\Psi_{n'}^{m'*}(q'^\perp)\\
=&\delta_{m_1+m_2,m'+1}\ \frac{1}{x'}\sum_{N=max[0,n'-1]}^{min[\nu,n'+1]}\mathcal{M}_{n_1,m_1,n_2,m_2}^{N,m'+1,\nu-N,0}(x_1,x_2)\ \mathcal{PC}^{(1)}(n',m';N,m'+1)\ \mathcal{P}^{(0)}(\nu-N,0)\ ,
\end{aligned} \tag{D.30}$$

where $\nu = N + n = n_1 + n_2 + \frac{1}{2}(|m_1| + |m_2| - |m' + 1|)$.

$$\begin{aligned}
&\int \frac{d^2q_1^\perp}{(2\pi)^2}\frac{d^2q_2^\perp}{(2\pi)^2}\frac{d^2q'^\perp}{(2\pi)^2}(2\pi)^2\delta^2(\sqrt{x_1}q_1^\perp + \sqrt{x_2}q_2^\perp - \sqrt{x'}q'^\perp)\cdot q_1^\perp\cdot\Psi_{n_1}^{m_1}(q_1^\perp)\Psi_{n_2}^{m_2}(q_2^\perp)\Psi_{n'}^{m'*}(q'^\perp)\\
=&\Bigg\{\sqrt{\frac{x_1}{(x_1+x_2)^3}}\sum_{N=max[0,n'-1]}^{min[n'+1,\nu]}\mathcal{M}_{n_1,m_1,n_2,m_2}^{N,m'-1,\nu-N,0}(x_1,x_2)\ \mathcal{P}^{(1)}(n',m';N,m'-1)\ \mathcal{P}^{(0)}(\nu-N,0)\\
&+\sqrt{\frac{x_2}{(x_1+x_2)^3}}\ \theta(n)\ \mathcal{M}_{n_1,m_1,n_2,m_2}^{n',m',n,-1}(x_1,x_2)\ \mathcal{P}^{(1)}(n,-1)\Bigg\}\delta_{m_1+m_2,m'-1}\ ,
\end{aligned} \tag{D.31}$$

where $\nu = N+n = n_1+n_2+\frac{1}{2}(|m_1|+|m_2|-|m'-1|)$ and $n = n_1+n_2-n'+\frac{1}{2}(|m_1|+|m_2|-|m'|-1) \geq 0$.

$$\begin{aligned}
&\int \frac{d^2q_1^\perp}{(2\pi)^2}\frac{d^2q_2^\perp}{(2\pi)^2}\frac{d^2q'^\perp}{(2\pi)^2}(2\pi)^2\delta^2(\sqrt{x_1}q_1^\perp + \sqrt{x_2}q_2^\perp - \sqrt{x'}q'^\perp)\cdot\left(q_1^\perp\right)^*\cdot\Psi_{n_1}^{m_1}(q_1^\perp)\Psi_{n_2}^{m_2}(q_2^\perp)\Psi_{n'}^{m'*}(q'^\perp)\\
=&\Bigg\{\sqrt{\frac{x_1}{(x_1+x_2)^3}}\sum_{N=max[0,n'-1]}^{min[n'+1,\nu]}\mathcal{M}_{n_1,m_1,n_2,m_2}^{N,m'+1,\nu-N,0}(x_1,x_2)\ \mathcal{PC}^{(1)}(n',m';N,m'+1)\mathcal{P}^{(0)}(\nu-N,0)\\
&+\sqrt{\frac{x_2}{(x_1+x_2)^3}}\ \theta(n)\ \mathcal{M}_{n_1,m_1,n_2,m_2}^{n',m',n,1}(x_1,x_2)\ \mathcal{PC}^{(1)}(n,1)\ \Bigg\}\delta_{m_1+m_2,m'+1}\ ,
\end{aligned} \tag{D.32}$$

where $\nu = N+n = n_1+n_2+\frac{1}{2}(|m_1|+|m_2|-|m'+1|)$ and $n = n_1+n_2-n'+\frac{1}{2}(|m_1|+|m_2|-|m'|-1) \geq 0$.

APPENDIX E. CONTRIBUTIONS TO THE LF HAMILTONIAN

E.1 Kinetic energy for the $N\pi$ system

The contribution from a free nucleon to P^- is

$$P^-_{\mathrm{KE_N}} = \sum_{p^+} \sum_{s=-\frac{1}{2}}^{\frac{1}{2}} \sum_{t=-\frac{1}{2}}^{\frac{1}{2}} \int \frac{d^2p^\perp}{(2\pi)^2} b^\dagger(p,s,t)\ b(p,s,t) \frac{(p^\perp)^2 + M_N^2}{p^+}\ . \tag{E.1}$$

Substituting Eq. (4.46) to the above expression, we obtain the analytic expression of the contribution of a free nucleon to the mass squared operator H [Eq. (4.49)] in terms of the LF basis:

$$\begin{aligned} &P^+ P^-_{KE_N} \\ =&\sum_{x_N} \sum_{s} \sum_{t} \sum_{n_1,m_1} \sum_{n_2,m_2} \beta^\dagger(x_N,n_1,m_1,s,t)\beta(x_N,n_2,m_2,s,t)\ \delta_{m_1,m_2} \\ &\times \left\{ b^2 \Big[(2n_2+|m_2|+1)\delta_{n_1,n_2} - \sqrt{n_1(n_1+|m_1|)}\delta_{n_1,n_2+1} - \sqrt{n_2(n_2+|m_2|)}\delta_{n_2,n_1+1} \Big] + \frac{M_N^2}{x_N}\delta_{n_1,n_2} \right\}, \end{aligned} \tag{E.2}$$

where we have applied the relation $x_N = \frac{p^+}{P^+}$ [Eq. (4.21)] with P^+ being the total longitudinal momentum. Note that $x_N = 1$ for the $|N\rangle$ sector and $0 < x_N < 1$ for the $|N\pi\rangle$ sector. When evaluating the integral, we have also made use of the integral identity Eq. (D.22).

The contribution from a free pion to P^- is

$$P^-_{\mathrm{KE}_\pi} = \sum_{k^+} \sum_{\lambda=-1}^{1} \int \frac{d^2k^\perp}{(2\pi)^2} a^\dagger(k,\lambda)\ a(k,\lambda) \frac{(k^\perp)^2 + M_\pi^2}{k^+}\ . \tag{E.3}$$

Analogous to Eq. (E.2), we also obtain the expression of the contribution of a free pion to the mass squared operator:

$$
\begin{aligned}
&P^+P^-_{KE_\pi}\\
=&\sum_{x_\pi}\sum_{\lambda}\sum_{n_1m_1}\sum_{n_2m_2}\alpha^\dagger(x_\pi,n_1,m_1,\lambda)\alpha(x_\pi,n_2,m_2,\lambda)\ \delta_{m_1,m_2}\\
&\times\left\{b^2\Big[(2n_2+|m_2|+1)\delta_{n_1n_2}-\sqrt{n_1(n_1+|m_1|)}\delta_{n_1,n_2+1}-\sqrt{n_2(n_2+|m_2|)}\delta_{n_2,n_1+1}\Big]+\frac{M_\pi^2}{x_\pi}\delta_{n_1,n_2}\right\},
\end{aligned}
\tag{E.4}
$$

with $x_\pi=\frac{k^+}{P^+}$. Note that $0<x_\pi<1$ in this work.

E.2 Interaction terms for the $N\pi$ system

Up to the level of the one-pion processes, the interaction terms in P^- can be sorted into the pion-absorption term and the pion-emission term

$$
P^-_{\text{int}} = \quad P^-_{\text{int;abs}}+P^-_{\text{int;em}}\ . \tag{E.5}
$$

For an incoming nucleon (labeled "2") that absorbs a pion (carrying momentum k and isospin projection λ) and the outgoing nucleon (labeled "1"), the term corresponding to one-pion absorption is

$$
\begin{aligned}
P^-_{\text{int;abs}} =&iM_N\frac{g_A}{F}\sum_{p_1^+}\sum_{p_2^+}\sum_{k^+}\frac{1}{2\pi\sqrt{2Lk^+}}\delta(p_1^+|k^++p_2^+)\\
&\sum_{s_1,s_2}\sum_{t_1,t_2}\sum_{\lambda}\int\frac{d^2p_1^\perp}{\sqrt{(2\pi)^2}}\frac{d^2k^\perp}{\sqrt{(2\pi)^2}}\frac{d^2p_2^\perp}{\sqrt{(2\pi)^2}}\delta^{(2)}(p_1^\perp-k^\perp-p_2^\perp)\\
&\times b^\dagger(p_1,s_1,t_1)a(k,\lambda)b(p_2,s_2,t_2)\\
&\times\underbrace{\zeta^\dagger(s_1)\left\{\frac{\gamma^\perp\cdot p_1^\perp+M_N}{p_1^+}\gamma_5-\gamma_5\frac{-\gamma^\perp\cdot p_2^\perp+M_N}{p_2^+}\right\}\zeta(s_2)}_{\text{spinor kernel}}\ \underbrace{T^\dagger(t_1)\Big[\sum_a\tau_a\varepsilon_a(\lambda)\Big]T(t_2)}_{\text{isospinor kernel}}\ ,
\end{aligned}
\tag{E.6}
$$

where $\delta(p_1^+|k^+ + p_2^+)$ is the Kronecker delta for the discretized longitudinal momenta p_1^+, k^+ and p_2^+; it ensures the conservation of the longitudinal momentum during the pion absorption. The spinor kernel for different helicity configurations of the incoming and outgoing nucleons is

$$\left|\begin{array}{c|c|c} s_1 & \zeta^\dagger(s_1)\left\{\frac{\gamma^\perp\cdot p_1^\perp + M_N}{p_1^+}\gamma_5 - \gamma_5\frac{-\gamma^\perp\cdot p_2^\perp + M_N}{p_2^+}\right\}\zeta(s_2) & s_2 \\ \uparrow & \frac{1}{p_1^+}M_N - \frac{1}{p_2^+}M_N & \uparrow \\ \uparrow & \frac{1}{p_1^+}(p_1^\perp)^* - \frac{1}{p_2^+}(p_2^\perp)^* & \downarrow \\ \downarrow & \frac{1}{p_1^+}p_1^\perp - \frac{1}{p_2^+}p_2^\perp & \uparrow \\ \downarrow & -\frac{1}{p_1^+}M_N + \frac{1}{p_2^+}M_N & \downarrow \end{array}\right| . \tag{E.7}$$

For clarity, we use "$\uparrow$" and "$\downarrow$" to denote the values of $+\frac{1}{2}$ and $-\frac{1}{2}$, respectively. The isospinor kernel for different isospin configurations of the incoming and outgoing nucleons is

$$\left|\begin{array}{c|c|c||c} t_1 & T^\dagger(t_1)\Big[\sum_a \tau_a\varepsilon_a(\lambda)\Big]T(t_2) & t_2 & \lambda = t_1 - t_2 \\ \uparrow & 1 & \uparrow & 0 \\ \uparrow & \sqrt{2} & \downarrow & 1 \\ \downarrow & \sqrt{2} & \uparrow & -1 \\ \downarrow & -1 & \downarrow & 0 \end{array}\right| . \tag{E.8}$$

Applying Eqs. (4.45), (4.46) and Eq. (D.3), we obtain the contribution from the one-pion absorption term to the mass squared operator [Eq. (4.16)]:

$$
\begin{aligned}
P^+ \cdot P^-_{\text{int;abs}} =& iM_N \frac{g_A}{F} \frac{1}{\sqrt{4\pi K}} \sum_{x_1} \sum_{x_2} \sum_{x_k} \sum_{s_1,s_2} \sum_{t_1,t_2} \sum_{\lambda} \sum_{n_1,m_1} \sum_{n_2,m_2} \sum_{n_k,m_k} \sqrt{x_1 x_2}\ \delta(x_1|x_k+x_2) \\
& \times \beta^\dagger(x_1,n_1,m_1,s_1,t_1)\ \alpha(x_k,n_k,m_k,\lambda)\ \beta(x_2,n_2,m_2,s_2,t_2)\ T^\dagger(t_1)\Big[\sum_a \tau_a \varepsilon_a(\lambda)\Big] T(t_2) \\
& \times \int \frac{d^2q_1^\perp}{(2\pi)^2} \frac{d^2q_k^\perp}{(2\pi)^2} \frac{d^2q_2^\perp}{(2\pi)^2} (2\pi)^2 \delta^{(2)}(\sqrt{x_1} q_1^\perp - \sqrt{x_k} q_k^\perp - \sqrt{x_2} q_2^\perp) \\
& \times \begin{cases}
\Psi^{m_1 *}_{n_1}(q_1^\perp)\ \big[\frac{M_N}{x_1} - \frac{M_N}{x_2}\big]\ \Psi^{m_k}_{n_k}(q_k^\perp) \Psi^{m_2}_{n_2}(q_2^\perp), & \text{for } s_1 = \uparrow,\ s_2 = \uparrow \\
\Psi^{m_1 *}_{n_1}(q_1^\perp)\ \big[\frac{1}{\sqrt{x_1}}(q_1^\perp)^* - \frac{1}{\sqrt{x_2}}(q_2^\perp)^*\big]\ \Psi^{m_k}_{n_k}(q_k^\perp) \Psi^{m_2}_{n_2}(q_2^\perp), & \text{for } s_1 = \uparrow,\ s_2 = \downarrow \\
\Psi^{m_1 *}_{n_1}(q_1^\perp)\ \big[\frac{1}{\sqrt{x_1}} q_1^\perp - \frac{1}{\sqrt{x_2}} q_2^\perp\big]\ \Psi^{m_k}_{n_k}(q_k^\perp) \Psi^{m_2}_{n_2}(q_2^\perp), & \text{for } s_1 = \downarrow,\ s_2 = \uparrow \\
\Psi^{m_1 *}_{n_1}(q_1^\perp)\ \big[-\frac{M_N}{x_1} + \frac{M_N}{x_2}\big]\ \Psi^{m_k}_{n_k}(q_k^\perp) \Psi^{m_2}_{n_2}(q_2^\perp) & \text{for } s_1 = \downarrow,\ s_2 = \downarrow
\end{cases}
\end{aligned}
\tag{E.9}
$$

where we have substituted the identity $P^+ = \frac{2\pi}{L} K$. The longitudinal momentum fractions are $x_1 = \frac{p_1^+}{P^+}$, $x_2 = \frac{p_2^+}{P^+}$ and $x_k = \frac{p_k^+}{P^+}$. The analytic expression of the matrix element $P^+ \cdot P^-_{\text{int;abs}}$ in the LF representation can be evaluated applying the identities in Sec. D.3.

Note that the one-pion emission contribution to the mass squared operator is the Hermitian conjugate of the one-pion absorption term $P^+ P^-_{\text{int;abs}}$.

APPENDIX F. THE PROTON'S DIRAC FORM FACTOR

The Dirac form factor for the physical proton [Eq. (4.63)] is

$$F_1(Q^2) = F^p_{1,f}(Q^2) + F^{p\pi^0}_{1,f}(Q^2) + F^{n\pi^+}_{1,b}(Q^2) \ . \tag{F.1}$$

Note that q^2 is substituted by Q^2 according to Eq. (4.61).

The first contribution is

$$F^p_{1,f}(Q^2) = \sum_{t_N,n_N,m_N,s_N} C^*(x_N,n_N,m_N,s_N,t_N)C(x_N,n_N,m_N,s_N,t_N) \ , \tag{F.2}$$

which results from the virtual photon coupling to the current of the bare proton $|p\rangle$. Here, the basis quantum numbers (according to Eq. (4.27)) are shown explicitly for clarity. The subscript "f" denotes the contribution from the fermionic current. The summation in Eq. (F.2) is only for the bare proton sector, i.e., $x_N = 1$. In fact, $F^p_{1,f}(Q^2)$ is the probability of the bare proton sector, $|a_p|^2$ (according to Eq. (4.62)), and it is independent of Q^2.

The second contribution is

$$\begin{aligned} F^{p\pi^0}_{1,f}(Q^2) = &\sum_{x_N}\sum_{s_N}\sum_{t_N,\lambda}\sum_{n'_N,m'_N}\sum_{n'_\pi,m'_\pi}\sum_{n_N,m_N}\sum_{n_\pi,m_\pi} e\big(t_N\big) \\ &\times C^*(x_N,n'_N,m'_N,s_N,t_N;x_\pi,n'_\pi,m'_\pi,\lambda)C(x_N,n_N,m_N,s_N,t_N;x_\pi,n_\pi,m_\pi,\lambda) \\ &\times \langle n'_N,m'_N;\frac{x_\pi}{\sqrt{x_N}}q^\perp|n_N,m_N\rangle\ \langle n'_\pi,m'_\pi;-\frac{x_\pi}{\sqrt{x_\pi}}q^\perp|n_\pi,m_\pi\rangle \ . \end{aligned} \tag{F.3}$$

$F^{p\pi^0}_{1,f}(Q^2)$ denotes the contribution from the virtual photon coupling to the current of the bare proton when dressed by charge-neutral π^0. The effective charge factor of the nucleons is $e\big(+\frac{1}{2}\big) = 1$ and $e\big(-\frac{1}{2}\big) = 0$. The kernel in the last line is the shifted operator, which is defined in Appendix D.3.2. This kernel, hence $F^{p\pi^0}_{1,f}(Q^2)$, vanishes as $Q^2 \to \infty$. At the limit of $Q^2 = 0$, $F^{p\pi^0}_{1,f}(0) = |a_{p\pi^0}|^2$, which represents the probability of the $|p\pi^0\rangle$ sector [Eq. (4.62)].

The third contribution is

$$F_{1,b}^{n\pi^+}(Q^2) = \sum_{x_N}\sum_{s_N}\sum_{t_N,\lambda}\sum_{n'_N,m'_N}\sum_{n'_\pi,m'_\pi}\sum_{n_N,m_N}\sum_{n_\pi,m_\pi} e(\lambda)$$
$$\times C^*(x_N,n'_N,m'_N,s_N,t_N;x_\pi,n'_\pi,m'_\pi,\lambda)C(x_N,n_N,m_N,s_N,t_N;x_\pi,n_\pi,m_\pi,\lambda)$$
$$\times \langle n'_N,m'_N;-\frac{x_N}{\sqrt{x_N}}q^\perp|n_N,m_N\rangle\ \langle n'_\pi,m'_\pi;\frac{x_N}{\sqrt{x_\pi}}q^\perp|n_\pi,m_\pi\rangle\ . \tag{F.4}$$

$F_{1,b}^{n\pi^+}(Q^2)$ denotes the contribution from the virtual photon coupling to the current of π^+ that dresses the bare neutron. The subscript "b" denotes the contribution from the bosonic current. The effective charge factor of the pions is $e(\lambda) = +1, 0, -1$ for $\lambda = +1, 0, -1$. Analogous to $F_{1,f}^{p\pi^0}(Q^2)$, $F_{1,b}^{n\pi^+}(Q^2)$ vanishes for $Q^2 \to \infty$. At the limit of $Q^2 = 0$, $F_{1,b}^{n\pi^+}(0) = |a_{n\pi^+}|^2$, which represents the probability of the $|n\pi^+\rangle$ sector [Eq. (4.62)].